GFZ

Helmholtz-Zentrum
POTSDAM

HELMHOLTZ-ZENTRUM POTSDAM
DEUTSCHES
GEOFORSCHUNGSZENTRUM

Katja K. Hirsch

Integrating structural and sedimentological observations with numerical lithospheric models to assess the 3D evolution of the South African continental passive margin

Scientific Technical Report STR08/13

www.gfz-potsdam.de

HELMHOLTZ
GEMEINSCHAFT

Integrating structural and sedimentological observations with numerical lithospheric models to assess the 3D evolution of the South African continental passive margin

Katja K. Hirsch

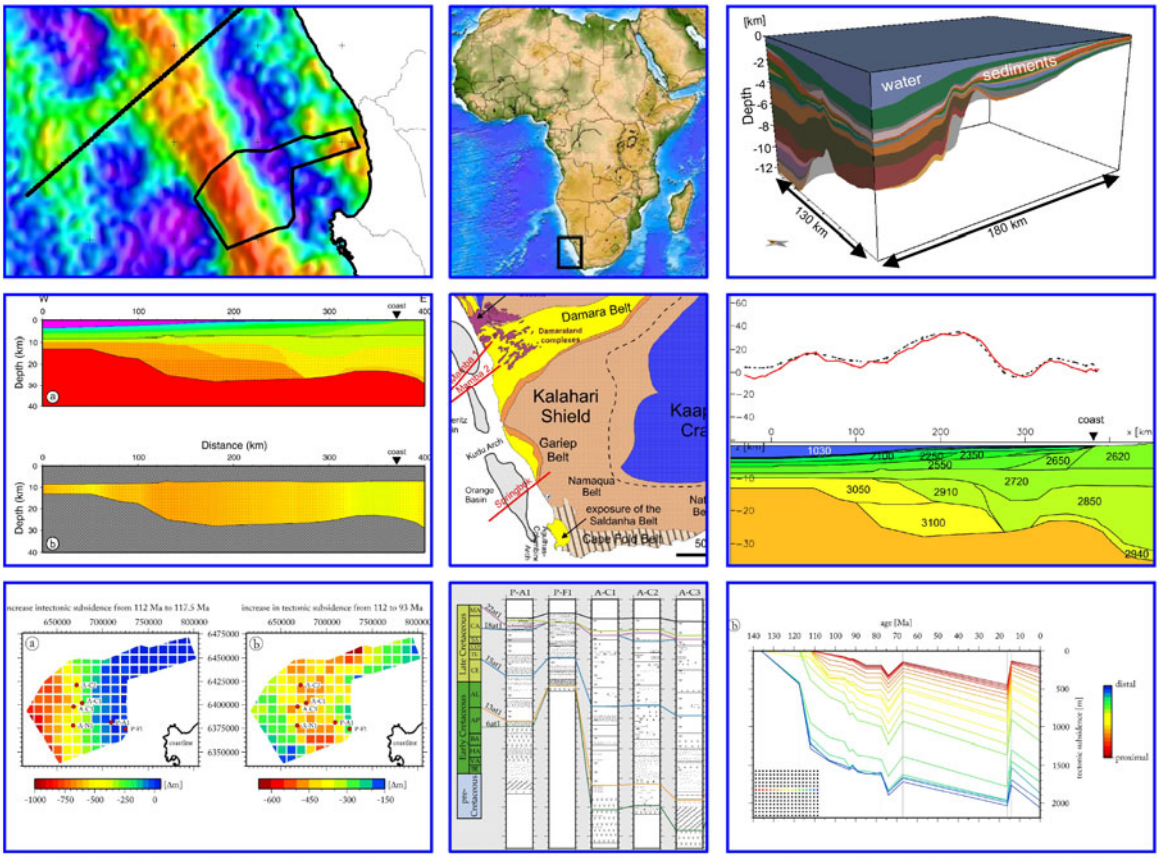

1. Gutachter: Prof. Dr. Onno Oncken, Helmholtz-Zentrum Potsdam
Deutsches GeoForschungsZentrum GFZ, Freie Universität Berlin
2. Gutachter: Prof. Dr. Sierd A. P. L. Cloetingh, Vrije Universiteit
Amsterdam

Mitglieder der Kommission:
Prof. Dr. G. Kaufmann, Freie Universität Berlin
Prof. Dr. Ch. Heubeck, Freie Universität Berlin
Dr. M. Scheck-Wenderoth, Helmholtz-Zentrum Potsdam
Deutsches GeoForschungsZentrum GFZ

Integrating structural and sedimentological observations with numerical lithospheric models to assess the 3D evolution of the South African continental passive margin

Dissertation

zur Erlangung des akademischen Grades

doctor rerum naturalium (Dr. rer. nat.)

dem Fachbereich Geowissenschaften

der Freien Universität Berlin

vorgelegt

von

Katja K. Hirsch

Berlin, 09.12.2008

Eidesstattliche Erklärung

Hiermit versichere ich, dass die vorliegende Dissertation ohne unzulässige Hilfe Dritter und ohne Benutzung anderer als der angegebenen Literatur angefertigt wurde. Die Stellen der Arbeit, die anderen Werken wörtlich oder inhaltlich entnommen sind, wurden durch entsprechende Angaben der Quellen kenntlich gemacht. Diese Arbeit hat in gleicher oder ähnlicher Form noch keiner Prüfungsbehörde vorgelegen.

Potsdam, September 2008

to my father

Content

Chapter 2 and 3 are already published or in press in the following international scientific journals:

Chapter 2

Crustal structure beneath the Orange Basin, South Africa

Hirsch, K.K., Scheck-Wenderoth, M., Paton, D.A. and Bauer, K.

2007
South African Journal of Geology, **110(2/3)**: 249-260

Chapter 3

**Deep structure of the western South African passive margin –
Results from a combined approach of seismic, gravity and isostatic investigations**

Hirsch, K.K., Bauer, K. and Scheck-Wenderoth, M.
2008
Tectonophysics (in press)

Chapter 4 represents a manuscript submitted to Marine and Petroleum Geology.

Summary

Although the development of passive margins has been extensively studied over a number of decades, significant questions remain on how mantle and crustal dynamics interact to generate the observed margin geometries. Here, the Orange Basin, located on the south-west African continental margin is investigated. The basin fill is considered to comprise a classic rift-drift passive margin sequence recording the break-up of Gondwana and subsequent opening of the South Atlantic Ocean. Based on interpreted seismic reflection data, a 3D geological model was first constructed. Subsequently, an isostatic calculation (Airy´s model) using a homogeneous middle and lower crust was applied to this geological model to determine the position of the Moho for an isostatically balanced system. Isostatic sensitivity tests were applied to the model, and their gravity response was validated against different crustal structures for the basin. The best-fit model requires dense, presumably mafic material in the middle and lower crust beneath the basin and an abrupt change to less dense material near the coast to reproduce the observed gravity field.

The passive margin of the South Atlantic shows typical features of a rifted volcanic continental margin, encompassing seaward dipping reflectors, continental flood basalts and high-velocity/density lower crust at the continent-ocean transition, probably emplaced during initial seafloor spreading in the Early Cretaceous.

The Springbok profile offshore western South Africa is a combined transect of reflection and refraction seismic data. This thesis addresses the analysis of the seismic velocity structure in combination with gravity modelling and isostatic modelling to unravel the crustal structure of the passive continental margin from different perspectives.

The velocity modelling revealed a segmentation of the margin into three distinct parts of continental, transitional and oceanic crust. As observed at many volcanic margins, the lower crust is characterised by a zone of high velocities with up to 7.4 km/s. The conjunction with gravity modelling affirms the existence of this body and at the same time substantiated its high densities, found to be 3100 kg/m³. Both approaches identified the body to have a thickness of about 10 km. Yet, the gravity modelling predicted the transition between the high-density body towards less dense material farther west than initially anticipated from velocity modelling and confirmed this density gradient to be a prerequisite to reproduce the observed gravity signal.

Finally, isostatic modelling was applied to predict average crustal densities if the margin was isostatically balanced. The results imply isostatic equilibrium over large parts of the profile; smaller deviations are supposed to be compensated regionally. The calculated load distribution along the profile implies that all pressures are hydrostatic beneath a depth of 45 km. The presence of lower crustal bodies of high seismic velocities indicates that large volumes of igneous crust formed as a consequence of lithospheric extension.

Furthermore, results of a combined approach using subsidence analysis and basin history inversion models are presented. The outcome shows that a classical uniform stretching model does not account for the observed tectonic subsidence. Moreover, it is found that that the thermal and subsidence implications of underplating need to be considered. Another departure from the uniform stretching model is renewed sub-crustal stretching and linked to that uplift in the Cenozoic which is necessary to reproduce the observed phases of erosion and the present-day depth of the basin. The dimension of these events has been examined and quantified in terms of tectonic uplift and sub-crustal stretching. Based on these forward models the heat flow evolution is predicted not only for the available real wells but also for

virtual wells over the entire study area. Finally, the hydrocarbon potential and the temperature evolution is presented and shown in combination with inferred maturation of the sediments for depth intervals which comprise potential source rocks.

Zusammenfassung

Die Entwicklung passiver Kontinentalränder stand in den letzten Jahrzehnten im Focus zahlreicher wissenschaftlicher Untersuchungen. Jedoch liegen über die Wechselwirkung zwischen Kruste und Mantel, welche die Struktur der Kontinentalränder kontrolliert und wie wir sie heute vorfinden, keine ausreichenden Kenntnisse vor.

Die vorliegende Arbeit untersucht das Orange Becken vor der Atlantikküste Südafrikas. Es wird angenommen, dass das Becken eine klassische Rift-Drift Sequenzabfolge eines passiven Kontinentalrandes enthält, beginnend beim Aufbruch der Kontinente und der darauffolgenden Öffnung des Südatlantiks.

Basierend auf der Interpretation reflektionsseismischer Daten wurde ein geologisches 3D-Modell konstruiert. Anschließend wurde dieses Modell für isostatische Berechnungen (Airy) mit einer homogenen mittleren und unteren Kruste genutzt, um die Tiefenlage der Moho unter der Vorraussetzung eines isostatischen Gleichgewichtes zu berechnen. Für diese Modelle wurden Sensitivitätstests durchgeführt, welche wiederum die Grundlage für gravimetrische Berechnungen der unterschiedlichen Krustenkonfigurationen lieferten. Das Modell, welches das gemessene Schwerefeld am besten reproduziert, enthält dichtes, vermutlich mafisches Material in der unteren Kruste und einen starken Dichtekontrast zu weniger dichtem Material in Küstennähe.

Der passive Kontinentalrand Südafrikas weist typische Eigenschaften eines gerifteten vulkanischen Kontinentalrandes auf, der seewärts geneigte Reflektoren und kontinentale Flutbasalte umfasst sowie eine untere Kruste, die sich durch hohe Geschwindigkeiten und Dichten auszeichnet. Diese Strukturen wurden mit hoher Wahrscheinlichkeit während des Aufbruchs der Kontinente in der Frühen Kreide intrudiert bzw. extrudiert.

Das Profil Springbok ist ein kombiniertes Profil aus reflektionsseismischen und refraktionsseismischen Messungen. Die vorliegende Arbeit untersucht die seismische Geschwindigkeitsstruktur in Kombination mit gravimetrischen und isostatischen Modellierungen, um die tiefere Krustenstruktur des Kontinentalrandes aus unterschiedlichen Blickwinkeln zu beleuchten.

Das berechnete Geschwindigkeitsmodell erlaubt eine Segmentierung des Kontinentalrandes in kontinentale, Übergangs- und ozeanische Kruste. Die untere Kruste zeichnet sich durch hohe Geschwindigkeiten von bis zu 7.4 km/s aus, was entlang vieler Kontinentalränder beobachtet wird. Durch die Verbindung der Ergebnisse mit einem gravimetrischen Modell kann die Existenz und die hohe Dichte des Körpers von 3100 kg/m^3 bestätigt werden. Beide Ansätze ergaben eine Mächtigkeit des Körpers von rund 10 km. Jedoch wurde durch das gravimetrische Modell vorhergesagt, dass sich der Übergangsbereich zwischen dichtem Unterkrustenkörper und leichterem Material weiter westlich befindet, als durch das Geschwindigkeitsmodell vorhergesagt. Weiterhin sagt das gravimetrische Modell aus, dass ohne die Anwesenheit dieses dichten Körpers in der unteren Kruste das gemessene Schwerefeld nicht reproduziert werden kann.

Mit Hilfe eines isostatischen Modells wurde die mittlere Krustendichte für den Fall des isostatischen Gleichgewichts berechnet. Die Ergebnisse lassen auf isostatisches Gleichgewicht schließen, wobei angenommen wird, dass kleinere Abweichungen regional kompensiert werden. Die berechnete Lastverteilung entlang des Profils impliziert das Vorherrschen hydrostatischen Drucks unterhalb einer Tiefe von 45 km.

Die Anwesenheit eines Körpers mit hohen Dichten in der unteren Kruste deutet auf die Bildung großer Mengen magmatischer Kruste in Folge von lithospherischer Extension hin.

Des Weiteren werden die Ergebnisse eines kombinierten Ansatzes präsentiert, der aus Subsidenzanalysen und Modellen, welche die Beckengeschichte invertieren, besteht. Die Ergebnisse zeigen, dass ein klassisches uniformes Rift-Modell nicht in der Lage ist, die heute beobachtete tektonische Subsidenz zu reproduzieren. Darüber hinaus kann festgestellt werden, dass die Implikationen einer dichten Unterkruste auf die Subsidenz und die thermische Entwicklung des Beckens nicht vernachlässigt werden kann. Eine weitere Abweichung von dem klassischen uniformen Rift-Modell stellt eine nochmalige Dehnung der subkrustalen Bereiche und damit verbunden eine Hebung des Kontinentalrandes im Känozoikum dar. Diese Abweichung ist notwendig, um beobachtete Erosionsereignisse und die heutige Beckentiefe zu reproduzieren. Die Intensität dieser Ereignisse ist bezüglich reiner tektonischer Hebung und subkrustaler Dehnung untersucht und quantifiziert worden.

Basierend auf diesen Vorwärtsmodellen wird die Entwicklung des Wärmeflusses, nicht nur für die verfügbaren Bohrungen, sondern auch für synthetische Bohrungen, welche das gesamte Arbeitsgebiet abdecken, vorhergesagt.

Abschließend wird das Potenzial zur Bildung von Kohlenwasserstoffen und die Entwicklung der Temperaturen betrachtet, im Speziellen für Tiefenbereiche möglicher Muttergesteine.

1 Introduction and motivation

The main goal of this thesis is the understanding of the present-day crustal structure of and the tectonic evolution of the Orange Basin.

The Orange Basin is an extensional sedimentary basin which formed in the wake of the Jurassic-Early Cretaceous Gondwana break-up on what was to become the southwestern African passive continental margin. Rifts are commonly accompanied by transient volcanic activity. That way, tectonic events affecting the South Atlantic margin prior to, during and after the break-up left their marks on the sedimentary successions. Although the basin has been extensively studied (e.g. Paton et al., 2008; Paton et al., 2007; Brown et al., 1995; Muntingh and Brown, 1993; Muntingh, 1993; Dingle et al., 1983; Gerrard and Smith, 1982) many aspects of basin formation remain open. The aim of this thesis is to provide integrated and quantitative models of the present-day crustal structure and the tectonic evolution of the basin using geological, geophysical and geothermal information. In this process the understanding of the present-day structure is the key to perceive the basin's history.

The passive continental margin offshore western South Africa provides a predestined area to understand the formation and evolution of sedimentary basins in response to rifting and continental break-up since the sedimentary successions consist of mainly clastics devoid of salt. Thus the basin is not affected by salt tectonic deformation and salt-related reduction of seismic resolution as found in other parts of the Atlantic.

Passive continental margins are the transition between continental and oceanic lithosphere where a considerably thick sedimentary pile overlies thinned continental crust. In mature stages these margins are regarded as quiescent whereas being formed they are subdued to large-scale geodynamic processes. Thinning and finally break-up of the lithosphere is linked to significant tectonic activity and mainly also to transient magmatism.

The volcanic character of the margin offshore South Africa was first postulated by Hinz (1981) and Austin and Uchupi (1982). The continental margin shows typical features of a volcanic passive margin, comprising onshore continental flood basalts, voluminous extrusive basaltic complexes along the continent-ocean boundary appearing as a wedge of seaward dipping reflectors in seismic images on top of the continental crust (Gladczenko et al., 1997; Hinz, 1981), lower crustal igneous accretions characterised by high seismic velocities (e.g. Bauer et al., 2000), and thicker than normal oceanic crust adjacent to the continent-ocean boundary (Eldholm et al., 1995).

Data acquisition has been escalated in the Orange Basin within the last decades not least for the sake of hydrocarbon potential but main questions on the interplay of rift tectonics and subsequent structural and sedimentary evolution remained open. At the same time the structure of the south western African passive continental margin remains enigmatic as only little deep seismic data is available.

The database of this work comprises a comprehensive seismic reflection dataset, biostratigraphic age constraints as well as lithological information from wells in the main working area which is used for the creation of a 3D structural model depicting the sedimentary successions within the basin. Seismic constraints on the crustal structure are lacking since the penetration of seismic energy is restricted to the upper crust.

The marine gravity field along the continental margin is characterised by an elongated positive free-air anomaly, the so-called edge-effect anomaly, which is used as a further source of input data giving constraints on deep-seated structures in the crust. Accordingly,

gravity modelling and the development of isostatic crustal models are used to investigate the deep crustal structure of the margin where the sedimentary successions of the system are resolved by seismic data to complete the picture of the margin in this domain.

Farther north of the working area, covered by shallow seismic reflection data, a seismic refraction line offers insights into the deep crustal structure. A detailed analysis of this profile has been carried out to assess the variation of seismic velocities across the margin. The results of this velocity modelling are validated against a gravity model along the profile and, in addition, against an isostatic crustal model to reduce ambiguities to which potential field modelling is prone to.

This project utilises the different available data sets to assemble a holistic picture of the Orange Basin, leveraging the diversity of input data.

The resulting 3D crustal model is in a further step used as a starting point for inverse and forward modelling of the basin's subsidence history. This includes the reconstruction of the thermal evolution from the onset of rifting throughout the drift stage until present-day. Processes and their mechanisms are identified which influenced the margin in the past and validated concerning their intensity and consequences on the thermal evolution.

2 Crustal structure beneath the Orange Basin, South Africa

Abstract

Although the development of passive margins has been extensively studied over a number of decades, significant questions remain on how mantle and crustal dynamics interact to generate the observed margin geometries. Here, we investigate the Orange Basin, located on the south-west African continental margin. The basin fill is considered to comprise a classic rift-drift passive margin sequence recording the break-up of Gondwana and subsequent opening of the South Atlantic Ocean. Based on interpreted seismic reflection data, a 3D geological model was first constructed. Subsequently, an isostatic calculation (Airy´s model) using a homogeneous middle and lower crust was applied to this geological model to determine the position of the Moho for an isostatically balanced system. Isostatic sensitivity tests were applied to the model, and their gravity response was validated against different crustal structures for the basin. The best-fit model requires dense, presumably mafic material, in the middle and lower crust beneath the basin and an abrupt change to less dense material near the coast to reproduce the observed gravity field.

2.1 Introduction

The Orange Basin offshore southwest Africa (Figure 1) is located within the passive continental margin of the South Atlantic between 31° and 33.5°S. It developed within a divergent plate boundary setting in response to lithospheric extension related to the break-up of South America and Africa in the Late Jurassic, followed by seafloor spreading and the opening of the South Atlantic Ocean in the Early Cretaceous around 136 Ma (Macdonald et al., 2003; Reeves and de Wit, 2000; Brown et al., 1995). The latest models of the relative motion between the South American and the African plates suggest a diachronous opening of the South Atlantic, starting in the south and propagating to the north within a time span of 40 Myrs (Eagles, 2007).

The Orange Basin contains the stratigraphic record from lithospheric extension and rift tectonics throughout a fully evolved post-break-up setting, and thus provides an ideal area to study the evolution of a "passive" continental margin. The stratigraphy comprises pre-rift successions (older than Late Jurassic, >130 Ma), that is overlain by syn-rift deposits of Late Jurassic to Hauterivian age (121-116.5 Ma), and, in turn, by sediments of early drift stages up to Aptian age (113- 108 Ma). Non-restricted marine deposits of an Aptian to present-day age overly the Pre-Aptian successions. The rift stage basin was characterised by the development of N-S oriented grabens and half-grabens trending approximately parallel to the rift axis, from near Walvis Bay to south of Cape Town (Gerrard and Smith, 1982). These graben structures were filled predominantly with siliciclastic continental and lacustrine sediments, and variable thicknesses of volcanic rocks (Brown et al., 1995). The syn-rift sequences rest unconformably on the Precambrian or Paleozoic basement and are unconformably overlain by Early Cretaceous to present post-rift successions. Lithologically the early post-rift successions comprise sandstone and shales, and the majority of the post-rift successions are claystones.

We present a 3D structural model the Orange Basin consistent with available seismic and lithologic well data, and validated this model using satellite gravity data to constrain the crustal structure of the basin.

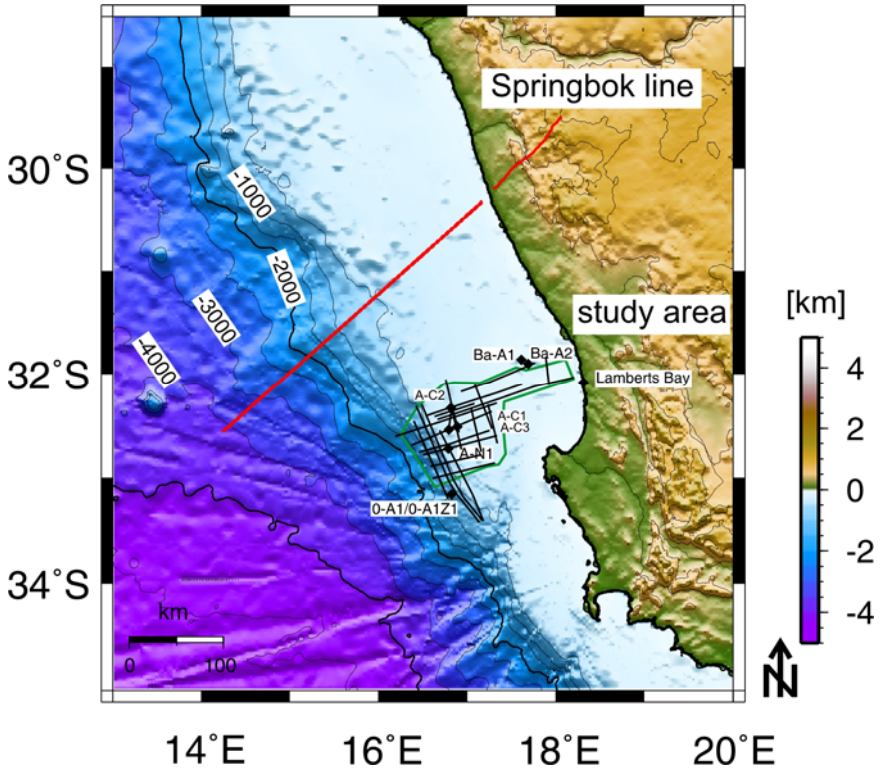

Figure 1: Bathymetric map of the continental margin offshore South Africa. The green line frames the study area and outlines the inferred 3D geological model constrained by interpreted seismic reflection lines (black lines). Black diamonds represent wells within the study area. The location of the Springbok seismic refraction profile is shown in addition with a red line.

2.2 Data base and construction of a geological 3D model

The study is based on results from seismic interpretation of 2D seismic lines recorded across the Orange Basin to a maximum of 6 seconds two-way travel time. Depth maps of interpreted horizons (Paton et al., 2008) were used in combination with the sequence stratigraphic framework established by previous studies (Brown et al., 1995; Muntingh, 1993; Muntingh and Brown, 1993) and data from 5 boreholes (including wire line logs, lithologies, vitrinite reflectance and biostratigraphy) to generate a 3D geological model. The interpreted horizons comprise a sequence of horizons from the near top-basement and the oldest lower drift horizon (6at1) through to the top of the drift succession, defined by the 22at1 horizon; these horizons correspond to an age range of 117.5 Ma to 67 Ma (Brown et al., 1995). Furthermore, between the basement and the drift horizons 5 syn-rift successions (SR-horizons cf. Table 1) were included, these were obtained from literature (Brown et al., 1995).

Information on the crustal structure underlying the basin sediments was available from the Springbok deep-seismic refraction experiment (Mahanyele et al., 2004) carried out approximately 100 km to the north of the study area (Figure 1).

In addition, the free-air gravity anomaly and the bathymetry across the study area are extracted from Sandwell and Smith (1997) using the 1-min grid as a reference for the gravity

modelling. The marine gravity field along the West African margin is characterised by an elongated, free-air anomaly parallel to the margin, known as the "edge-effect" anomaly (Figure 2). This positive anomaly occurs just above the continental shelf break and is one of the most prominent features characterising the gravity field of offshore southwest Africa. Similar anomalies are observed at many passive continental margins and in particular along large parts of the conjugate margins of the Atlantic Ocean (Watts and Fairhead, 1999). The simplest configuration of an edge-effect anomaly is a positive "high" that correlates with the outer shelf, and a seaward "low". In many places an additional landward "low" is also linked with the gravity "high" (Watts and Fairhead, 1999).

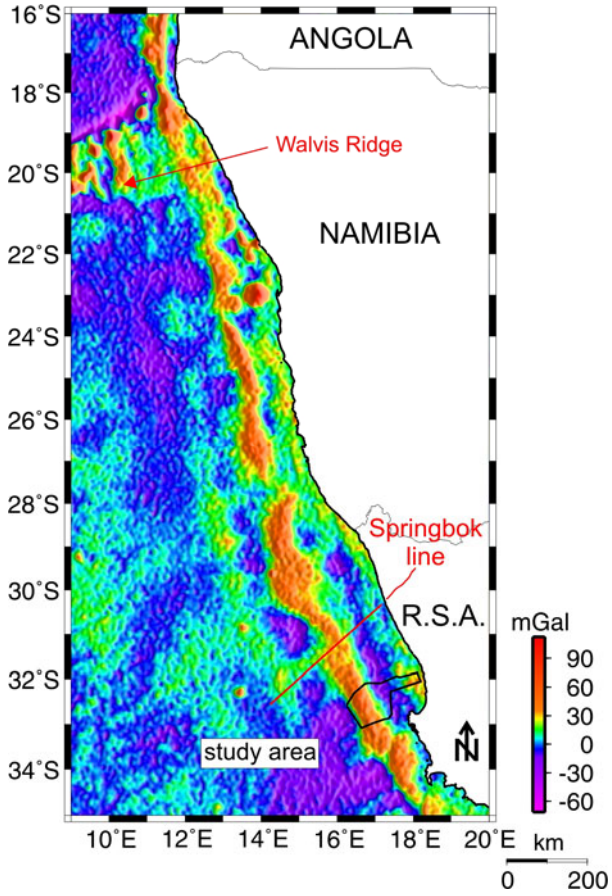

Figure 2: Free air gravity field with positive "edge-effect" anomaly parallel to the margin (Sandwell and Smith, 1997).The Location of the on- and offshore seismic refraction line is shown with a red line, and the bold black line encompasses the study area.

Along the coast of West Africa the positive edge-effect anomaly displays variable characteristics. South of the Walvis Ridge, offshore Namibia, the character of the edge-effect anomaly is very diffuse and the gravity signal appears complex. Southwards, nearby the border with South Africa, the anomaly is expressed as a simpler "high-low" pair. Farther south, in the middle of the Orange Basin, this positive-negative couple can be observed clearly.

To construct the geological model, depth maps from seismic interpretation were interpolated using a minimum tension gridding algorithm to derive depth grids covering the entire study area. Subtraction of successive depth levels yielded the thickness of the geological units in-between. These 2D thickness grids of each unit were then integrated into a 3D geological model using the **G**eological **M**odelling **S**ystem (GMS) developed at the GeoForschungsZentrum Potsdam (Scheck and Bayer, 1997). The model (Figure 3) covers an

area of 180 km in an east-west direction and 130 km in a north-south direction, with a grid size of 58 x 33. This corresponds to a horizontal resolution of 3 by 4 km. Vertically, the resolution of the model is defined by the 18 stratigraphic layers (Table 1, Figure 3, Figure 1) and average physical properties are assigned to each layer. For the isostatic and gravimetric model calculations density is the decisive physical parameter. To derive realistic bulk densities for each layer a porosity-depth relationship combined with lithology-dependent matrix densities was assigned using well log information. Table 1 gives an overview of the densities used to construct the 3D model of the sediments, which in turn was used for isostatic crustal modelling to derive the position of the Moho beneath the basin.

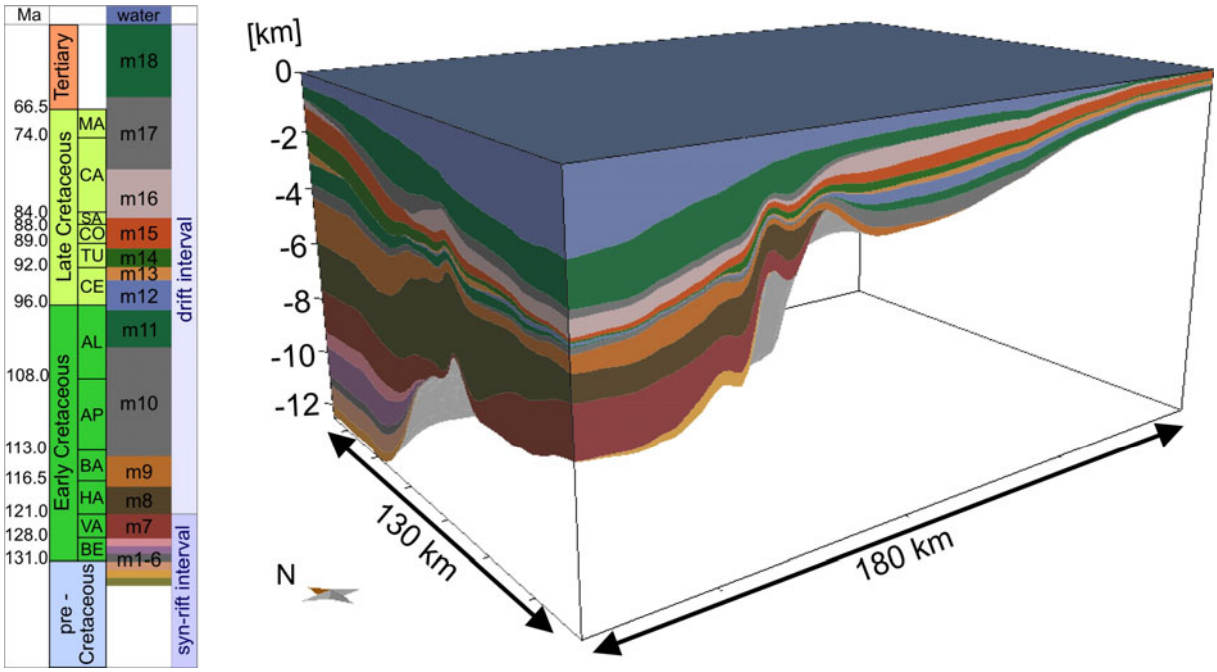

Figure 3: 3D geological model comprising the study area with 18 assigned layers from the interpretation of seismic lines and well data.

2.3 Gravity modelling

Three different models were tested to evaluate the influence of different crustal levels on the gravity field. The 18 layers of the geological model were reduced to 6 layers of significant density contrasts, by combining different layers of similar densities, to facilitate the gravity modelling.

As mentioned above, the seismic- and well data constrain the sedimentary cover of the study area. Once the geometry and density distribution in the sedimentary package were defined, different crustal configurations were investigated and tested against the observed gravity data. This was done in a three step procedure. First, the entire crust was treated as homogeneous and the variation of an average crustal density was tested. Second, the known densities of the sedimentary part were included to evaluate the gravity effect of the sediments. Third, realistic lateral variations of density in the middle and lower crust, based on information from the Springbok deep seismic refraction line, were incorporated to obtain a final gravity model that was compared to the observed gravity.

seismic horizons	assigned 3D model layers	porosity φ_0 [%]	density ρ[g/cm³]	densities for the gravity modelling	lithologies
	mwater				
post22at1	m18	~70	1.7	1.80	clay-stone
22at1	m17	~50	1.81		
pre22at1	m16	~50	1.9		
16dt1	m15	~40	2.15	2.30	
16at1	m14	~35	2.25		
15at1	m13	~27	2.4		
14ht1	m12	~22	2.5	2.52	silty sandstone
14at1	m11	~18	2.54		
13ht1	m10	~16	2.6	2.60	sandstone
13at1	m9	max. 12	2.6		
6at1	m8	10	2.61	2.61	
Hauter	m7	10	2.62		
SR1upper	m6	10	2.62		
SR1lower	m5	10	2.62		
SR2upper	m4	10	2.62		
SR2lower	m3	10	2.62		
SR3upper	m2	10	2.62		
	m1	10	2.62		

Table 1: Overview of seismic horizons interpreted from seismic reflection data and the inferred layers in the 3D geological and gravity model, together with porosities and assigned densities.

The software IGMAS was used for gravity modelling. IGMAS is an interactive, graphical computer system for the interpretation of potential field data by means of numerical simulations in 3D (Goetze and Lahmeyer, 1988). Geologic structures are defined as polygons along parallel working planes; the triangulation between vertical planes is done automatically as well as the transformation from the 2D data input into the 3D model structure. Within the gravity models presented here the distance between each working plane is 25 km. Successive and interactive modification of parameters along the working planes, either density or geometry or both, enables the user to create a model as realistic as possible. To avoid boundary effects, the gravity models were extended to both sides of the study area. The reference density is 2.67 g/cm³.

Finally, the algorithm based on triangulated polyhedrons is used for the calculation of the potential field resulting from the respective model (Goetze and Lahmeyer, 1988).

2.3.1 Isostatic model based on homogeneous crust

The simple model considers a homogeneous crust; the only constraint is present-day water depth. This model was calculated for an area beyond the constrained 3D geological model and covers the entire area shown in Figure 1. A depth position of the Moho was calculated with GMS assuming Airy isostasy. Airy´s concept presumes static equilibrium with local compensation of the topography by buoyancy and gravitational forces (e.g. Fowler, 1996). The crust is considered as floating in a denser mantle. Buoyancy forces, based on Archimedes principle, act on the crust to equal the weight of displaced mantle material. Isostatic compensation is achieved within a homogeneous crust by varying the depth to the crust/mantle boundary (Moho). Thus, a change in crustal thickness and hence Moho

topography, balances the masses. The resulting Moho depth for this simple model depends on the chosen average crustal density as well as on the assumed depth of isostatic compensation. Modelling is based on the comparison with a reference model defined as a crustal block with a given thickness and density that "sinks" into the mantle. Firstly, the equilibrium conditions for the reference model are calculated according to:

$$\rho_C \cdot h_C = \rho_M \cdot h_M \quad (1)$$

Where

ρ_c = crustal density;	h_c = thickness of the crust;
ρ_M = mantle density;	h_M = thickness of displaced mantle.

Secondly, the isostatic compensation is calculated for the model accounting for the present-day water depth and the configuration of the sediments. Accordingly, a varying of the crustal thickness, and thus a change in the topography of the Moho, balances the masses:

$$\rho_c \cdot h_c + \rho_M \cdot h_M = \rho_W \cdot h_W + \sum \rho_S \cdot h_S + \rho_C \cdot h_C + \rho_M \cdot h_M \quad (2)$$

Where

ρ_c = crustal density;	h_c = thickness of the crust;
ρ_M = mantle density;	h_M = thickness of displaced mantle;
ρ_w = water density;	h_w = water depth;
ρ_s = sediment density;	h_s = thickness of the sediments.

The base of the crust in the reference model corresponds to the compensation depth because at this level isostatic equilibration is achieved and below this depth all pressures are hydrostatic (e.g. Fowler, 1996). The compensation depth (cd) with respect to an Airy isostatic model, therefore, implies the depth of the deepest block (e.g. Sleep and Fuyita, 1997). The reference compensation depth is chosen to coincide with observations from the Springbok seismic refraction profile, where the greatest crustal thickness is about 35 km in the continental part of the profile. The first calculated model considers a compensation depth of 34 km and a mantle density of 3.3 g/cm³. Crustal density is assumed to be homogeneous (ρ_{crust}=2.75 g/cm³) and the position of the Moho is obtained from an isostatic calculation that balances the present-day water depth.

The resulting model shows a Moho position at a depth of 34 km in the eastern, landward part of the model. Westward, with increasing water depth, the Moho depth decreases. In the south-western part of the model, where the water depth reaches a maximum, the Moho shallows to less than 27 km (Figure 4).

These findings are included into the IGMAS gravity modelling program to calculate the gravity response of this simple model. Along a cross-section through the 3D gravity model (Figure 5), the calculated result is shown. The gravity response of the model in the east is a flat curve, similar to the observed gravity field. Although the signature of both curves is similar, the response of the model is not able to fit the observations, especially between 0 and 300 km along the profile.

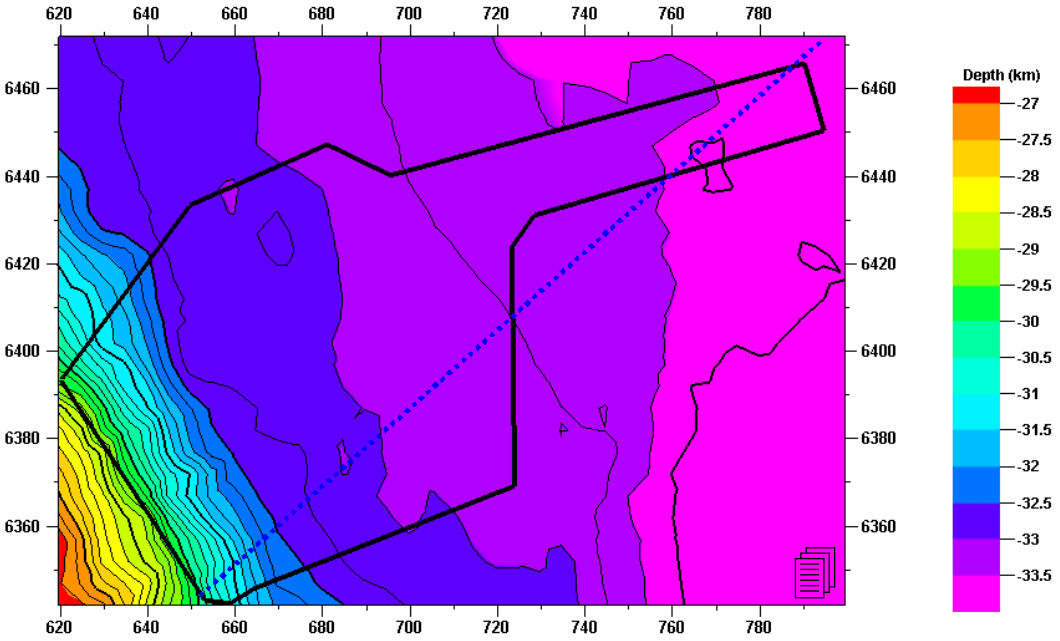

Figure 4: Moho position for the simple case model considering a homogenous crust and present-day water depth. The crustal density is 2.75 g/cm³, mantle density is 3.3 g/cm³ and the compensation depth is 34 km in the reference model. The black outline shows the area covered by seismic reflection data. The blue dotted line is the working plane shown in Fig. 5,6,7,9,10. Map is in UTM coordinates (kilometres), Zone -33 S.

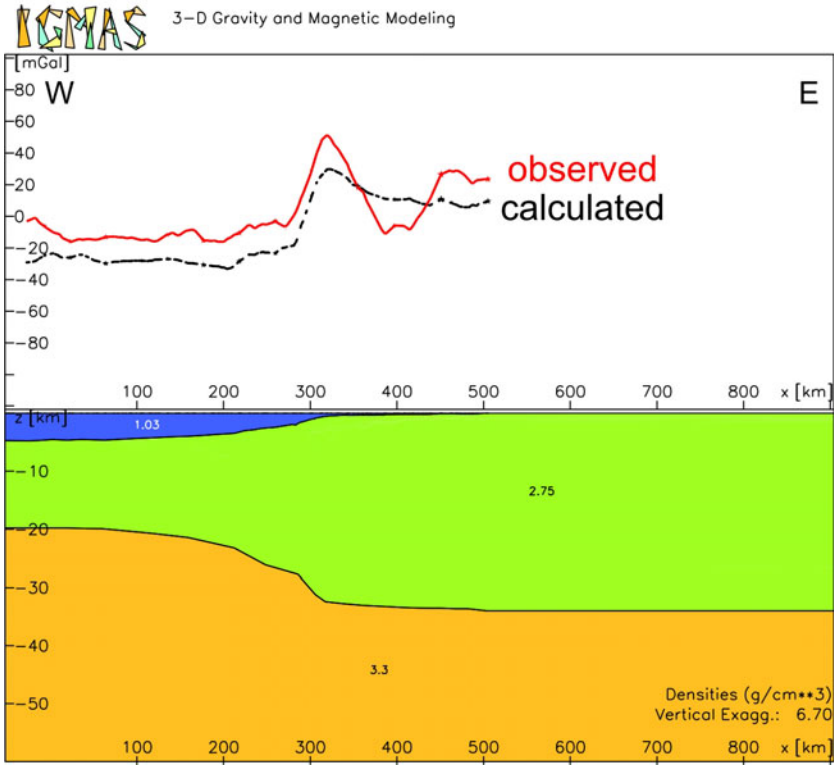

Figure 5: Gravity response for the simple case model: ρ_{crust}=2.75g/cm³, ρ_{mantle}=3.3g/cm³, cd= 34 km.

To summarise, the simple model is able to reproduce the position of the edge-effect anomaly, but does match neither its wavelength nor its amplitude.

Applying a higher/lower average crustal density results in a proportional shift of the resulting Moho depth but yields the same gravity response of the model (cf. Figure 6); it does not match observed variations.

Using a different depth of compensation does, however, result in a different gravity response. The responses for three different compensation depths, 30, 34 and 37 km, using an average crustal density of 2.75 g/cm³ and a mantle density of 3.3 g/cm³ are shown in Figure 7. The resulting geometry of the Moho, calculated in GMS, is the same for each applied depth, but shifted according to the new compensation depth. Not surprisingly, a compensation depth of 34 km results in a Moho depth that is 4 km deeper compared to a compensation depth of 30 km, and 3 km shallower compared to a model of 37 km compensation depth. By comparing the resulting gravity fields two major features are obvious: (1) The three models differ only in the seaward part of the model; and (2) all models reproduce the location of the observed anomaly but fail to match its magnitude. Seaward all curves diverge within a range of -12 to -20 mGal but all converge above the shelf break. All density configurations result in the same shape of the edge-effect anomaly with the same amplitude and wavelength.

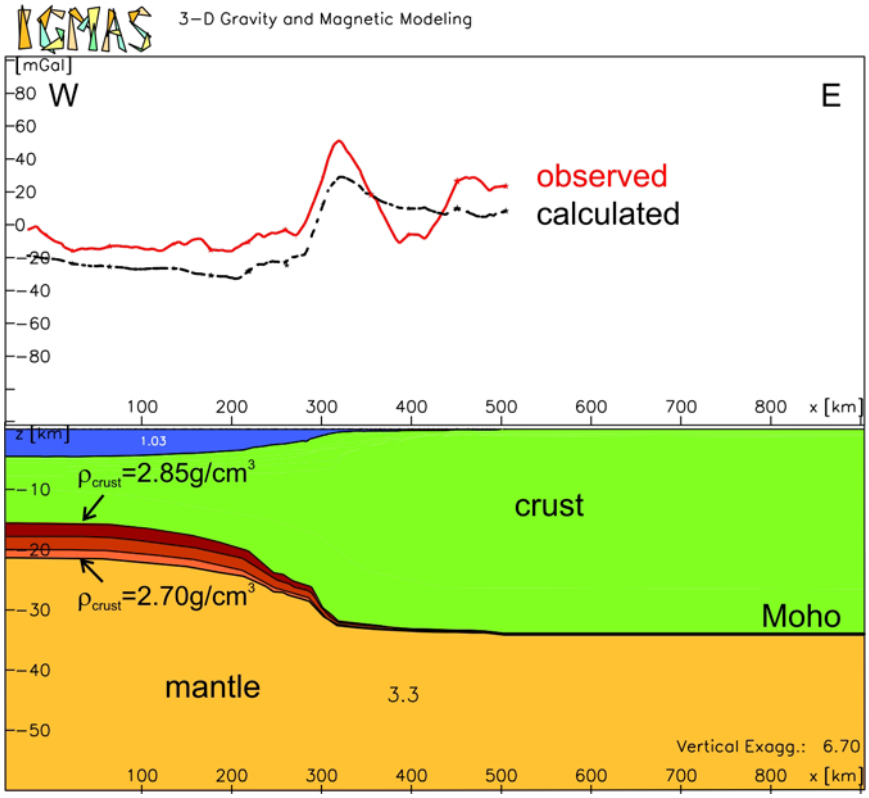

Figure 6: Compilation of all simple case models for a constant compensation depth of 34 km, but a range of crustal densities (2.70, 2.75, 2.80 and 2.85 g/cm³). Different crustal densities result in changing Moho depths (brownish colours), but result in the same respective calculated gravity response.

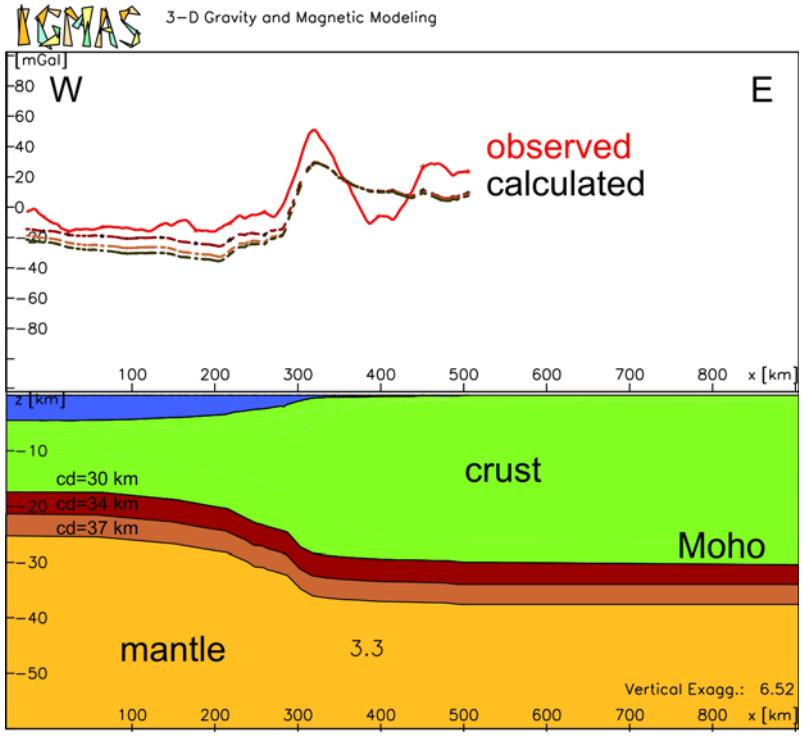

Figure 7: Compilation of all simple case models for a constant crustal density of 2.75 g/cm³, but a range of depth to Moho according to different compensation depths (30, 34 and 37 km) and the respective calculated gravity response.

2.3.2 *Isostatic model including sediments*

This Airy based model includes both the geometry and density of the sediment package that makes up to 18 km of the crust, but the (middle and lower) crust is treated as homogeneous. The Airy approach is applied, therefore, to the load distribution imposed by the present-day water column and the sedimentary layers to derive the Moho depth. Again, different model configurations were tested. Densities for the crystalline crust were varied from 2.7 g/cm³ to 2.85 g/cm³. For the compensation depths values of 30, 34 and 37 km were chosen. In Figure 8, the position of the Moho using a compensation depth of 34 km is shown for two end-member models with crustal densities of 2.7 g/cm³ and 2.85 g/cm³, respectively. The density difference between these two end member models results in the depth to the Moho of the deep water area being 6 km deeper than in a landward position. For a density of 2.7 g/cm³ the Moho shallows to 25 km, and for a density of 2.85 g/cm³ a depth of 20 km is calculated.

Applying realistic density variations in the sedimentary part of the model results in an up to 5 km shallowing of the Moho compared to the simple model with a homogeneous crust.

The gravity response for a crustal density of 2.75 g/cm³ and a compensation depth of 34 km is shown in Figure 9. In the seaward part of the profile, where the observed gravity profile is flat, the response of the model fits the observations. At kilometre 260 along the profile, close to the shelf break, both curves converge and rise parallel to each other.

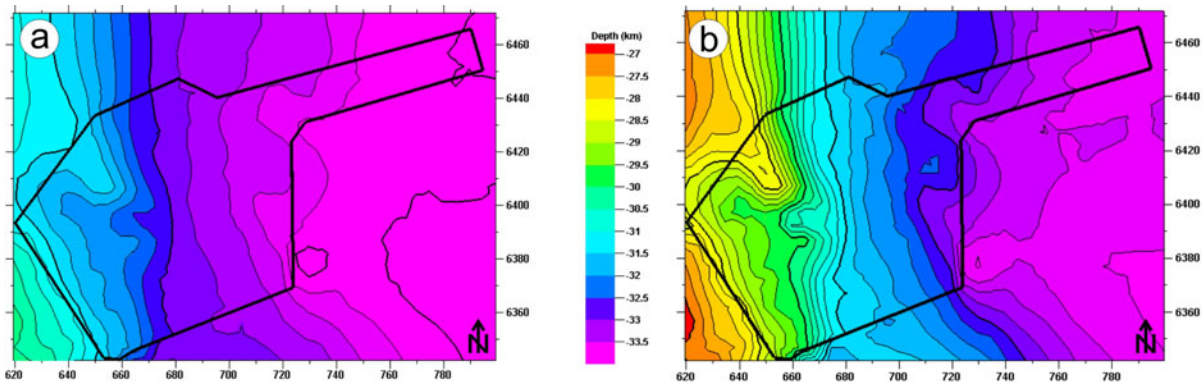

Figure 8: Moho position for 2 end-member models: **a)** crustal density of 2.7 g/cm³; **b)** 2.85 g/cm³ including the geometry of sediments for a compensation depth of 34 km in both cases. Maps are in UTM coordinates (kilometres), Zone -33 S.

In contrast, landward of kilometre 310, above the shelf break, the calculated and observed curves diverge and there is a significant mismatch between the calculated and the observed curves. Thus, this Airy model is able to reproduce the slope of the anomaly in its observed position, but not its wavelength or its amplitude.

To summarise, an Airy-based, isostatically balanced density model including a homogeneous mid to lower crust does not explain the observation of the edge effect anomaly. A mass excess adjacent to the shelf break is needed to resolve this effect.

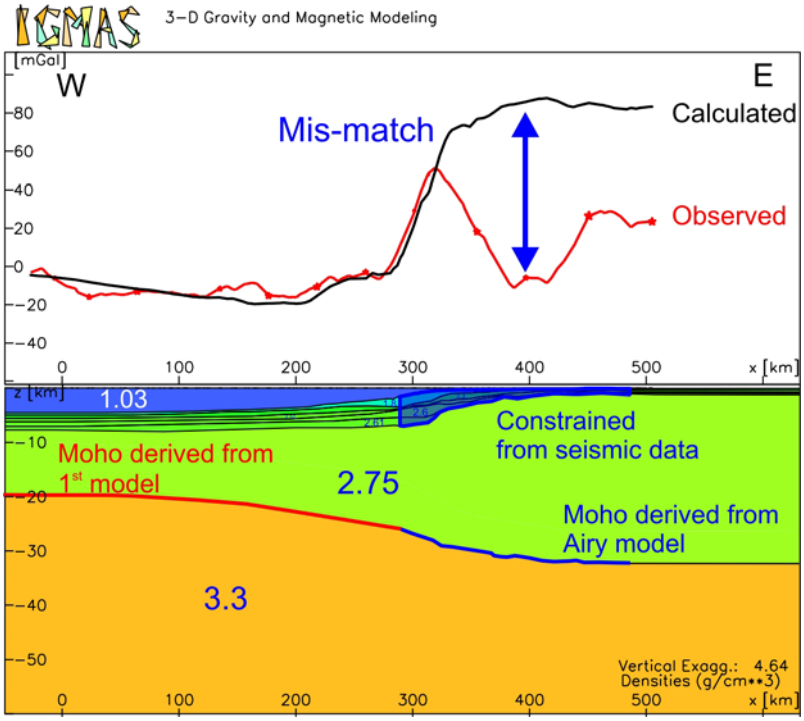

Figure 9: Gravity modelling including the geometry of sediments (for a reference model ρ_{crust}=2.75 g/cm³, ρ_{mantle}=3.3 g/cm³, and cd=34 km).

2.3.3 *Final model considering a sediment cover and a complex crustal configuration*

A common strategy for density-modelling of the crystalline crust is to convert P-wave velocities measured in deep refraction seismic experiments to densities. The closest such deep refraction profile to the study area is the Springbok line (Mahanyele et al., 2004). Along this profile, the transitional lower crust between the oceanic and the continental crust is characterised by high P-wave velocities (> 7 km/s) and high densities (> 3.1 g/cm³). We used the Nafe-Drake curve (e.g. Ludwig et al., 1970) for sedimentary rocks and a correlation from Christensen and Mooney (1995) for igneous and metamorphic rocks (e.g. Fowler, 1996) to derive a grid-based density field from the velocity model.

In order to apply a similar structure to the 3D model, as found in the Springbok line, 6 different layers were defined to represent the middle and lower crust beneath the study area. The lateral density variations of these layers were allowed to range from 2.7 to 3.2 g/cm³. Furthermore, with increasing depth densities also increase. Within the volume of the geological model the position of the Moho is inferred from the isostatic crustal model (reference model: ρ_{crust} = 2.75 g/cm³, cd = 34 km).

For the seaward part of the gravity model we adopted the geometry observed in the Springbok seismic refraction profile. Although the Springbok line is at some distance (~100 km) from the modelled area, we consider it reasonable to project the main features observed there into the working planes of the study area with the assumption that the margin is characterised by a similar 2D structural character along strike.

The configuration of this model was defined by the water column, the sedimentary part, an inhomogeneous middle and lower crust. The position of the Moho was derived from isostatic crustal modelling used in combination with findings from the Springbok line. Figure 10 shows the working plane through the 3D density model with the respective measured and calculated gravity curves

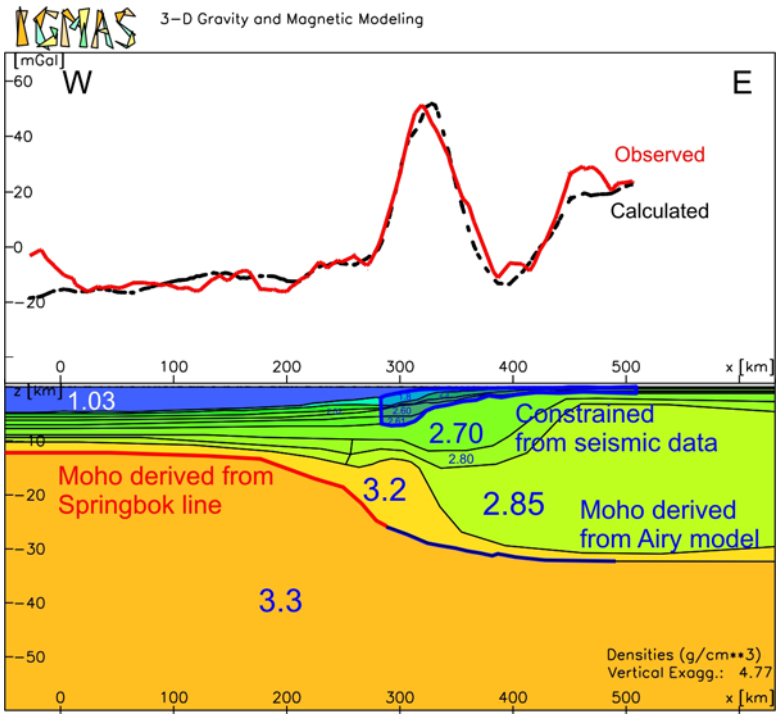

Figure 10: Final model, incorporating an inhomogeneous middle and lower crustal structure.

In the seaward part, the uppermost 10 km are made of regularly layered sediments and crustal units and the Moho occurs at a depth of 12.5 km. Towards the shelf break, east of kilometre 290, the sediment layers reach their maximum thicknesses below the edge-effect anomaly where the middle and lower crust comprises 6 layers of different densities. At this location, the Moho depth increases to more than 30 km, and the observed gravity anomaly reaches its maximum at the shelf break. A thick pile of sediments in the uppermost part of the model replaces much of the water body of the model and forces the calculated gravity curve to rise. In order to compensate for this effect, a higher density contrast is needed to decrease the curve towards the east. To achieve this, a high density body of up to 14 km thickness is required in the lower crust. Remarkably, east of kilometre 320 km, along the profile the thickness of the high density body decreases abruptly. This corresponds to an increase in thicknesses of the adjacent lower-density bodies. This change coincides with a decrease in the amplitude of the gravity curve. Across the entire 3D model area the high density body has an average thickness of 11 km along the strike of the anomaly, and locally is up to 14 km thick (Figure 11). The body thins continuously oceanward, but is limited landwards by a sharp boundary against less dense crustal material.

This crustal model of the African continental margin reproduces the observed edge-effect not only along a single profile (Figure 10), but also in three dimensions. Figure 12 shows a comparison of the measured gravity field and the calculated results in map view across the modelled area.

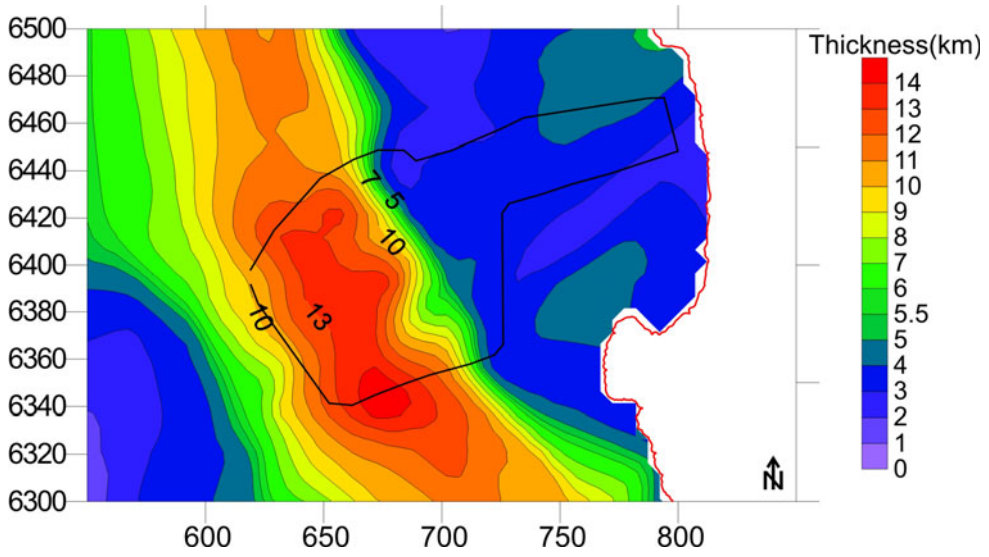

Figure 11: Thickness (in kilometres) of the high density body (3.2 g/cm³) in the lower crust across the 3D geological model derived from gravity modelling. Map is in UTM coordinates (kilometres), Zone -33 S.

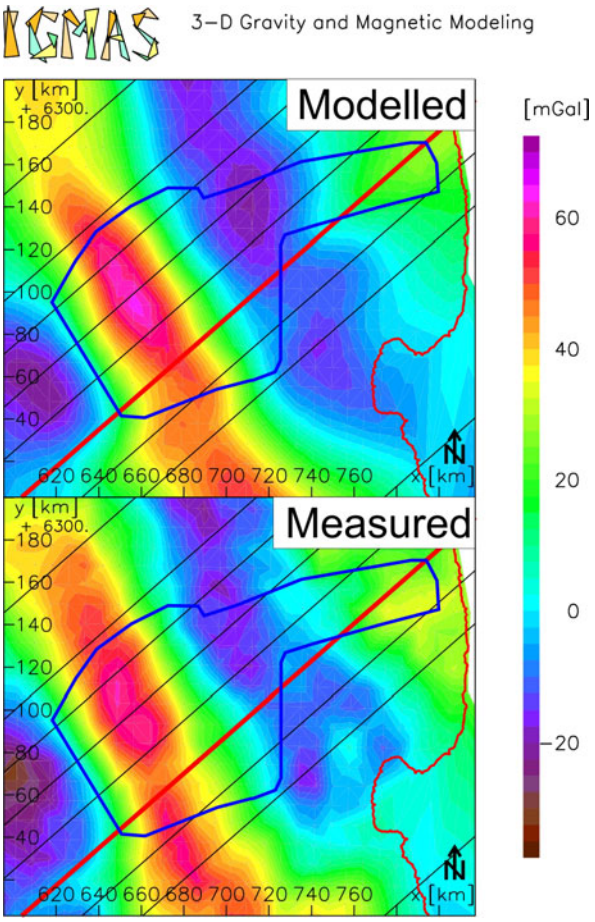

Figure 12: Comparison of measured versus calculated gravity field (interactive working planes are shown as diagonal lines). The red line is the working plane shown in previous figures.

2.4 Discussion

Early models of the edge-effect anomaly fitted observations with an idealized continent-ocean transition. For example, the transition between thick continental crust and thin oceanic crust can produce an asymmetric anomaly (e.g. Sleep and Fuyita, 1997). Such an anomaly would be centred above the transition zone between oceanic and continental crust with a maximum above the continental part and a minimum above the oceanic portion. This model is very sensitive to the underlying geometry. In reality, this theoretical concept of an edge-effect anomaly is more complex. The most obvious reason for this is the load-effect of sediments on the thinned crust. In addition, it is likely that crustal blocks are not completely compensated in terms of local isostasy. Walcott (1972) and Watts (1988) showed the importance of regional compensation and geologic processes (e.g. sedimentation and magmatism) involved in margin evolution.

Watts (1988) proposed that the edge-effect anomaly resulted from all the processes operating at the margin, including rift structures and sediment loading. A "rifting anomaly" results from the margin geometry through its evolution without sediment loading and consists of both a negative and a positive anomaly with a high located above the un-stretched crust and a low above the stretched crust.

This type of anomaly can be reproduced by the simple model, as described above, when a homogeneous crust is affected by an increasing degree of thinning towards the ocean (Figure

6, Figure 7). In such a configuration, water depth alone would balance crustal thinning. The position of the Moho shallows where the water deepens as more high-density material must balance the low-density water. Although the water load and a homogeneous crust create a curve similar to the edge-effect, the calculated gravity response of the model is shifted to lower gravity values. Consequently, the gravity response of the simple model suggests that this type of model is not applicable.

The sum effect of the sediments and the crust are investigated in a further refined model. Again, this model does not reproduce the required gravity decrease landward of the observed high, which is nevertheless observed in the data (Figure 9). These isostatic Airy models do give information on a required crustal geometry based on a certain average crustal density. In detail, they fail to give information on the internal density distribution within the crust. The juxtaposition of the incorporated sediment pile and the homogeneous crust does not create a sufficient density contrast, either because the pile is not thick enough or the crust is not homogeneous. As the sediment thickness resolved in this model is quite large (up to 12 km) and in the average range for continental margins, the misfits are more likely related to deep crustal heterogeneities. Indications for such variations in deep crustal structures come from seismic refraction data. The Springbok line, and other refraction profiles elsewhere reveal significant lateral variations in seismic velocity of the lower crust perpendicular to the passive margin as well as the presence of lower crustal high velocity bodies (e.g. Holbrook et al., 1994).

Bauer et al. (2000) have demonstrated that the observed edge-effect anomaly offshore Namibia is related to the superposition of topography effects and lateral density variations alone, but that the width and amplitude of the observed gravity anomaly requires dense material in the middle and lower crust.

Assuming a positive correlation between seismic velocity and density allows the construction of an improved gravity model that closely reproduces the edge-effect anomaly (Figure 10). Beside the geological model information, such a gravity model includes a heterogeneous middle and lower crust. In this model a high density body in the lower crust is spatially consistent with a high velocity body along the Springbok profile. The positive anomaly in this case appears to be a result of the juxtaposition of the high densities in the middle and lower crust at the continent-ocean transition and the lower densities of the continental crust. In our gravity model, this lower crustal body has a density of 3.2 g/cm^3 (and the respective P-wave velocities are > 7.2 km/s). The high velocities and the modelled high densities suggest that this material is mafic in nature. Similar conclusions have been proposed for the Namibian margin by Stewart et al. (2000) and Gladczenko et al. (1998). In addition, these high density, high velocity bodies have also been found on other volcanic margins, for example the offshore eastern United States (Talwani and Abreu, 2000). In the North Atlantic the characteristic P-wave velocities commonly range within this zone from 7.1 - 7.7 km/s (e.g. Eldholm et al., 2000; Gernigon et al., 2003).

From this observation arises the question how to interpret the high velocity-high density body?

Offshore and onshore refraction and reflection seismic experiments in Namibia show that the zone of high average P-wave velocities (> 7 km/s) is situated directly beneath a wedge of seaward dipping reflectors (Bauer et al., 2000). These reflectors in the transition zone between continental and oceanic crust are interpreted to consist of basalt flows and intercalated sediments. A seaward thickening wedge has been drilled in the study area in well A-C1 and found to consist of mainly basaltic lavas (Gerrard and Smith, 1982). This seaward thickening wedge has been interpreted as corresponding to the coeval postulated

seaward dipping reflectors, and to represent extensive basaltic volcanism during the rifting phase of continental break-up (Hinz, 1981; Eldholm et al., 1995). Along the Springbok seismic refraction profile, nearby the Namibian/South African border, a high velocity body (> 7 km/s) is present in the lower crust below this seaward dipping wedge.

Offshore Namibia, the high velocity body is interpreted to represent the intrusive counterpart of the seaward dipping reflector wedge. The base of this high velocity body correlates with the seismic Moho. Bauer et al. (2000) favour the interpretation of this zone to be completely underplated mafic igneous material (Holbrook et al., 1994), whilst alternative interpretations assume heavily intruded extended continental crust (White et al., 1987).

McKenzie (1978) proposed a passive rifting model for basin evolution. Lithospheric thinning is accompanied by upwelling of the asthenosphere to maintain the isostatic equilibrium. A few years later Foucher et al. (1982) put forward a model of melt generation as a result of passive asthenosphere upwelling. White and McKenzie (1989) generally agreed with Foucher's ideas and argue that lithospheric stretching and thinning results in passive upwelling of the asthenosphere to fill the created space. Large quantities of melts, therefore, are a product of the decompressional processes. But crucial components of this model are increased temperatures, involving a "hot" mantle plume leading to the formation of large quantities of magmatic rocks.

This excessive magmatism may result in the emplacement of a mafic material, at present preserved as high density, high velocity bodies. Features like the lower crustal body can be also explained in an alternative way.

Gernigon et al. (2004) suggest that melt volumes along continental margins can originate from mechanical processes alone, and do not require the coeval influence of an involved mantle plume. Assuming realistic thinning factors, they show with 2D numerical calculations that a mantle plume is not a pre-requisite to generate a volcanic margin. Moreover, volcanic margin formation may simply be a consequence of decompressional melt production. In these models the lithosphere is extended and thinned, while the crust is warmed and mantle material rises. This leads to decompressional melting in the head of the rising mantle material (Van Wijk et al., 2001). Melt production is dependent on the assumed amount of extension. At low stretching factors ($\beta < 2$) little melt is produced. At high extension ($\beta > 5$) significant melting occurs during the break-up process in a depth range from 20 to 50 km (e.g. Van Wijk et al., 2001; Gernigon et al., 2006).

However, if a plume is involved it would influence the volume of produced melt. The difference between melt produced by decompressional melting and by a plume is a function of the magnesium content of the melts.

Melt generated from abnormally hot mantle material (plume) has a higher concentration of magnesium in comparison to melt generated from normal mantle material. This enrichment in magnesium causes an increase of igneous rock velocities from 6.8 km/s to 7.2 km/s or higher (White and McKenzie, 1989).

Trumbull et al. (2002) argue for a plume influence off Namibia, an area close to Walvis Ridge. They show that the high observed P-wave velocities in a depth range from 7 – 30 km can be modelled with a lower crust of magnesium-rich basaltic composition along two transects offshore Namibia. The enrichment in magnesium indicates increased mantle temperatures perhaps related to the coeval Tristan da Cunha Hotspot activity. In contrast, they find no indication for a plume influence in the south close to our study area.

Based on the analysis of P-wave velocities along the Springbok seismic refraction profile Trumbull et al. (2002) argue against the possibility that the high velocities in the lower crust are related to the influence of the Tristan da Cunha plume. The velocity structure in the

lower crust corresponds to gabbros without elevated magnesium content. This is consistent with results obtained onshore, where compositional signatures found in dolerite dikes indicate the same conclusion. To summarise, the influence of a plume on the high velocity body appears to be less probable in the study area than farther north, offshore Namibia.

An interesting aspect concerning the geometry of the high density body within the gravity model is its sharp boundary against the "normal" crystalline continental crust. This is consistent with observations in the MAMBA seismic refraction experiments offshore Namibia where a strong velocity gradient represents the landward termination of an intrusive section, whereas the seaward edge is much more gradual (Bauer et al., 2000). The lack of a transition zone is used to support the idea that intruded igneous material causes this strong gradient rather than thinned and rifted continental crust which is heavily intruded.

2.5 Conclusions

Three types of crustal models and the respective gravity response have been used to derive the crustal-scale density structure of the continental margin beneath the Orange Basin of the west coast of South Africa consistent with the observed edge-effect anomaly along this margin. Although modelling of potential field data always yields non-unique results, we have reduced the ambiguity to a significant degree by combining isostatic findings and gravimetric modelling with constraints from deep seismic refraction data.

We find that:

(1) An Airy-type compensation with a laterally homogeneous crust is only partly consistent with observed gravity data, though the edge-effect anomaly is reproduced in position.

(2) A similar model incorporating sediments to explain the gravity low landward of the edge-effect anomaly is also not sufficient to reduce the misfit between observed and modelled gravity. A density contrast caused by a 12 km thick sequence of sediments is insufficient to cause the observed anomaly.

(3) Only a model that considers the sedimentary pile and an inhomogeneous mid- and lower crust comprising a high density body (3.2 g/cm^3) of considerable thickness (~ 11 km) holds a sufficient density contrast to reproduce the observed edge-effect anomaly.

The high density material is likely mafic in nature and related to magmatic activity during the break-up phase of continental margin formation.

Acknowledgements

This work has been done in the framework of INKABA yeAFRICA at the GeoForschungsZentrum Potsdam.

We are grateful for the constructive comments of the reviewers M. de Wit and R. Domoney.

Isostatic modelling was performed with the Geological Modelling System (GMS) developed at GeoForschungsZentrum Potsdam, Department Organic Geochemistry under the leadership of Prof. Dr. U. Bayer.

We thank H.-J. Götze and S. Schmidt, University of Kiel, for the 3D gravity modelling programme IGMAS.

Maps were plotted using GMT 4.0 (http://gmt.soest.hawaii.edu/).

This is INKABA yeAFRICA contribution number 21.

3 Deep structure of the western South African passive margin - results of a combined approach of seismic, gravity and isostatic investigations

Abstract

The passive margin of the South Atlantic shows typical features of a rifted volcanic continental margin, encompassing seaward dipping reflectors, continental flood basalts and high-velocity/density lower crust at the continent-ocean transition, probably emplaced during initial seafloor spreading in the Early Cretaceous.

The Springbok profile offshore western South Africa is a combined transect of reflection and refraction seismic data. This paper addresses the analysis of the seismic velocity structure in combination with gravity modelling and isostatic modelling to unravel the crustal structure of the passive continental margin from different perspectives.

The velocity modelling revealed a segmentation of the margin into three distinct parts of continental, transitional and oceanic crust. As observed at many volcanic margins, the lower crust is characterised by a zone of high velocities with up to 7.4 km/s. The conjunction with gravity modelling affirms the existence of this body and at the same time substantiated its high densities, found to be 3100 kg/m³. Both approaches identified the body to have a thickness of about 10 km. Yet, the gravity modelling predicted the transition between the high-density body towards less dense material farther west than initially anticipated from velocity modelling and confirmed this density gradient to be a prerequisite to reproduce the observed gravity signal.

Finally, isostatic modelling was applied to predict average crustal densities if the margin was isostatically balanced. The results imply isostatic equilibrium over large parts of the profile, smaller deviations are supposed to be compensated regionally. The calculated load distribution along the profile implies that all pressures are hydrostatic beneath a depth of 45 km.

3.1 Introduction

The structure of the southwest African passive continental margin is still enigmatic as very little deep seismic data is available. We present the results of a combined on- and offshore seismic refraction experiment designed to image the deep structure of the margin. The resultant velocity-depth model is additionally constrained with free-air gravity data and finally used for isostatic calculations.

The investigated profile on- and offshore South Africa is located between the Orange River to the north and the Olifants River to the south (Figure 13). The profile provides a transect through the westernmost Kalahari Shield, the southern edge of the Gariep Belt, the continental crust that has been stretched during the Mesozoic (>130 Ma) and the adjacent oceanic crust with cooling ages of ~130 Ma.

A special focus was set on the distribution of masses and on implications for the isostatic state of the system. 2D seismic raytracing yielded the velocity structure across the margin that was further constrained by gravity modelling especially where the seismic data quality

was only moderate. Finally, isostatic modelling assuming local isostasy was used to evaluate the isostatic state of the margin. We explore how far the results from velocity, gravity and isostatic modelling are consistent and to what extent these findings provide information on the crustal structure of the margin.

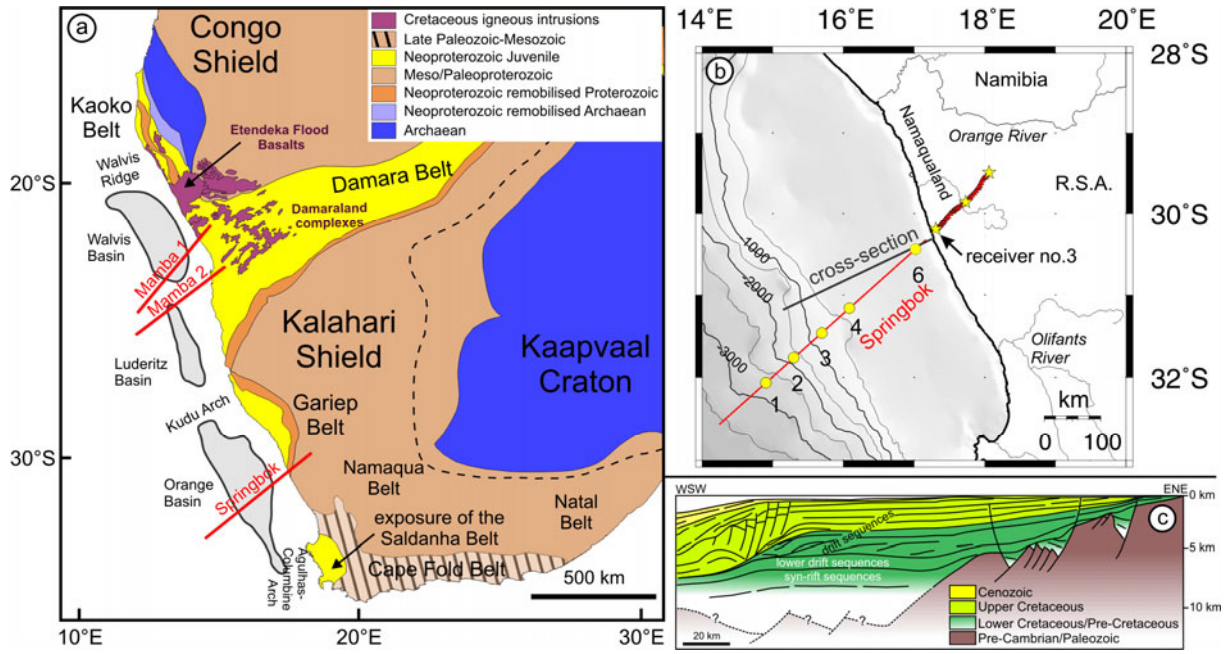

Figure 13: a) Simplified geology of south-western Africa (modified after de Wit and Stankiewicz, 2007) including the old cratons and surrounding mobile belts which accreted during the Damara Orogeny. Along the Atlantic margin three major sedimentary basins are shown in combination with the location of the Springbok seismic refraction/reflection profile crossing the Kalahari Shield, running through the offshore Orange Basin and ending in approximately 3600 m water depth in the seaward domain of the profile. Farther north are the positions of the MAMBA profiles given in red. **b)** Bathymetric map (Sandwell and Smith, 1997) of the South African margin with the Springbok profile in red. Yellow circles indicate the positions of the OBHs offshore. 40 onshore receivers are plotted as red triangles, overlain by 3 stars indicating the position of the onshore borehole shots. An arrow indicates the position of land station 3. **c)** Cross-section of the south-western African continental margin illustrating the geometries of syn- and post-rift sequences within the Orange Basin (modified after Brown et al. 1995).

3.2 Geological setting

The Springbok profile is 500 km long and crosses the western margin of the Republic of South Africa (R.S.A.) at 31°S. In the offshore part, the profile starts at 3600 m water depth and runs through the central part of the Orange Basin in the shelf region (Figure 13). Near the shoreline the foothills of the deeply eroded, coast-parallel Panafrican Gariep Belt are crossed and the profile extends 100 km on land, where the topography is elevated to a maximum of 1000 m. At the landward termination of the Springbok profile the new study can be compared with the results of Green and Durrheim (1990) in which a refraction seismic experiment was carried out to study the deep crustal structure of the South African continent in the region of the Kalahari Shield. The latter formed when ocean-like crust was emplaced

over the Kaapvaal Craton and its surrounding mobile belts. This stabilized the belt systems against the craton approximately 1 Ga ago (Eglington and Armstrong, 2003).

Subsequently, in the Damara orogeny, a large network of Proterozoic to early Paleozoic orogenic belts developed through accretion coeval to the construction of Gondwana which surrounds and welds together the older Congo, Angola, and Kalahari Cratons (e.g. Grunow et al., 1996). In western Gondwana this belt system comprises the Kaoko, Damara, Gariep, and Saldanha Mobile Belts that have their equivalents on the South American side, e.g. the Ribeira Belt (Porada, 1979).

The Damara Belt, and its coast-parallel extension, the Kaoko and Gariep Belt underlie the passive margin offshore Namibia.

The Gariep Belt is restricted to the coast in southern Namibia and northern South Africa and is the only orogenic belt in which oceanic crustal material has been described. Metasedimentary sequences similar to the Damara Belt sequences represent continental rift conditions whereas the western units, separated by a suture zone, comprise metabasalts (Frimmel and Frank, 1998).

The Damara Orogeny was succeeded by a tectonically tranquil period, dominated by erosional and sedimentary processes until the opening of the South Atlantic in Early Cretaceous times around 136 Ma (Brown et al., 1995; Reeves and de Wit, 2000; Macdonald et al., 2003). The continental break-up of Africa and South America was accompanied by massive, transient volcanic activity which resulted in the emplacement of the Cretaceous igneous intrusions, also called the South Atlantic Large Igneous Province. This province encompasses the Paraná-Etendeka continental flood basalts and the offshore counterpart of extrusive complexes represented by a wedge of seaward-dipping reflectors (Hinz, 1981; Gladczenko et al., 1997; Talwani and Abreu, 2000; Bauer et al., 2000). Magmatic activity is attributed to the Tristan da Cunha hotspot activity and the emplacement of the seaward-dipping reflector wedge is supposed to be generated by a transient magmatic pulse (Gladczenko et al., 1997). The Etendeka Province is exposed onshore as eroded remnants of thick basaltic sequences, intrusive subhorizontal dolerite sills, and a number of large subvolcanic ring intrusions, known as the Damaraland Complexes (Milner et al., 1995, Trumbull et al., 2000). These ring complexes represent the eroded roots of ancient volcanoes which were active during flood volcanism (Marsh et al., 2001). South of the Walvis Ridge, offshore Namibia, and R.S.A. several Late Mesozoic basins are present, namely the Walvis Basin, Luderitz Basin, and Orange Basin that cumulated some kilometres of post break-up sediments.

The post break-up Orange Basin overlies basins of Early Cretaceous age that developed during several rift-stages prior and during the break-up of the South Atlantic Ocean. To the north the Orange Basin is bound by the Kudu arch and by the Agulhas-Columbine arch to the south (Muntingh and Brown, 1993). Post-rift sedimentary successions outline the basin which had its main depocenter offshore Namaqualand south of the present-day Orange River mouth since the drift-onset.

The underlying syn-rift successions are generally isolated grabens and half-grabens that trend approximately parallel to the present-day margin. Graben infill consists predominantly of Upper Jurassic and Lower Cretaceous coarse continental clastics, fluvial/lacustrine sediments and volcanic rocks of variable thickness (Muntingh and Brown, 1993).

3.3 Modelling

3.3.1 Springbok seismic experiment

In April-May 2003 a geophysical experiment was carried out to study the shallow to deep crustal structure of the western margin of the Republic of South Africa (R.S.A.). The project was initiated by a German-South African consortium consisting of the GeoForschungsZentrum Potsdam (Germany), the Bundesanstalt fuer Geowissenschaften und Rohstoffe Hannover (Germany), and the Council for Geoscience (R.S.A.). The campaign included reflection and refraction seismic profiling offshore and partly onshore, where traverses have been surveyed parallel and perpendicular to the ocean-continent transition zone (Mahanyele et al., 2004; Schnabel et al., 2006). In this paper, the data from the Springbok profile (Figure 14) are used to determine the seismic velocity structure of the crust along the transect. This information forms the starting point for the gravity modelling described in the subsequent sections 4.2 and 4.3.

Wide-angle reflection/refraction seismic data were collected by 5 ocean bottom hydrophones (OBH) and 40 seismometers (3-component, 1 Hz) onshore (Figure 13 b). Air-gun shots (volume ca. 70 l) were fired every 175 m generating signals that could be recorded at a maximum distance of 250 km. Additionally, three bore-hole shots were executed on land. Multichannel seismic (MCS) data have been collected along the offshore part of the Springbok profile to provide structural, reflection seismic images across the margin. For the purpose of the velocity modelling presented in this paper, these data were included in that the geometry of the major sedimentary layers could be interpolated between the regions covered by the OBH data.

3.3.2 Velocity modelling

To determine the velocity model across the continental margin modelling based on travel time data was carried out by the use of the forward and inverse modelling package RAYINVR (Zelt and Smith, 1992). The data were analysed in the common receiver domain. Initial processing included band pass filtering, deconvolution, and frequency-wavenumber filtering. Travel times of reflected and refracted phases were determined and used as input information for the subsequent velocity modelling. Forward modelling with 2-D ray tracing was applied. Subsequently, the model was further updated by the use of damped least squares inversion. This procedure was applied to parts of the model with high ray coverage. Reflected events with limited lateral extension were modelled as floating reflector features. In other words, those boundaries (reflection segments) were established in the model which are not associated with a change in seismic velocity. Considering the general objective of this procedure, this ray-based modelling is comparable with pre-stack migration of seismic reflections, without obtaining the resolution and accuracy of the latter method.

Examples of the data and the ray tracing along the profile are shown in Figures 2-4. The data collected by OBH 1, located in the oceanic part of the profile, are displayed in the upper panel of Figure 14a. At the offset range of +- 75 km several phases with apparent velocities between 2.0 and 6.2 km/s are identified and picked (middle panel in Figure 14b).

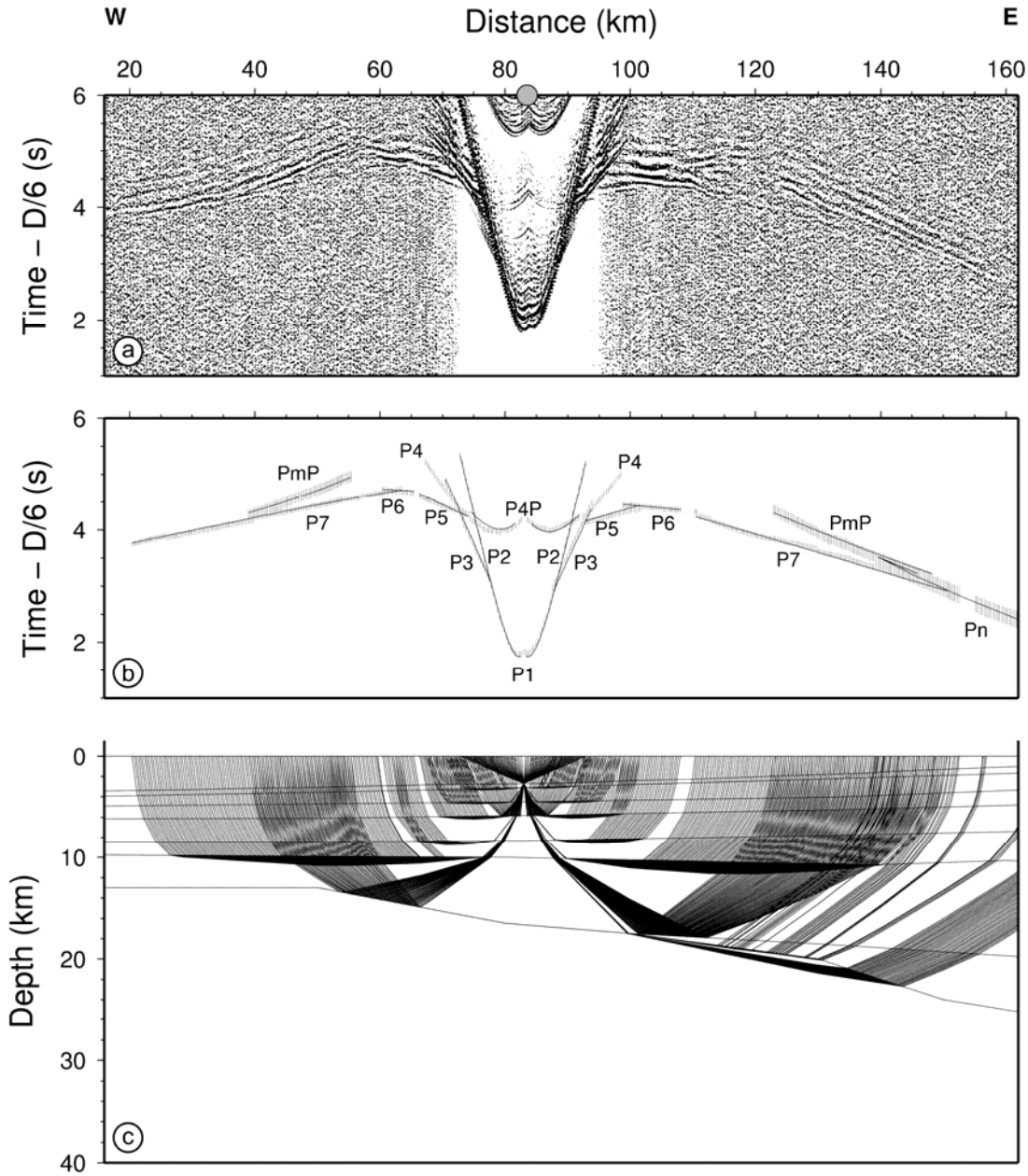

Figure 14: a) Receiver gather for OBH 1 from km 20 to km 160 along the Springbok profile. The vertical axis corresponds to reduced travel times (reduction velocity is 6 km/s). Distances represent the model coordinates along the profile and the grey circle indicates the position of OBH 1. **b)** Observed and calculated travel times based on the final P-wave velocity model. The arrival P1 refers to the water wave, arrivals P2, P3 and P4 correspond to the marine sedimentary layers the base of which is a prominent reflection (P4P) that refers to the seismic basement. The underlying crust can be subdivided into 3 sections (P5, P6, P7) beneath this section the Moho reflection PmP can be identified. Pn - refracted wave from the upper oceanic mantle. **c)** Model section showing ray paths for OBH 1.

The ray tracing demonstrates the coverage of the model around the OBH location (lower panel in Figure 14c). The arrivals P2, P3, and P4 correspond to the marine sedimentary layers 2, 3, and 4 with velocities of 1.8, 2.4, and 3.2 km/s. The boundary underneath this package is also associated with a prominent reflection (P4P) that corresponds to the seismic basement. The crustal section underneath is divided into 3 layers with velocities from top to bottom of 4.7, 6.0 and 7 km/s, respectively. Moho reflections PmP can be identified that are reflected at 12 to 15 km depth. An example for the modelling of the transitional crust is shown for OBH 2

(Figure 15). For the upper sedimentary section, seismic phases P2, P3, and P4 are used to model layers 2, 3, and 4 with velocities of 1.8, 2.4, and 3.1 km/s, very similar to the modelling of the OBH 1 data shown in Figure 14. The seismic basement is associated with the boundary between layers 4 and 5.

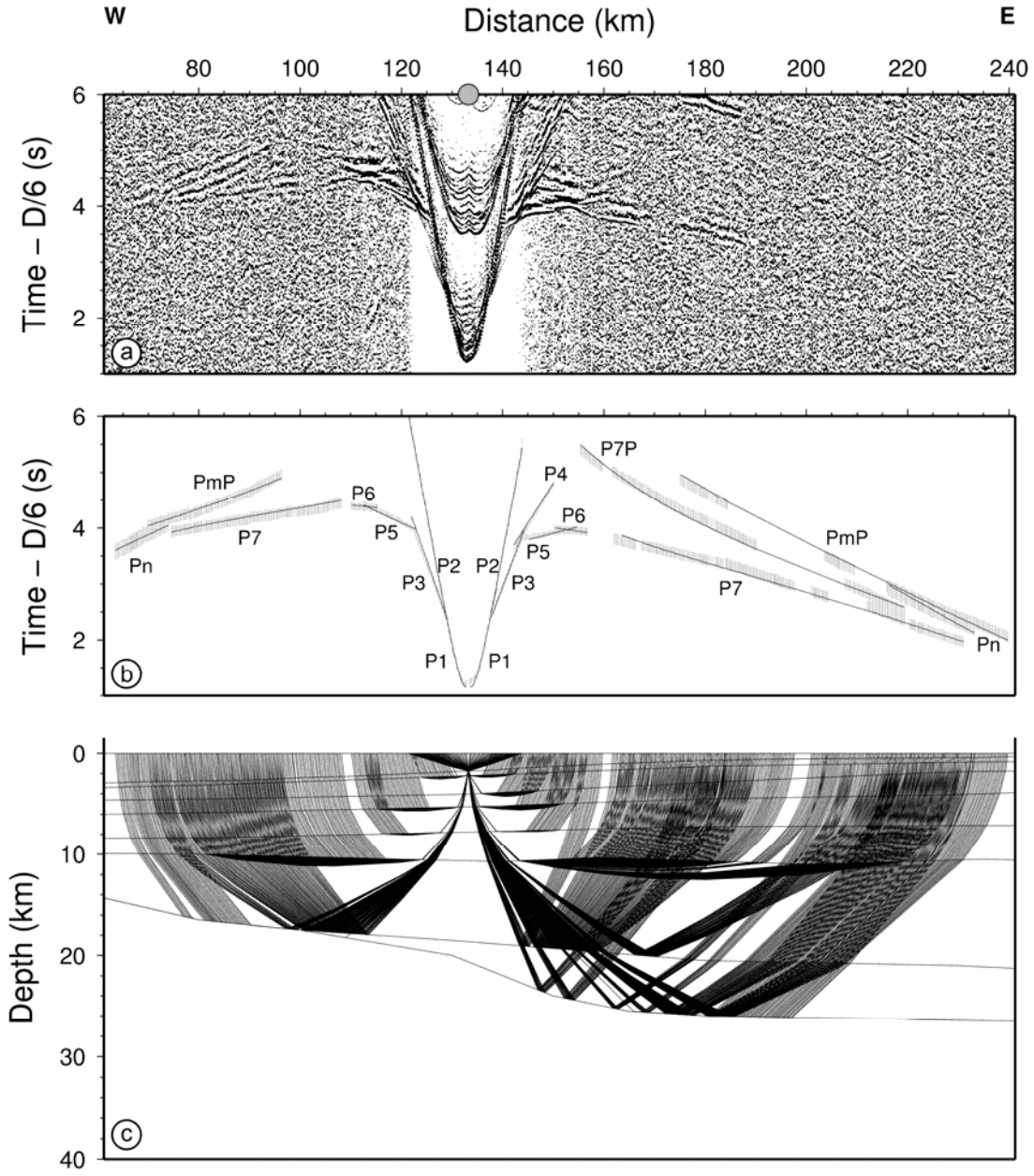

Figure 15: a) Receiver gather for OBH 2 from km 70 to km 240 along the Springbok profile. The vertical axis corresponds to reduced travel times (reduction time is 6 km/s). Distances represent the model coordinates along the profile and the grey circle indicates the position of OBH 2. **b)** Observed and calculated travel times based on the final P-wave velocity model. The arrival P1 refers to the water wave, arrivals P2, P3 and P4 correspond to the marine sedimentary, P4P refers to the seismic basement. The underlying crust is divided into 4 layers based on the modelling of the refracted arrivals P5, P6, P7, and the P7P reflection arrivals. The latter corresponds to the reflection from top of the lowermost crustal body. Arrival PmP refers to the Moho reflection and Pn corresponds to a refracted wave from the upper oceanic mantle. **c)** Model section showing ray paths for OBH 2.

In contrast to OBH 1, the wide-angle reflection from this boundary (P4P) is less pronounced. The upper basement layer 5 is characterised by velocities of 5.1 km/s which is slightly higher than at OBH 1 (4.7 km/s). Layer 6 shows a slight landward increase in velocity and thickness comparing OHB 1 and 2. An additional lower crustal body 7 was modelled landward of 110 km profile distance with velocities between 7.3 and 7.4 km/s. The top of this body is associated with the wide-angle reflections P7P. The depth of this boundary varies between 17 km at 110 km and 21 km at 200 km profile distance. The Moho depth was modelled with PmP wide-angle reflections and increased from 18 km at 110 km to 26 km at 200 km profile distance.

Figure 16 shows data and the corresponding ray tracing for land station 3 (location indicated in Figure 13). The smallest offsets of 21 km correspond to the distance of the seismometer on land to the air-gun location nearest to the coast. Upper crustal refracted arrivals P6 are identified and were modelled with velocities between 5.9 km/s at the surface and 6.3-6.5 km/s in the middle crust. Lower crustal velocities of 6.7 to 7.0 km/s were determined by the use of PmP reflected arrivals. The events named Pc1P and Pc2P were modelled as floating reflector segments which are not associated with a change of velocity at these boundaries. However, the location of these segments appears to be related with large velocity anomalies in the middle and lower crust in those regions. Ray path coverage provides a measure for the resolution of the model along the profile (Figure 17) and the derived final velocity model is shown in Figure 18.

The offshore section is characterised by a sedimentary succession of 3 distinct layers with velocities of 1.8, 2.4, and 3.0-3.5 km/s. The sediments diminish to a thickness of a few hundred metres landward of the shelf break. Onshore, velocities of 6.0 km/s at the surface indicate that there is no sedimentary section in this region. Similar observations were reported by Green and Durrheim (1990). This is most likely related to the fact that inversion and erosion occurred at least since the Tertiary in this area (Doucouré and de Wit, 2003) and led to exposure of crystalline rocks at present. The crustal structure along the profile can be divided into 3 major sections: (1) Normal oceanic crust can be identified at distances between 0 and 50 km. The crust shows a typical structure with velocities of 4.5-5.0 km/s and 6.2 km/s corresponding to the extrusive flows and sheeted dikes (layer 2A and 2B) and a layer with velocities of 7 km/s corresponding to the gabbroic layer 3 (e.g. Spudich and Orcutt, 1980; Pluijm and Marshak, 2004; Raum et al., 2006). (2) Transitional crust is encountered at distances between km 50 and km 250. The high velocities of 6.9 – 7.4 km/s found in the middle and lower crust in this region are a typical feature of rifted volcanic margins. Such high crustal velocities are commonly interpreted as heavily intruded crust in a developing continental rift and underplated bodies resulting from enhanced decompressional melting by mantle upwelling (e.g. White and McKenzie, 1989; Mjelde et al.; 2002; Raum et al., 2006). Following the interpretation of MCS reflection seismic data, this section is overlain by successions of volcanic flows and sediments forming the typical extrusive counterpart of the igneous crust at volcanic rifted margins (Talwani and Abreu, 2000, Schnabel et al., 2006). (3) Continental crust is modelled at distances between 250-300 and 500 km. The data provide no constraints to divide the crustal section into upper and lower crust in terms of a distinct velocity contrast but indicate a continuous increase of velocity between both layers. The crustal velocities vary between 5.9-6.1 km/s at the surface and 6.7-7.0 km/s at the Moho boundary. The inversion of P6 and PmP travel times revealed features of increased velocities in the middle and lower crust in the coastal region less than 50 km wide. Ray-based modelling of reflected events showed that these regions with high velocities are associated with prominent wide-angle reflections.

The final velocity model was used to calculate an initial density model using well-established velocity-density relationships as described in subsequent section 4.2. From this point the model was calibrated with free-air gravity data to cross-check the results of the velocity modelling.

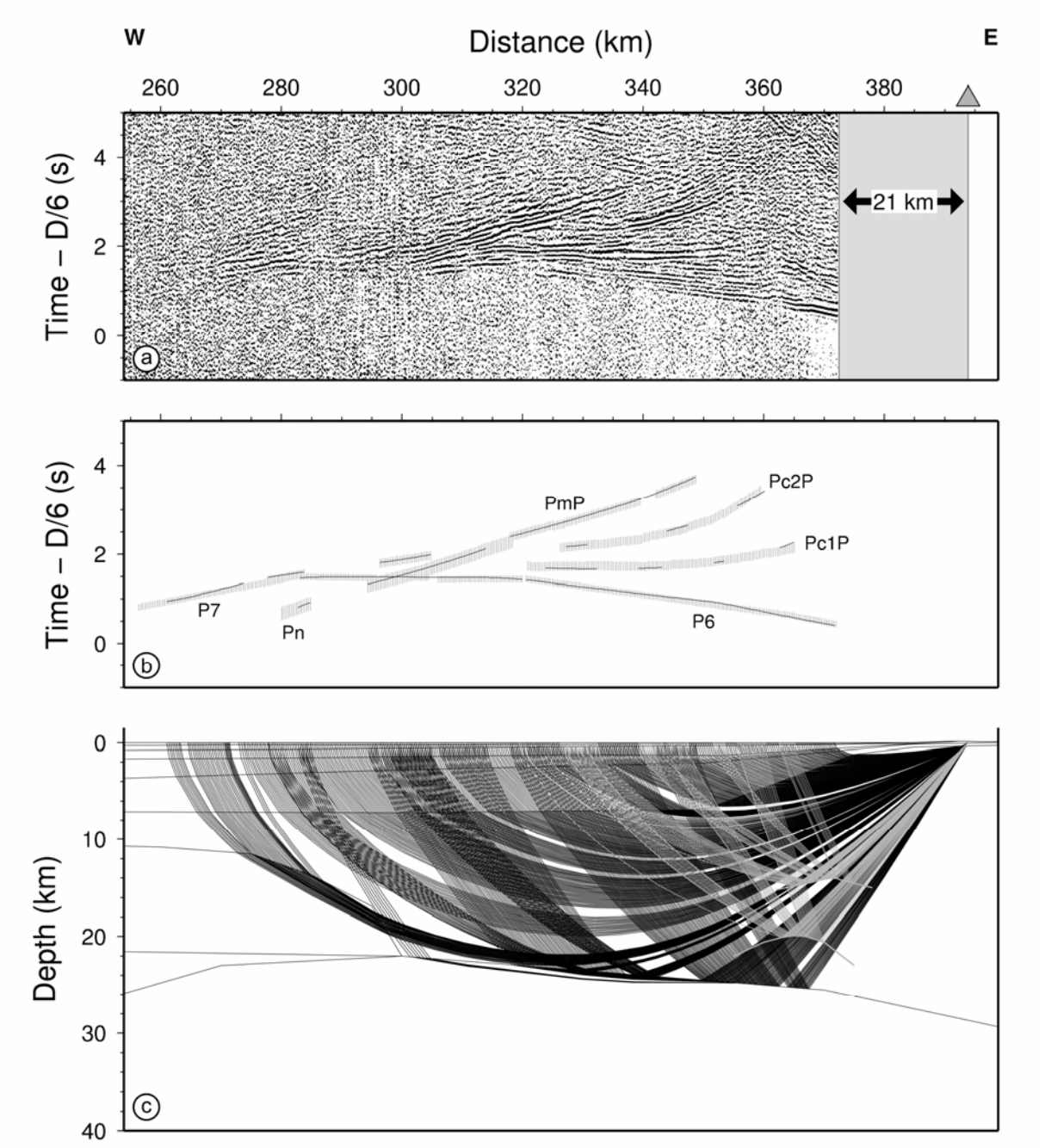

Figure 16: a) Receiver gather for the onshore receiver station 3 (for location see Fig.1b). The smallest offsets of 21 km correspond to the distance of the seismometer on land to the air-gun location nearest to the coast. The vertical axis corresponds to reduced travel times (reduction velocity is 6 km/s) and the grey triangle indicates the position of land station 3. Distances represent the model coordinates along the profile. **b)** Observed and calculated travel times based on the final P-wave velocity model. **c)** Model section showing ray paths for land station 3.

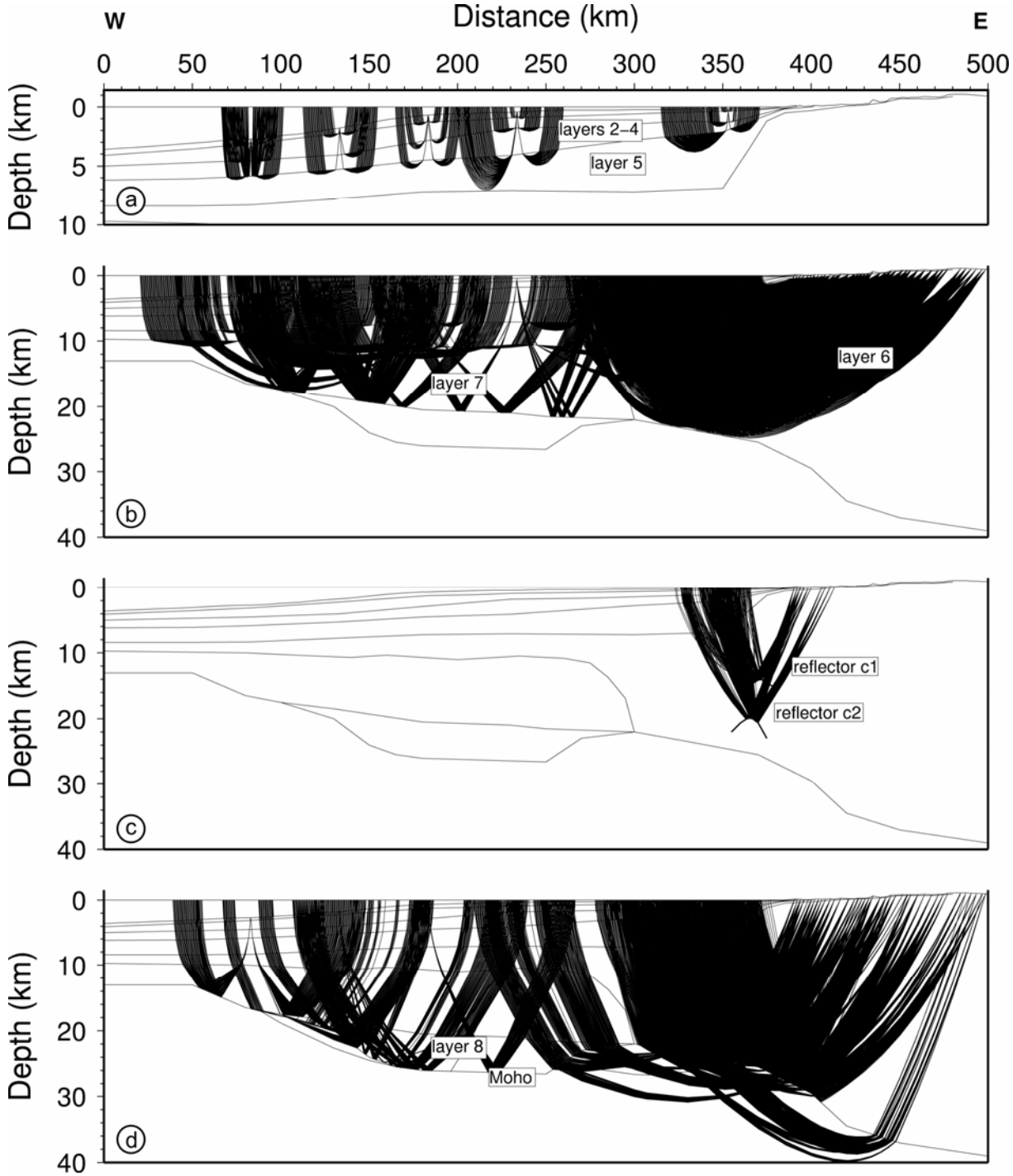

Figure 17: Figure of the ray paths in the model. Panel **a** shows the ray paths for P3 and P4 which correspond to the marine sedimentary layers and also the P4P which corresponds to the seismic basement. Panel **b** shows the ray paths for P5, P6, P7, and P7P which travel through the mid to lower crust. Panel **c** images the ray paths for the modelled floating reflectors Pc1P and Pc2P. Panel **d** shows the ray paths for P8, PmP and Pn.

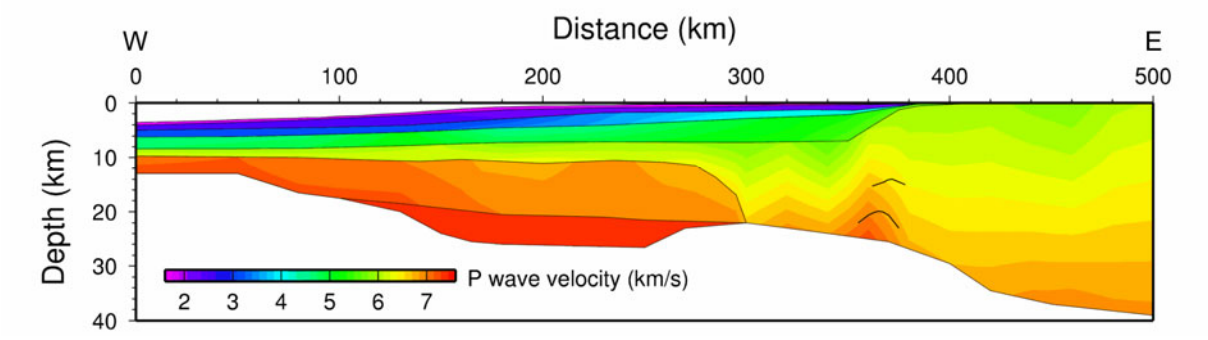

Figure 18: Final velocity model. Black lines indicate model boundaries. Between km 0 and km 50 the velocity distribution indicates typical oceanic crust, followed eastward by a zone of transitional crust and from km 275 on velocities of typical continental crust is modelled.

3.3.3 Gravity field

Figure 19 shows the marine free-air gravity anomaly across the study area which was extracted from Sandwell and Smith (1997) using the 1-min grid. Nearby the border from South Africa to Namibia, the marine gravity field is dominated by the so called "edge-effect" anomaly (Figure 19). This feature is an elongated positive, free-air anomaly and is commonly observed at passive continental margins (Watts and Fairhead, 1999). The gravity anomaly has its maximum above the shelf break and trends parallel to the margin although with a variation in wavelength and amplitude.

Farther offshore a second positive anomaly (Figure 19) was identified by Bauer et al. (2000). This feature is most pronounced between 27°S and 33°S although to the north it becomes less distinct and vanishes southwards of the mentioned range. The amplitude of this outer high is less than the amplitude of the prominent edge-effect high as it reaches only up to 20 mGal. Following the modelling of this study, this feature appears to be related to the change from normal oceanic crust to transitional crust.

In many cases an adjacent low occurs on the slope and rise of passive margins and sometimes an additional low emerges landward of the maximum. Along the Springbok profile the wavelength of the edge-effect anomaly reaches about 100 km whereas immediately to the north the wavelength is reduced to less than 75 km. Farther north the anomaly widens again to more than 150 km. The amplitude also changes: in the north of the shown gravity map, where the Orange River drains into the ocean, a pronounced gravity signal of 60 mGal can be seen. Offshore the Olifants river mouth the same intensity is observed. Yet in general the magnitude of the signal is ~40 mGal along the margin.

Sleep and Fuyita (1997) propose a model to explain the edge-effect anomaly. This model consisted of an idealised transition between thick continental and thinner oceanic crust. However, Walcott (1972) and Watts (1988) demonstrated the importance of geologic processes and regional compensation. Watts (1988) distinguished between a rifting anomaly and a sedimentation anomaly. The first one results from the gravity response of the crystalline crust of the margin geometry through its evolution and the latter shows the influence of sedimentation on the margin. Accordingly, stretched crust produces a typical edge-effect anomaly prior to loading and is overlain by the sediment anomaly which is a high flanked by lows. Here, we explore how far the edge-effect is related to deep crustal heterogeneities.

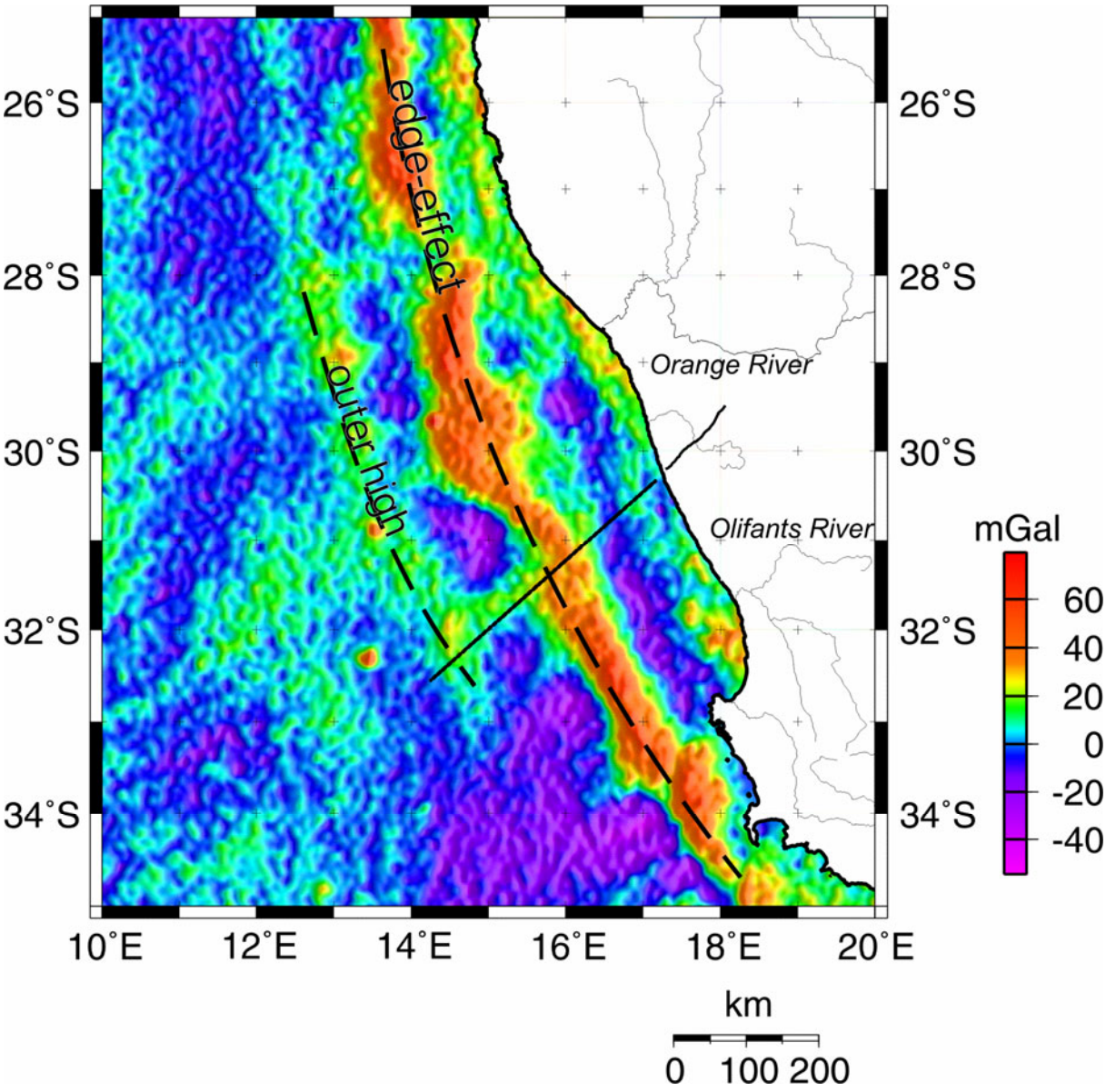

Figure 19: Marine free-air gravity field with positive "edge-effect" anomaly (Sandwell and Smith, 1997). Two dashed black lines mark the prominent edge-effect and the farther offshore a second minor feature here referred to as the "outer high". Both anomalies have also been identified along the MAMBA profile offshore Namibia (Bauer et al., 2000).

3.3.4 Gravity modelling

As stated above, the processing of the seismic refraction line Springbok revealed the velocity structure of the crust across the margin. However, as the data quality is minor in the middle shelf domain than in other domains further constraints on the crustal structure of the margin are needed. We tried to obtain further constraints by performing gravity modelling using seismic velocity results.

As a first step one gravity response of a density model derived from a velocity model was calculated. Therefore, the velocity model was converted into a density model. The respective density grid was obtained from the conversion of P-wave velocities to densities using the conversion function shown in Figure 20. This function integrates a compilation of global sample sets and is characterised by two correlations.

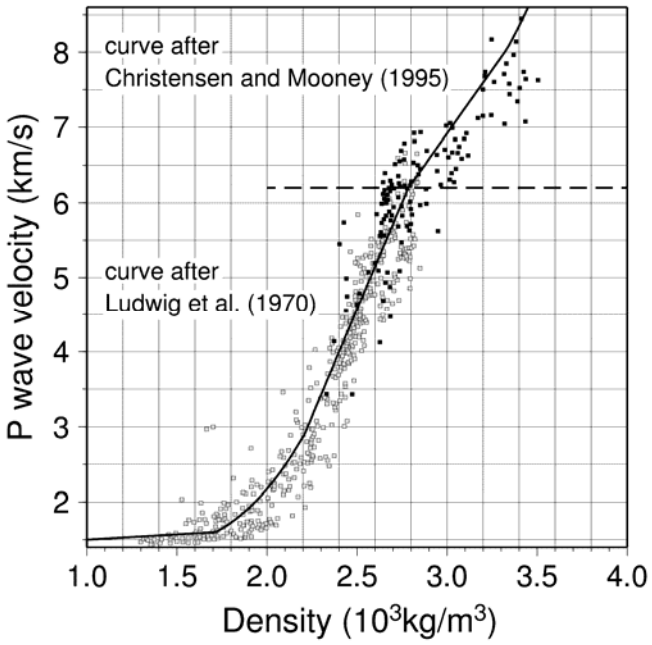

Figure 20: Conversion function used to derive densities from P-wave velocities of the final velocity model according to experimental laws (Christensen and Mooney, 1995; Ludwig et al., 1970).

The first correlation is for the P-wave velocity conversion for sedimentary rocks, the so called Nafe-Drake curve (Ludwig et al., 1970). The second correlation relates velocities and densities for igneous and metamorphic rocks (Christensen and Mooney, 1995). The calculated density grid was used to set up the first gravity model along the profile. Crustal thickness is about 33 km beneath the continent and thins towards the ocean to less than 15 km. Density contours of every 50 kg/m³ were extracted from the grid and were adopted as body boundaries in the initial gravity model. Therefore, the respective gravity model consisted of 18 bodies. The densities of these bodies range from 1600 kg/m³ in the uppermost part of the model to 3300 kg/m³ in the mantle. This density converted structure of the velocity model was included into a gravity modelling programme and the gravity response of this model was calculated. Later, the geometry of this model was altered in order to gain a fit with the observed gravity field.

Gravity modelling was carried out with the programme IGMAS, which is an interactive, graphical computer system for the interpretation of potential field data in 3D (Goetze and Lahmeyer, 1988). Geological structures are defined as polygons along parallel working planes. Between individual planes triangulations are calculated automatically.

Since the Springbok profile is just a single line and due to the lack of further information from the surrounding area, the geometry of the Springbok line was interpolated to two sections parallel to the original profile to prevent edge-effects within the modelling. The distance between the Springbok line and the adjacent profiles is 25 km. Additionally, two further sections are placed at 500 km distance for the same reason.

3.3.5 Initial gravity model

The gravity response of the initial density model which was derived from the velocity model is shown in Figure 21. In the seaward part of the profile (up to kilometre 200) a reasonable fit between the measured and calculated gravity response of the initial gravity model is achieved.

Yet a clear mass excess occurs across the middle shelf domain towards the continent resulting in an anomaly of significant width and amplitude exceeding the properties of the edge-effect anomaly in terms of amplitude and wavelength. Moreover the position of the calculated maximum gravity response is offset eastward of the observed anomaly. To achieve a better consistency between the calculated gravity response and the observations the amplitude as well as the wavelength needed to be reduced.

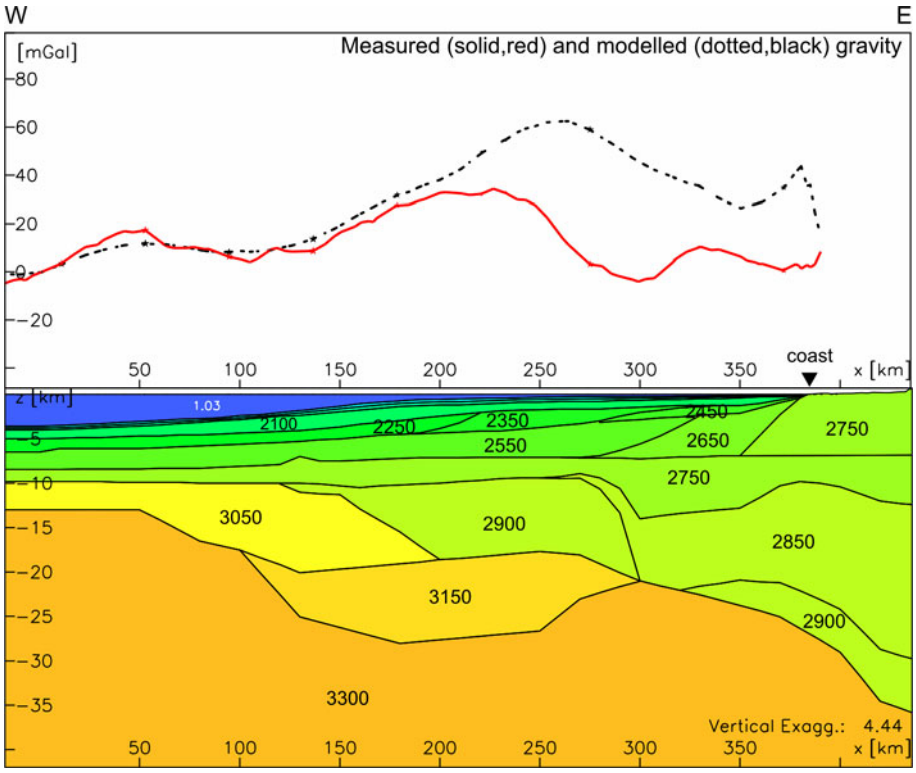

Figure 21: Calculated and observed gravity curve (upper panel) shown for the initial gravity model (lower panel). The structure of the model is derived from the converted final velocity model shown in Figure 18. The gravity response of this model implies a mass excess across the shelf break. Densities are given in kg/m³ and the reference density is 3043 kg/m³.

Even though the velocity-density-conversion allows a range of densities for the respective velocity, a fit could not be obtained alone by changing the densities along the profile. The geometry of the model needed to be altered to yield a fit with the observations (Figure 22). Several modelling attempts of changing the geometry of the crustal bodies were made, but resulted in very similar configurations to that of the final geometry of the model. These configurations involved the implementation of an additional less dense body in the upper crust (Figure 22) with a density of 2620 kg/m³. This body is not characterised by a strong velocity gradient observed in the seismic; but the velocity conversion allows a range of appropriate densities. Therefore the additional body of 2620 kg/m³ is reasonable.

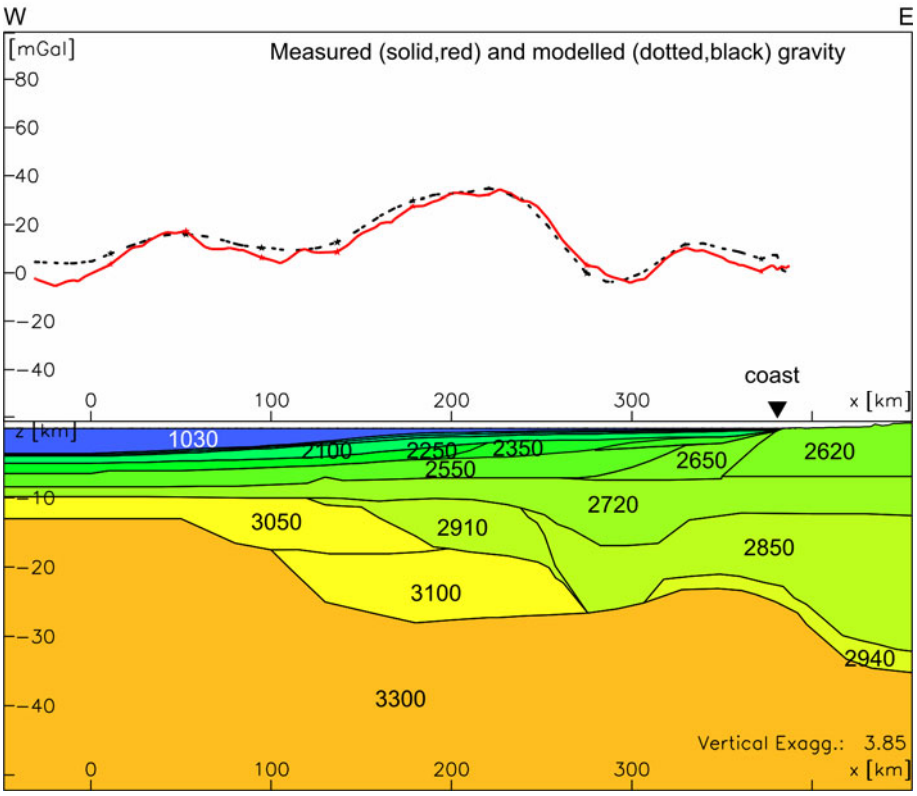

Figure 22: The upper panel shows the calculated gravity response and the observed gravity for the final gravity model. This final gravity model (lower panel) altered between km 250 and km 300 with respect to the initial density model derived from seismic velocity modelling and also the lower crustal body (ρ=3100 kg/m³) is less dense than in the initial model (ρ=3150 kg/m³). Densities are given in kg/m³ and the reference density is 3043 kg/m³.

In order to improve the fit of the model, diverse changes have been applied to it. The most significant change to the initial model was the westward shift of the transition between bodies of relatively high density towards less dense bodies in the mid-lower crust to account for the large wavelength of the calculated anomaly. In this domain the position of the Moho was deepened to reproduce the observed decrease of the amplitude. Furthermore, bodies of relative high densities (densities of 2910 and 3100 kg/m³) were reduced in dimension in comparison to less dense bodies (densities of 2720 and 2850 kg/m³) that were enlarged to diminish the amplitude (Figure 22).

There is no uniqueness in our final model configuration. It represents one solution amongst a lot of possibilities. However, we favour this final model because of it's alikeness to seismic geometries and properties.

3.3.6 Isostasy

The final gravity model which explains best the observed gravity helped us to derive the density structure of the crust and the depth to Moho across the margin. It was possible to reduce the degree of uncertainty concerning parts of the crustal structure derived from seismic data. As a next step we revised this model isostatically to analyse the present-day state of the margin.

Isostasy describes the hydrostatic equilibrium of the earth's crust/lithosphere, obeying the principles of Archimedes. The principle of local isostasy is a 1D approach that assumes all loads to be compensated locally and surrounding loads are irrelevant to the isostatic

response. Mass excesses in topography in the continental domain and mass deficiency in the oceanic domain are balanced by compensation masses. Isostasy requires the surface layers of the earth to be rigid and to "float" on, or in, a denser substratum representing the boundary between the lithosphere and the asthenosphere. Within these models the depth of compensation describes a depth, beneath of which all pressures are hydrostatic. Density compensation as required by isostasy can be accomplished in several ways: Airy (1855) compensation is achieved by depressing/deflecting the Moho as a consequence of topographic loading (ρ_{crust} and ρ_{mantle} are treated as homogeneous); isostatic equilibrium is achieved by mountains having deep roots. Loading at the surface and subsequent deflection of the asthenosphere/lithosphere boundary deflects the crust-mantle boundary (Moho). The depth of compensation is arbitrary, but deeper than the deepest mountain root.

Whilst Airy´s concept is achieving isostatic compensation by deflecting the Moho and treats the density distribution as fixed, Pratt's concept (1855) uses horizontal variations in density over a prescribed (Moho) depth. Therefore, isostatic equilibrium is achieved by a variable crustal density which is related to the elevation above sea level. In our approach, modelling is based on the comparison of a reference model to a structural model, which is in this case the structure of the Springbok profile. The reference model represents a standard crustal block floating in or on the mantle. The block has a thickness h_c and a density ρ_c. The upper edge of the block is consistent with sea level, whereupon the compensation depth specifies the depth to which the body sinks into the mantle. In other words the compensation depth describes the thickness of this standard crustal block. At the lower edge of the block equation 1 is satisfied:

$$\rho_c h_c = \rho_M h_M \tag{1}$$

Where

ρ_c = crustal density;	h_c = thickness of the crust;
ρ_M = mantle density;	h_M = thickness of displaced mantle.

It is possible to calculate the amount of displaced mantle material for a given crustal thickness and respective densities. Within the reference model the average crustal density, the mantle density and the depth of compensation is prescribed.

For the structural model equation 2 is accomplished:

$$\rho_c \cdot h_c + \rho_M \cdot h_M = \rho_W \cdot h_W + \sum \rho_S \cdot h_S + \rho_C \cdot h_C + \rho_M \cdot h_M \tag{2}$$

Where

ρ_c = crustal density;	h_c = thickness of the crust;
ρ_M = mantle density;	h_M = thickness of displaced mantle;
ρ_w = water density;	h_w = water depth;
ρ_s = sediment density;	h_s = thickness of the sediments.

Obeying Airy´s concept, the depth position of the Moho is calculated from equation 2. Based on Pratt's isostasy in turn the crustal density is achieved from equation 2 (e.g. Turcotte and Schubert, 2002, Fowler, 1996).

Isostatic modelling was done with the software **G**eological **M**odelling **S**ystem (GMS) developed at the GeoForschungsZentrum Potsdam (Scheck and Bayer, 1999). This programme allows multi 1D isostatic calculation for a 3D grid.

3.3.7 Isostatic model

The structure of the density model down to a depth of ~7 km was used as input for the isostatic modelling (Figure 23a). This boundary is defined as a density contrast between densities < 2700 kg/m³ and densities > 2700 kg/m³, which refers to a velocity increase to > 6 km/s. The position of the Moho was known from seismic and gravity modelling and used here as the lower boundary for a Pratt model. We used this model to obtain the lateral variation in average crustal density below the 6 km/s iso-velocity level. A density distribution was calculated for the mid to lower crust according to Pratt to achieve isostatic compensation over the prescribed Moho depth (Figure 23b). Several reference models had been tested. The reference model reproducing the densities derived from gravity modelling best had an average crustal density of 2965 kg/m³ and a compensation depth of 43 km.

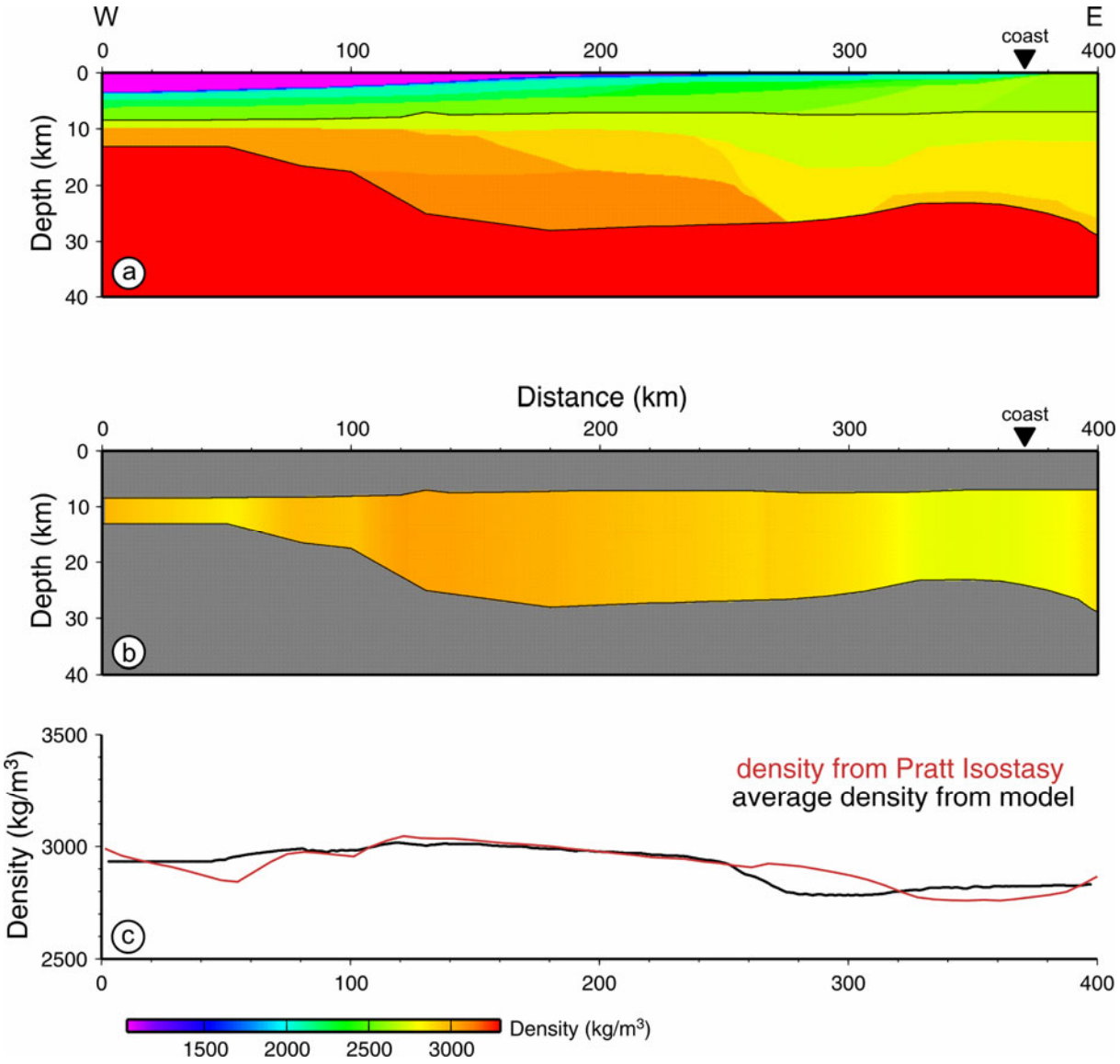

Figure 23: Isostatic modelling results. Panel **a** shows the final gravity model and the depth interval which was used in the isostatic modelling (outlined in black) to predict the average crustal density if the margin is in isostatic equilibrium. Panel **b** shows the average crustal densities derived from isostatic modelling for the respective depth interval. Panel **c** compares the average crustal densities from isostatic modelling with the average crustal densities from gravity modelling for the same depth range.

The results of the isostatic modelling are shown in Figure 23. Panel a shows the density distribution in the gravity model and the depth interval which was used for isostatic modelling outlined in black. Panel b images the calculated Pratt density distribution along the profile derived from isostatic modelling. Whereas, panel c shows the results of the isostatic modelling in comparison to the average density of the gravity model for the respective depth interval.

Isostatic modelling revealed a density range for the middle and lower crust varying between 2760 and 3050 kg/m³. In the middle of the profile (between km 80 and km 250) the densities of the Pratt model are in good agreement with the densities in the gravity model (Figure 23c). To both sides of this part the differences between both models increase and the predicted densities are higher than the ones modelled with gravity. But close to the coast the trend reverses and the isostatically predicted densities are lower than seen in the gravity model.

3.4 Discussion

3.4.1 Crustal structure at Springbok and along the margin

The velocity distribution obtained by 2D velocity modelling allows the following interpretation of the margin (Figure 24): On top of the section velocity modelling revealed a sedimentary succession of considerable thickness of about 4-5 km which diminishes towards the continent until the thickness is reduced to a few hundred metres landward of the shelf break and finally vanishes onshore.

Between km 0 and km 50 velocity contrasts within the crust separate oceanic layers 2A and 2B. Layer 2A is commonly interpreted as extrusive flows of pillow basalts with velocities of 4.5-5.0 km/s and layer 2B as basaltic sheeted dikes with velocities of 6.2 km/s. Beneath of which the velocities increase to 7 km/s which indicates the gabbroic layer 3. This layer is in turn underlain by a layer of cumulates, rocks formed from mafic minerals in a cooling magma (e.g. Spudich and Orcutt, 1980; Pluijm and Marshak, 2004; Raum et al., 2006).

Transitional crust has been identified from km 50 to km 250 along the profile where the middle and lower crust is characterised by high P-wave velocities (6.9 – 7.4 km/s) as most commonly observed at rifted volcanic margins.

Heavily intruded continental crust or mafic intrusions/underplating are commonly interpreted to cause these high velocities in the respective depth range but from seismic resolution alone it is not possible to distinguish between both. It is very likely that the interpreted transitional upper crust is a mixture of both and includes extended and rifted old continental segments. On top of this section, seaward dipping reflectors are observed in MCS which are interpreted to represent volcanic flows and sediments (Talwani and Abreu, 2000, Schnabel et al., 2006) most likely emplaced during continental break-up and early seafloor spreading (e.g. Eldholm et al., 1995). Thirdly, from km 250-300 to km 500 velocities range from 5.9 to 6.1 km/s at surface and thus indicate continental crust. Here, the crust is characterised by a continuous velocity increase with depth, but no significant velocity contrasts were found to divide the crust into an upper and a lower continental crust. Within the continental crust small scale zones of high velocities are spatially linked with the location of the Gariep Mobile Belt. The latter could either represent minor intrusions related to the continental break-up or relicts of high grade metamorphic rocks formed during the Damara Orogeny.

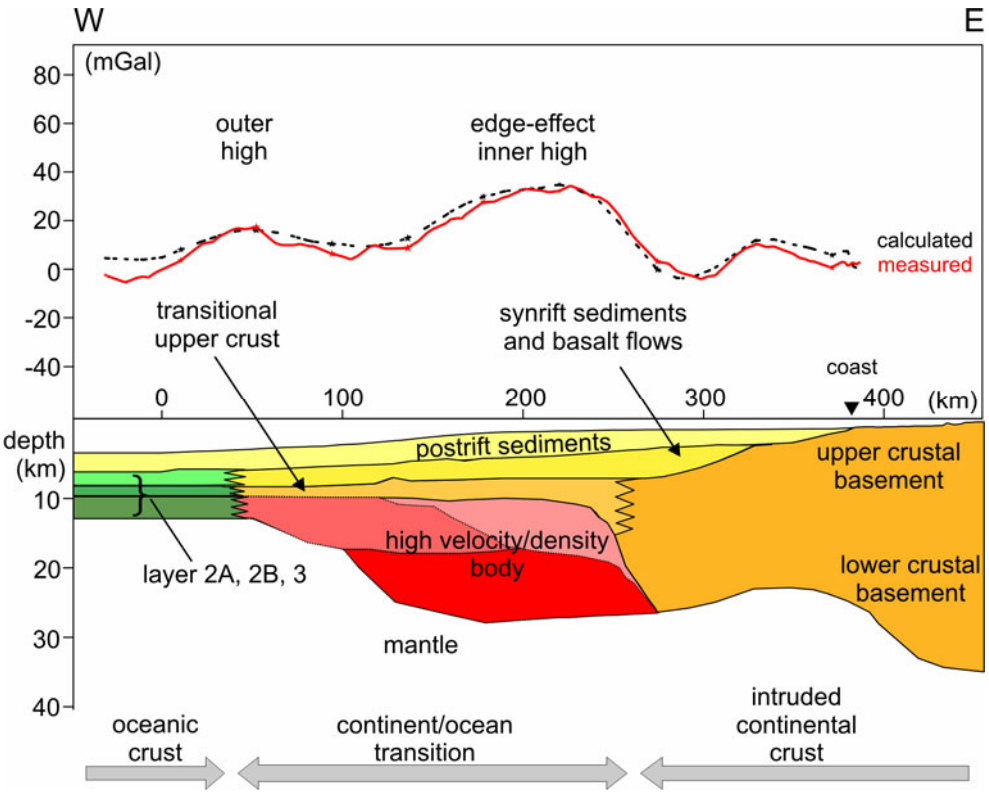

Figure 24: Interpretation figure of the Springbok line. In the oceanic domain, oceanic layers 2A, 2B and 3 could be resolved between km 0 and km 50. Layer 2A changes gradually into a layer interpreted to contain syn-rift sediments and basaltic flows eastward of km 50. Here the transitional crust in underlain by a high-velocity, high-density body in the lower crust. These two domains are overlain by sedimentary successions that diminish towards the coast. From km 250 towards the east the crust is continental in origin and no sedimentary cover is observed.

In comparison to this fairly small scale local features, lower crustal bodies of high seismic velocities and also high densities of considerably extension as observed along the Springbok line have been documented on several other volcanic margins, although their origin remains controversial. Talwani and Abreu (2000) demonstrated the presence of such bodies characterised by high seismic velocities (7.2-7.4 km/s) both in the North Atlantic offshore of the eastern United States and in the South Atlantic offshore Brazil and Namibia. These bodies reach up to 24 km in thickness and are interpreted to originate from accretion processes of igneous material during the break-up (Holbrook et al., 1994). Furthermore, these high-velocity bodies correlate spatially with break-up features as defined by Eldholm et al. (1995) including onshore continental flood basalts, extrusive basaltic complexes along the continent-ocean transition, and the occurrence of seaward dipping reflector wedges.

To explain the evolution of passive margins one can not ignore the very first, but elegant theory of basin evolution by McKenzie (1978). He developed that included the thinning of the lithosphere accompanied by asthenospheric upwelling to maintain the isostatic equilibrium. Later, authors elaborated on McKenzie´s model by proposing a passive upwelling of the asthenosphere to result in melt generation (Foucher et al., 1982). White and McKenzie (1989) developed the discussion further by suggesting that decompressional melting just occurs if a mantle plume causes a thermal anomaly to create large quantities of melts.

On the other hand, numerical simulations showed an alternative of mechanical processes generating melt volumes (Gernigon et al., 2004). Due to crustal thinning mantle material rises and consequently decompressional melting processes in the head of the rising material cause significant volumes of melt (Van Wijk et al., 2001). In these models the volume of melt is controlled by the thinning factor beta.

The volcanic character of the South Atlantic margin south of the Walvis Ridge-Rio Grande Rise appears to be independent from plume influence, an interpretation also suggested by the presence of a wedge of seaward dipping reflectors. This wedge occurs along the entire margin south of the Walvis Ridge and is constant in width and volume (Talwani and Abreu, 2000). North of the hotspot traces of the Walvis Ridge and the Rio Grande Rise these seaward dipping reflectors vanish and continental flood basalts are not observed. The Walvis Ridge separates the southern part of the margin which is volcanic in nature from the northern part where the margin appears to be non-volcanic in character (e.g. Gladczenko et al., 1998).

The involvement of a mantle plume is not a prerequisite to produce melts but increases the generated melt volumes and influences the melt composition. In the plume vicinity melts are rich in magnesium due to increased mantle temperatures which results in increased seismic velocities compared to velocities of rocks originating from melts generated distal to a plume head (White and McKenzie, 1989, Holbrook and Kelemen, 1993). Studies undertaken by Trumbull et al. (2000, 2002) argue for the influence of a mantle plume as far south as offshore Namibia. Farther south they propose a diminishing influence of the Tristan da Cunha plume based on decreasing magnesium composition in the crust.

North of our studied profile the MAMBA experiments offshore Namibia (Bauer et al., 2000) aimed to reveal the crustal structure of the margin with a combined approach of seismic interpretation and gravity modelling. In particular, these results indicate the presence of lower crustal bodies characterised by P-wave velocities >7 km/s and densities >3000 kg/m^3. According to these data, the gravity observations are explained by a superposition of topographic effects and lateral density variations, but, like along the Springbok profile lower crustal bodies of high densities are required in addition.

Comparing the results of the three seismic refraction experiments it becomes clear that the thickness and the average velocities of the lower crustal body decrease from north to south (Figure 25).

Accordingly, the 3D nature of this high-velocity body is not debatable. It is characterised by a southwards decreasing thickness but also a slight decrease in maximum velocities. The MAMBA profiles reveal a high-velocity body with a thickness of ~20 km and with velocities of up to 7.6 km/s. Along the Springbok transect our seismic velocity modelling results reveal a P-wave velocity of 7.4 km/s and a maximum thickness of 10 km for this body. This confirms the tendency that the dimension of the high-velocity body diminishes from north to south. These observations appear to support the suggestions of Trumbull et al. (2007), who argue for reduced magnesium content in the produced melts from north to south. Furthermore, this aligns with the theory of less melt production distal to mantle plumes.

A further seismic refraction/reflection line (Profile 95303) offshore the Orange River mouth identified a similar crustal structure across the margin, including a high-velocity body (7.1-7.4 km/s) in the lower crust (Schinkel, 2006). Gravity modelling suggests that this body has a density of 3130 kg/m^3 and a maximum thickness of about 13 km. In this study, the interpretation of mafic intrusions in the lower crust have been emplaced in late rift stages is favoured to explain the presence of the lower crustal body.

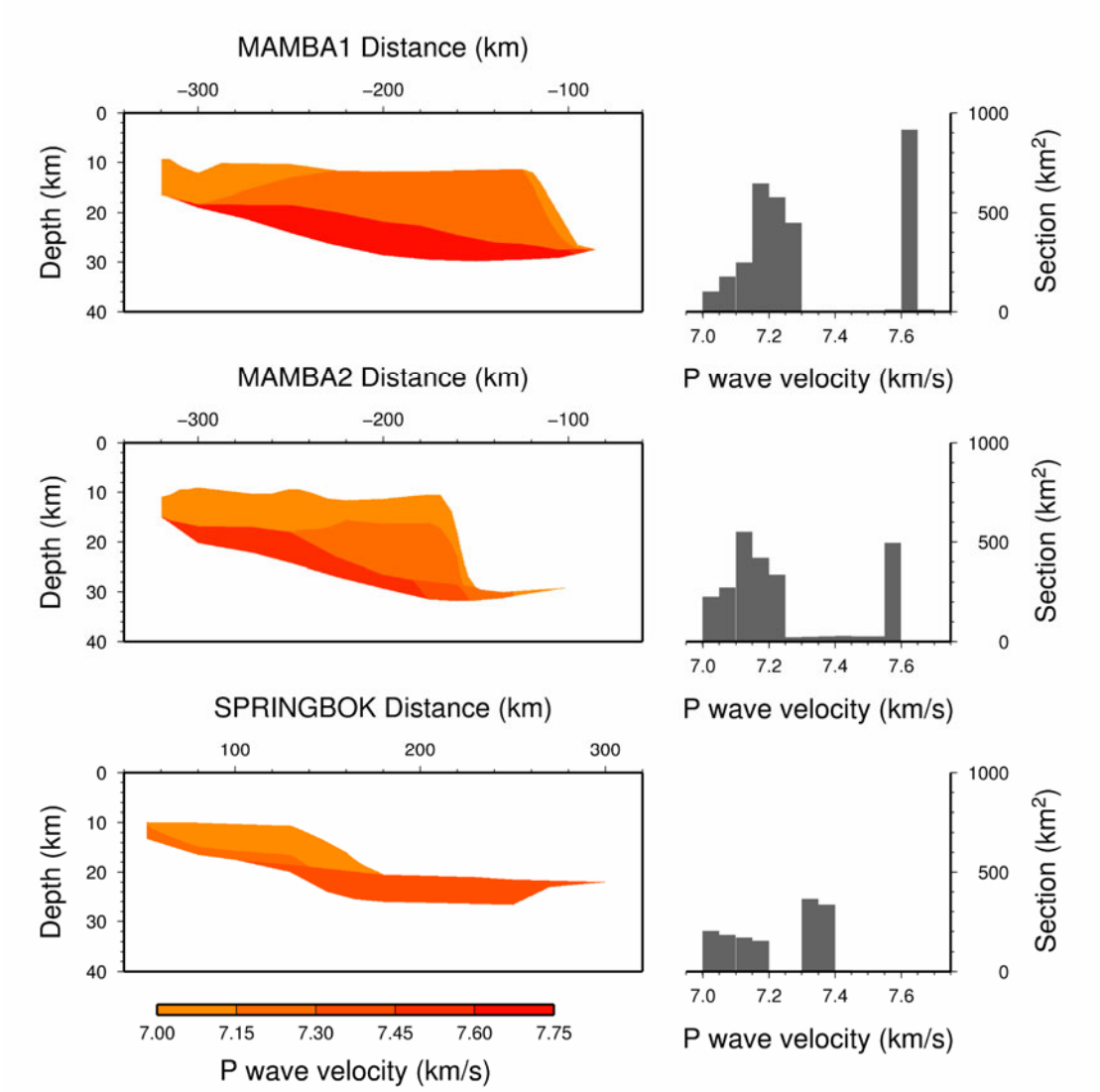

Figure 25: Model of the high-velocity bodies (v > 7km/s) interpreted for three seismic refraction lines recorded across the West African margin (for location see Figure 13b) and the respective velocity distribution. The comparison shows the southward diminishing extent of this high-velocity bodies and the decrease in P-wave velocities from north to south.

3.4.2 Gravity anomalies along the margin

The final density model reproduces the observed edge-effect anomaly. The maximum of the calculated gravity anomaly is located above the shelf break which coincides with the position of a lateral density gradient from dense to less dense material in the lower crust. This density contrast in the lower crust is crucial to reproduce the observed edge-effect anomaly. In comparison to the initial velocity model this gradient had to be dislocated seaward and amplified. The areas of high densities still correlate spatially with zones of high velocities and reach a maximum thickness of 10 km. Isostatic modelling also confirms high densities within this domain of the margin.

Thus in summary, the edge-effect anomaly is a superposition of two components. Firstly, a sediment pile on top of the model produces a rise of the observed gravity curve. This, however, does not reproduce the observed gravity pattern. So secondly, a high-density body

in the lower crust is required to produce a density contrast which in turn causes the anomaly to decline continentward and follow the observed curve.

Offshore Namibia Stewart et al. (2000) modelled the gravity low on the shelf landward of the gravity high with a sediment filled graben structure. Due to the fact that no considerable sediment-filled graben structure is observed in MCS, we argue for the density gradient in the lower crust to force the amplitude to decline.

An earlier gravity study offshore Namibia (Light et al., 1992) was performed to image the deep crustal structure that infers the presence of an anomalous high-density body in the lower crust which was interpreted as a continuous mantle wedge. In contrast to this interpretation, our findings suggest P-wave velocities and densities higher than expected for normal crust but lower than for mantle properties. In addition, the spatial distribution of the properties constrains the geometry of the high-velocity body and excludes a mantle wedge.

Furthermore, in the southern Orange Basin 3D gravity modelling revealed a similar crustal structure as derived from the Springbok profile and indicates the presence of a high-density body in the lower crust which is about 11 km thick in average, and has a density of 3200 kg/m³ (Hirsch et al., 2007). There it was shown that the gravity signal caused by the sedimentary wedge on top of the model and the lower crustal bodies act in concert to reproduce the observed edge-effect anomaly.

3.4.3 Consideration of isostasy

The results of isostatic modelling imply isostatic equilibrium for the high-density body in the lower crust over large parts. This is concluded from the consistence between the lower crustal densities obtained by isostatic and by gravity modelling. Deviations from isostasy are less than 50 km wide and are probably compensated regionally.

A series of reference models have been tested for the isostatic modelling. The fit between the isostatically obtained densities and the average density of the gravity model could also be achieved using different reference models. A reduction of the compensation depth in combination with a reduced average crustal density results in the same density distribution as if a reference model with a deeper compensation depth was used in combination with higher average crustal density. For a minimum compensation depth of 40 km the respective reference density is 2900 kg/m³. This value represents a reasonable average of continental and oceanic crustal density. A shallower compensation depth is impossible due to the thickness of the unstretched continental crust. To increase the compensation depth to 45 km demands a crustal reference density of 2980 kg/m³ which is a rather high value for average density between oceanic and continental crust. Nevertheless, all these tests provide reasonable density variations for the continental crust ranging from 2800 to 3000 kg/m³. Thus we conclude that the system is isostatically balanced at the depth level of 40-45 km and at least at 45 km depth all pressures are hydrostatic.

The gravity modelling of the initial model configuration revealed a mass excess in the range from km 200 to km 350 which does not reproduce the observations. To obtain a better fit this mass excess was reduced in wavelength and amplitude. In contrast, local isostatic modelling predicted higher densities than derived by gravity modelling in the 260-300 km segment of the profile. These higher densities in the crust predicted by local isostasy are contradictory to the results of the gravity modelling. Obviously the respective segment of the profile is less dense than isostatically required and indicates an isostatic disturbance at this location. Here the load is not equilibrated locally, but appears to be sustained by the regional

rigidity of the lithosphere. It is very likely that crustal blocks are not completely compensated in terms of local isostasy. The principle of Pratt's isostasy assumes all loads to be compensated locally which is equivalent to the assumption of no elastic strength in the lithosphere (Roberts et al., 1998). This assumption is of course not correct and may lead to overestimates of the average crustal density in the calculations because loads are distributed regionally.

In contrast to our results, farther south isostatic models suggest that the margin there is rather far from isostatic equilibrium (Hirsch et al., 2007). Isostatic and gravity analysis based on a 3D structural model of the Orange Basin revealed a large discrepancy between crustal configurations predicted by local isostasy and 3D gravity modelling. There, however, deep seismic constraints are missing.

3.5 Conclusions

Three types of models have been used to derive a comprehensive picture of the crustal structure of the South African passive continental margin. This conjunction of different approaches reduced the ambiguousness in both, the seismic velocity modelling and also the modelling of potential field data which alone always leads to non unique results. To top the modelling off, isostatic modelling was applied to reveal the isostatic state of the margin.

From seismic modelling we identified three types of crustal structure along the transect. In the western domain of the profile, typical oceanic layered crust (where layer 2A, 2B and 3 are distinguished) is followed eastward by a transitional crust in the middle domain of the profile. Here typical volcanic margin features were found encompassing seaward dipping reflectors in the MCS data and a high-velocity, high-density body in the lower crust revealed by 2D seismic velocity modelling. Finally, continental crust was identified at the landward termination of the profile where P-wave velocities imply the lack of a considerable sediment cover but indicate the presence of a metasedimentary succession. In the middle and lower continental crust some local anomalies of high velocity and density suggest minor, break-up related features.

The density structure of the margin was approved by gravity modelling which required a slight westward shift of the boundary between the transitional and the continental crust in comparison to the initial density model which was yielded from the velocity model using two conversion laws to account for the mass excess of the initial density model. Accordingly, the high-velocity body in the lower crust was modelled with a density of 3100 kg/m³.

Isostatic modelling indicates that isostatic equilibrium is established over large parts of the profile. The best-fit and most reasonable isostatic model includes an average reference crustal density of 2965 kg/m³ in combination with a compensation depth of 43 km. We found that all masses are balanced and pressures are hydrostatic at least below a depth of 45 km.

Acknowledgements

This work has been done in the framework of INKABA yeAFRICA at the GeoForschungsZentrum Potsdam.

We wish to thank Dieter Franke, Sönke Neben and Michael Schnabel from the BGR and in addition Trond Ryberg, Albrecht Schulze and Michael Weber from the GeoForschungsZentrum Potsdam for preparation and execution of the Springbok experiment. Geophysical Instrument Pool Potsdam (GIPP) provided the instruments for the

onshore part of the experiment. Thanks go also to the field crews on- and offshore for their work during the measurements and in particular to Coenie de Beer for the preparation of the experiments. J. Mahayele is acknowledged for his work in the first phase of data analysis. Special thanks go to J. Stankiewicz for his help to generate the geological map.

Isostatic modelling was performed with the Geological Modelling System (GMS) developed at the GeoForschungsZentrum Potsdam, Department Organic Geochemistry under the leadership of Prof. Dr. U. Bayer.

We thank H.-J. Götze and S. Schmidt, University of Kiel, for the 3D gravity modelling programme IGMAS.

4 Tectonic subsidence history and thermal evolution of the Orange Basin

Abstract

The Orange Basin offshore southwest Africa appears to represent a classical example of continental rifting and break-up associated with large-scale, transient volcanism. The presence of lower crustal bodies of high seismic velocities indicates that large volumes of igneous crust formed as a consequence of lithospheric extension.

We present results of a combined approach using subsidence analysis and basin history inversion models. Our results show that a classical uniform stretching model does not account for the observed tectonic subsidence. Moreover, we find that the thermal and subsidence implications of underplating need to be considered. Another departure from the uniform stretching model is renewed sub-crustal stretching and linked to that uplift in the Cenozoic that is necessary to reproduce the observed phases of erosion and the present-day depth of the basin. The dimension of these events has been examined and quantified in terms of tectonic uplift and sub-crustal stretching. Based on these forward models we predict the heat flow evolution not only for the available real wells but also for virtual wells over the entire study area. Finally, the hydrocarbon potential and the temperature evolution is presented and shown in combination with inferred maturation of the sediments for depth intervals which comprise potential source rocks.

4.1 Introduction

Basins located in a passive margin setting are commonly regarded as quiescent after the transition from rift to drift stage and during the following subsidence. Nevertheless, most of these basins may undergo strata disruption to some degree caused by processes such as salt mobilisation, post break-up flank uplift or margin instability. The Orange Basin offshore western South Africa (Figure 26) is one of the few examples where these margin deformation mechanisms were not active or dormant throughout most of the basin history. Since the basin contains the stratigraphic record from lithospheric extension and rift tectonics to a fully evolved post-break-up setting it provides an ideal area to study the evolution of a “passive” continental margin. With this study we aim to analyse the tectonic history of the Orange Basin.

Though several campaigns have been carried out, with a resultant established seismic and stratigraphic framework for the Orange Basin (e.g. Brown et al., 1995), many aspects and main questions of basin formation and margin evolution remain unexplored. In particular, processes in the underlying mantle and mechanisms for suspected phases of uplift and denudation along the margin are poorly understood.

Here, we develop a tectonic model that explains both the observed subsidence history as well as phases of uplift and erosion while incorporating the observed crustal configuration.

A combined approach of reverse and forward modelling has been applied in the course of which several model configurations have been tested. Classical approaches obeying the principles of uniform stretching (McKenzie, 1978) have been applied and have been further expanded for departures as the effects of underplating and renewed stretching in the mantle. Thermal implications of these departures have been analysed and the respective temperature evolution has been cross-checked with observed vitrinite reflectance data.

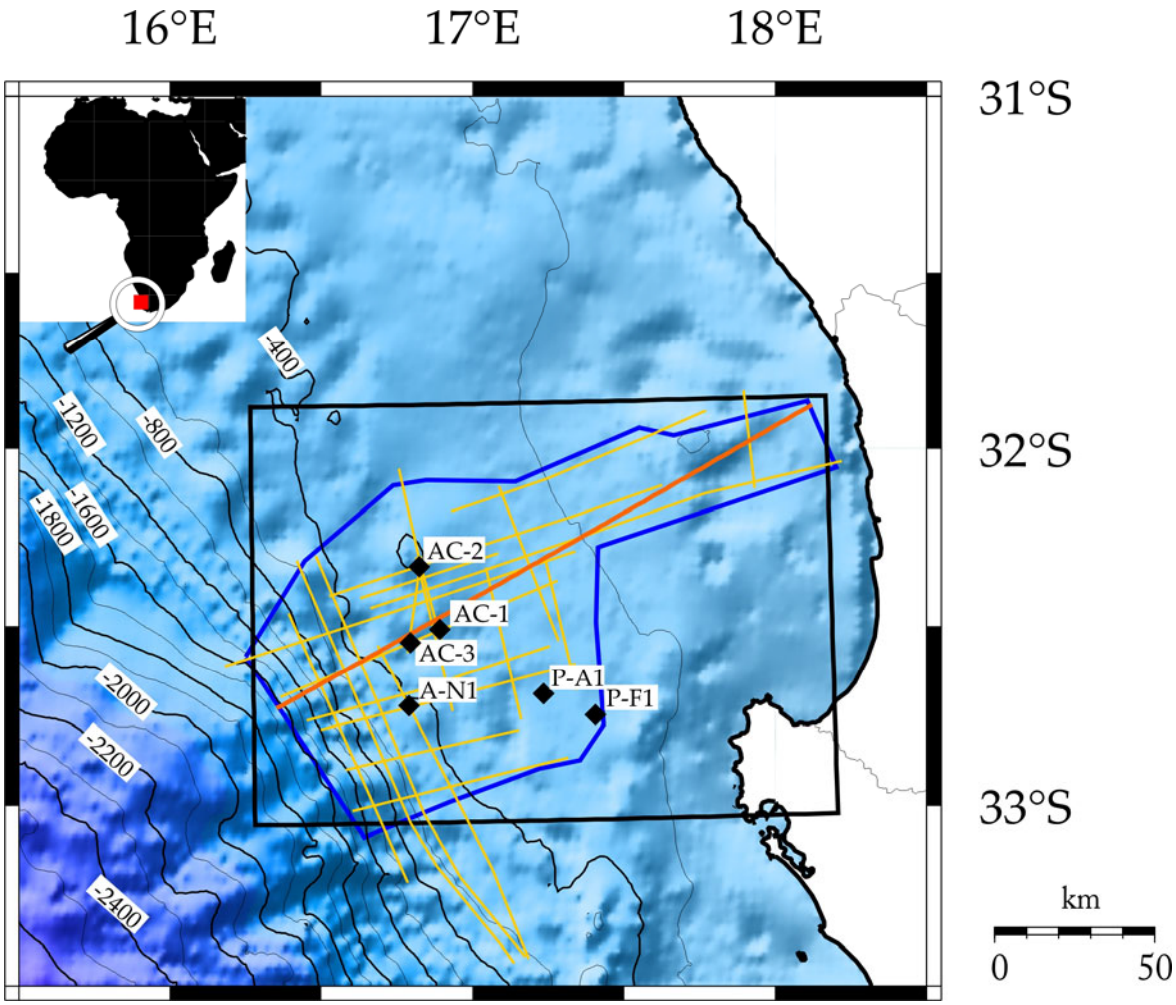

Figure 26: Bathymetric map of the working area offshore west South Africa. The black line outlines the area covered by the 3D model presented in this study, overlain by yellow lines indicating the position of available seismic lines which are embraced by a blue line marking the area of best data coverage. Black diamonds represent the analysed wells. The orange line documents the position of the cross-section shown in Figure 28.

4.1.1 Database

The database for this study comprises 2D seismic reflection profiles of 6 s TWT recording time and of 2000 km length in total (Figure 26). Tied to these profiles 7 wells have been investigated that are located on the continental shelf in varying water depths ranging from 240 m to 750 m (Figure 27). Wells placed along seismic profiles allowed us to attribute sedimentary lithologies to the interpreted seismic horizons. Age constraints for the interpreted seismic horizons have been provided by the Petroleum Agency South Africa in the form of biostratigraphic picks for the drilled successions. Well data also included gamma-ray wire-line logs, lithologies, vitrinite reflectance, and biostratigraphy.

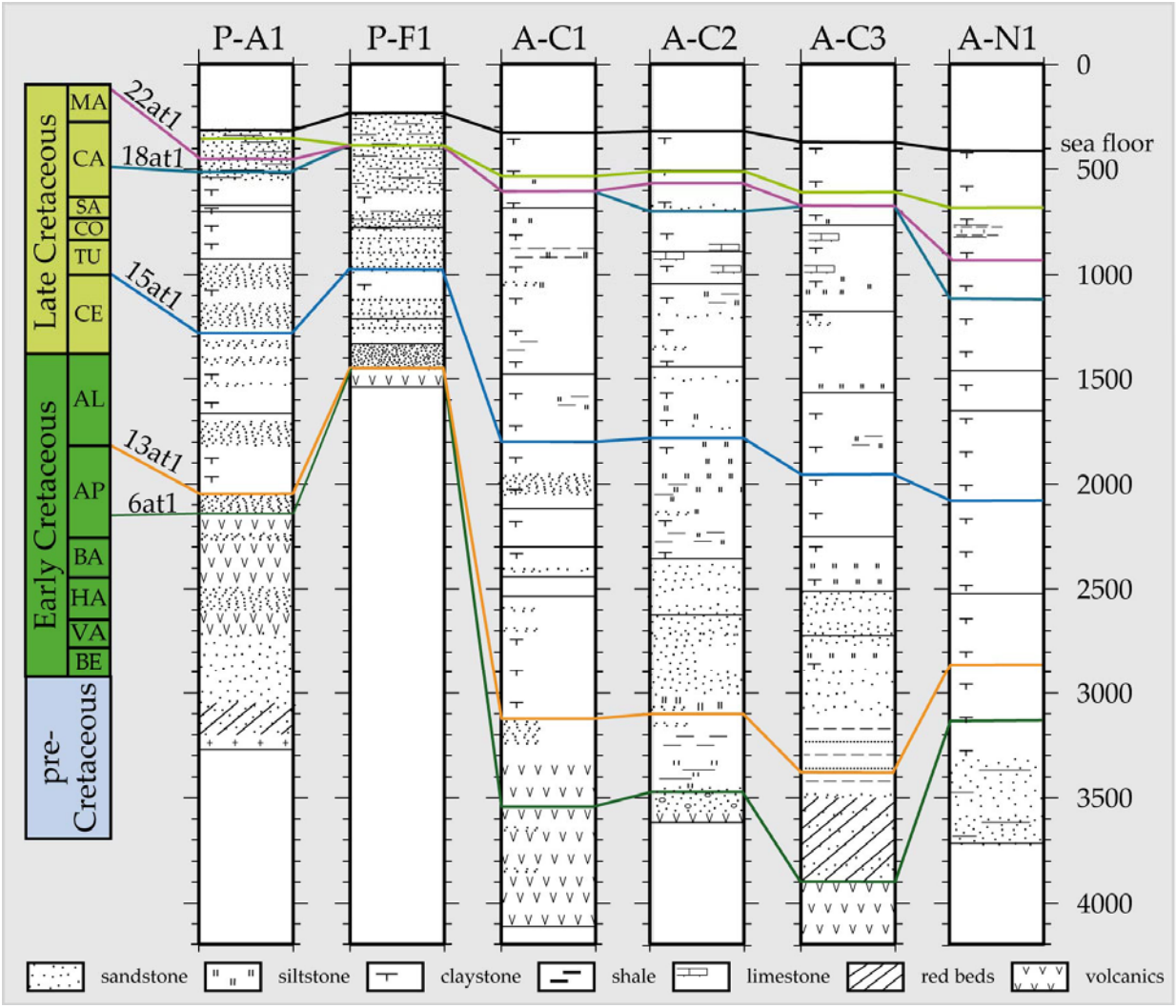

Figure 27: Age correlation of seismic stratigraphic horizons between the individuals wells with the according lithologies.

These data provided the base for a seismic stratigraphic investigation by Paton et al. (2008) for which a local seismic stratigraphic nomenclature was used devoted solely to the Orange Basin and developed at SOEKOR in the 1990´s (McMillan, 2003). This interpretation of seismic lines provided by Paton et al. (2008) was further used by Hirsch et al. (2007) to create a 3D model of the basin infill and the underlying lithospheric structure. The crustal configuration for this model was derived using information from deep seismic sounding for 3D gravity modelling. This study yielded the presence of a high density, lower crustal body with a stark density contrast compared to a less dense lower crust continentward, the geometry of which is used to assess the influence of underplating in this study (Figure 28).

In summary, we use detailed well information and the previously developed 3D model. The latter not only includes information on the configuration of the sediments but also accounts for the lithologies, porosities and densities of the different layers as well as thermal such as radioactive heat production and conductivities.

An additional source of information was a set of vitrinite reflectance data, a widely used indicator for the maturity of organic matter (e.g. Héroux et al., 1979; Allen and Allen, 2006). Vitrinite reflectance increases with increasing burial and temperature, and represents a good measure of the peak paleo temperature to which the sample has been subjected to in its

history (Dow, 1977). Lateral and vertical trends in vitrinite reflectance result from a range of basin-scale geological processes. They can offer important constraints with respect to the thermal evolution and the exhumation history and give insights into mechanism of heating and cooling of the rocks (Cocoran and Clayton, 2001).

Since thermal reactions are irreversible, vitrinite reflectance data are a reliable thermal calibration method which can be also used to assess and quantify the denudation (e.g. Dow, 1977; Allen and Allen, 2006). Especially in exhumed basin settings vitrinite reflectance data are of particular importance. Here a quantitative assessment of the peak paleo temperatures achieved by potential source rock intervals is decisive for the maturation of the organic matter (Cocoran and Clayton, 2001). Several drawbacks such as the reworking of organic material, identification of primary vitrinite material, rough texture or inclusions should be taken into account but for a depth interval of 1-4 km vitrinite reflectance is a good measure of the maximum paleo temperature and for the evaluation of the thermal alteration of sedimentary rocks (Héroux et al., 1979).

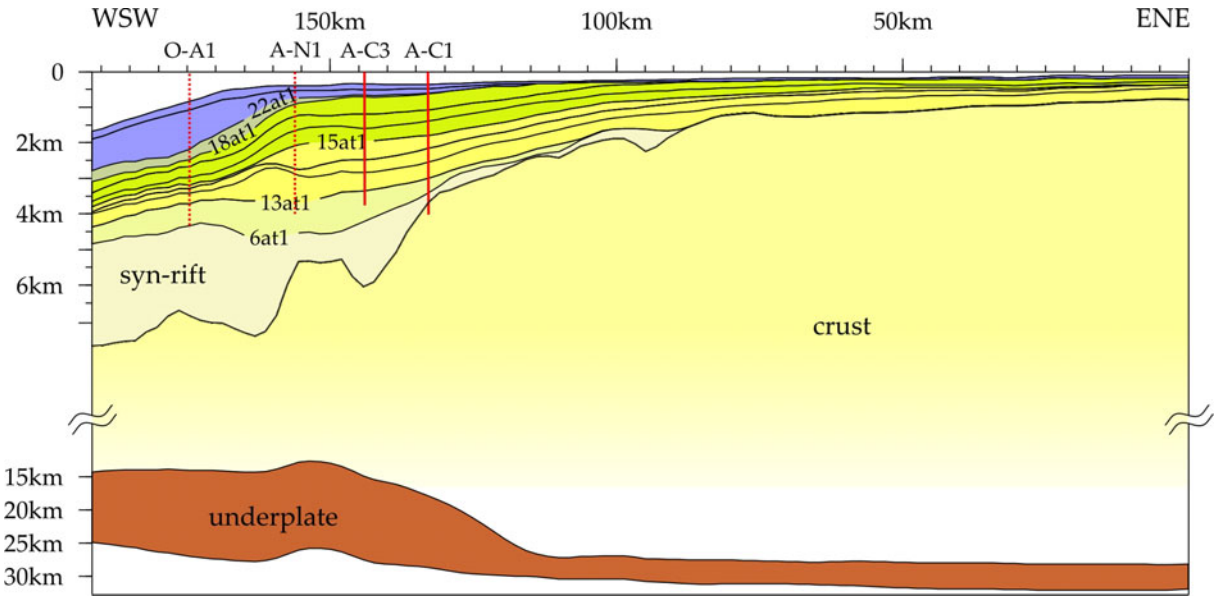

Figure 28: WSW-ENE oriented cross-section through the 3D model (for position see Figure 26) illustrating the main features of the margin comprising sequence stratigraphic boundaries as well as main crustal structures like the underplated body. Additionally, the positions of the wells are plotted along the transect (dashed lines indicate projected wells).

4.2 The Basin

rifting

The Orange Basin is situated on the continental margin of South Africa and southern Namibia (Figure 26) and it represents by far the largest depocentre in the Atlantic around South Africa. Basin initiation was part of the rifting between South-America and Africa that resulted in the break-up of the South-Atlantic in Early Cretaceous times.

Studies along the South African continental margin indicate that the rifting history was complex (Gladczenko et al., 1997; Gladczenko et al., 1998; Bauer et al., 2000; Stewart et al., 2000). It is, however, evident that the continental break-up of Africa and South America was accompanied by massive, transient volcanic activity evidenced by the widespread occurrence of volcanic rocks. Coevally to rifting, the South Atlantic Large Igneous Province was emplaced, which encompasses the Paraná–Etendeka continental flood basalts. Offshore,

a wedge of seaward dipping reflectors is interpreted to represent the offshore counter part of extrusive complexes (Hinz, 1981; Gladczenko et al., 1997; Talwani and Abreu, 2000; Bauer et al., 2000; Hirsch et al., 2007).

The analysis of volcanic rocks onshore South Africa and Namibia is supposed to give age constraints on the age of rift initiation as these rocks were emplaced due to the prevailing magmatism at the time of initial extension. In Namibia K-Ar and Ar-Ar dating of coastal dykes swarms provides an age of ~134 Ma (Seider and Mitchell, 1976). Farther south in the False Bay, dykes were K-Ar dated to 132 ± 6 Ma (Reid et al., 1991) and in the lower Orange River region Ar-Ar dating of the Mehlberg dyke gave 134 ± 4 Ma (Reid and Rex, 1994).

Offshore Namibia and also farther south, offshore South Africa, deep seismic profiles revealed the presence of a high velocity body in the lower crust which is interpreted to represent the intrusive counterpart of the seaward dipping reflector wedge found in the distal parts of the Orange Basin. Because of its seismic properties and modelled densities this body is interpreted as an underplated mafic wedge (Figure 28; Hirsch et al., in press; Bauer et al., 2000).

syn-rift

Rifting was accompanied by initial faulting and the creation of half-grabens aligned roughly parallel to the present coastline (Gerrard and Smith, 1982). The syn-rift graben infills consist predominantly of fluvial claystones, sandstones, and pebble beds (McMillan, 2003) which are assumed to have been deposited coeval to the injection of coastal dykes around 132 or 134 Ma (Reid and Rex, 1994). The fluvial, coarse clastic nature of the syn-rift deposits indicates that deposition started in a mostly continental environment.

The graben infills are unconformably overlain by a transitional Early-Cretaceous succession of lacustrine sediments and volcanic rocks (Figure 29; Muntingh and Brown, 1993) comprising a deepening-upward sequence of fluvial red beds and sand-prone deltaic deposits pointing to an increasing water depth until 112 Ma (Paton et al., 2008). These sediments embrace the proven Hauterivian source rock which is the eldest of the three source rock intervals in the Orange Basin. The top of this succession is a well-defined late Hauterivian unconformity (6at1, 117.5 Ma) indicating the transition to a marine depositional environment (Brown et al., 1995).

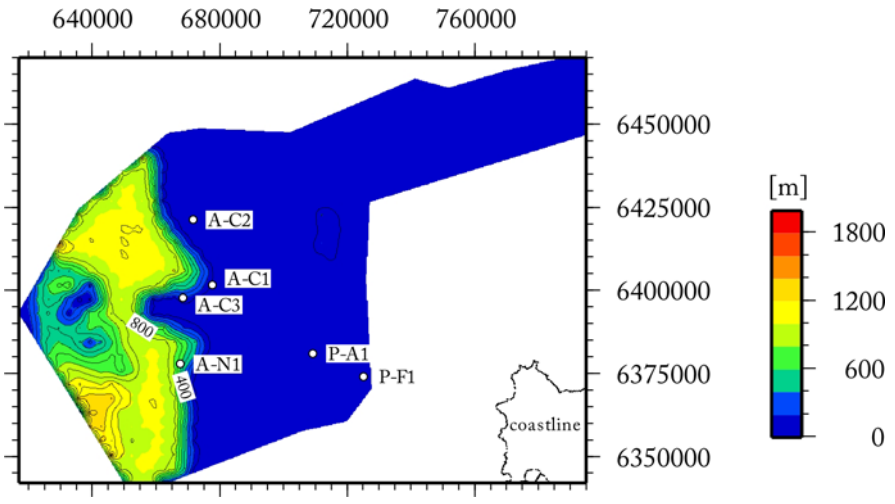

Figure 29: Thickness map of the syn-rift succession derived from seismic interpretation.

post-rift

Along the southwestern margin of the African plate drift commenced at ~117.5 Ma and the Hauterivian unconformity (6at1) marks the transition from rift to drift-stage (Gerrard and Smith, 1982; Muntingh and Brown, 1993). On top of the drift unconformity, the deposition was characterised by continental and shallow marine sediments with occasionally interbedded basaltic rocks. Areally restricted, red beds are deposited which, in turn, are followed upwards by coarsening-upward, sand-prone deltaic deposits. Microfossil assemblages of early drift sequences demonstrate that marine conditions have prevailed since Mid-Barremian times only in the distal part of the Orange Basin (Muntingh and Brown, 1993; McMillan, 2003) where water depth even exceeded the present-day water depth.

The Hauterivian unconformity (6at1, 117.5 Ma) and the Aptian unconformity (13at1, 112 Ma) embrace a sediment package that has been deposited predominantly on the outer and middle margin. It is rarely affected by faulting (Gerrard and Smith, 1982). The thickness of this unit points to an elongated depocentre with a NNW-SSE trending axis, where a maximum of 1500 m of sediments is preserved (Figure 30a). The lithology of this interval appears to vary significantly from north to south. North of the working area drilling penetrated mainly marine shales resting on gas-bearing sandstones intercalated by basaltic lavas (Gerrard and Smith, 1982). To the contrary, the wells A-C1 and A-C2 encountered mainly sandstones and minor conglomerates of shallow marine origin. Closer inshore wells intersected continental red beds with minor amounts of lavas or igneous intrusions (Gerrard and Smith, 1982). The thickness of the succession between Early Barremian to Late Campanian times indicates that sedimentation was predominantly siliclastic since the Orange Basin received the majority of the drainage of Southern Africa (Muntingh and Brown, 1993; McMillan, 2003). Frequently rapid rates of sediment input and subsidence provide a preserved succession of fluvial/coastal deposits in the proximal domain of the margin. The basin expanded shoreward when the Barremian to middle Albian successions progressively overstepped the underlying sequences in an eastward direction.

From the Aptian interval (13at1) until the Cenomanian/Turonian interval (15at1) sedimentation was concentrated on the middle shelf domain where a paleo shelf break of up to 2000 m developed. At the same time sedimentation was reduced on the inner shelf (Figure 30b). The thickest portions were deposited from Early Albian to Early Cenomanian times when sedimentation was in general more clay-rich than before and included coarsening-upward silts to medium sandstones. Massive sandstones developed locally across the paleo outer shelf.

The margin of the basin migrated offshore slowly to the west which suggests subtle differences in the tectonic regimes of the Atlantic (McMillan, 2000; Paton et al., 2008). On the outer margin, the lowermost part of the package comprises the anoxic black shales of Barremian and Aptian age which represent the region's best source rocks (Herbin et al., 1987; Paton et al., 2008). Paleontological data document a decreasing water depth which remained shallower than today at all times since Early Aptian times (McMillan, 2003).

A north-westward shift of the depocentre is indicated by the cumulative thickness of the Cenomanian/Turonian (15at1) to Campanian (18at1, 75 Ma) successions. Across the inner and middle margin sedimentation deposited packages of moderately uniform thicknesses. The lithologies are fluvial sands and occasional grits, interbedded with shales and occasional silt stringers in varying proportions. In the area of the A-Wells thicknesses of 900 – 1500 m are preserved today (Figure 30c). Within these successions is the most speculative source rock interval of Cenomanian to Turonian age (Van der Spuy et al., 2003; Paton et al., 2008).

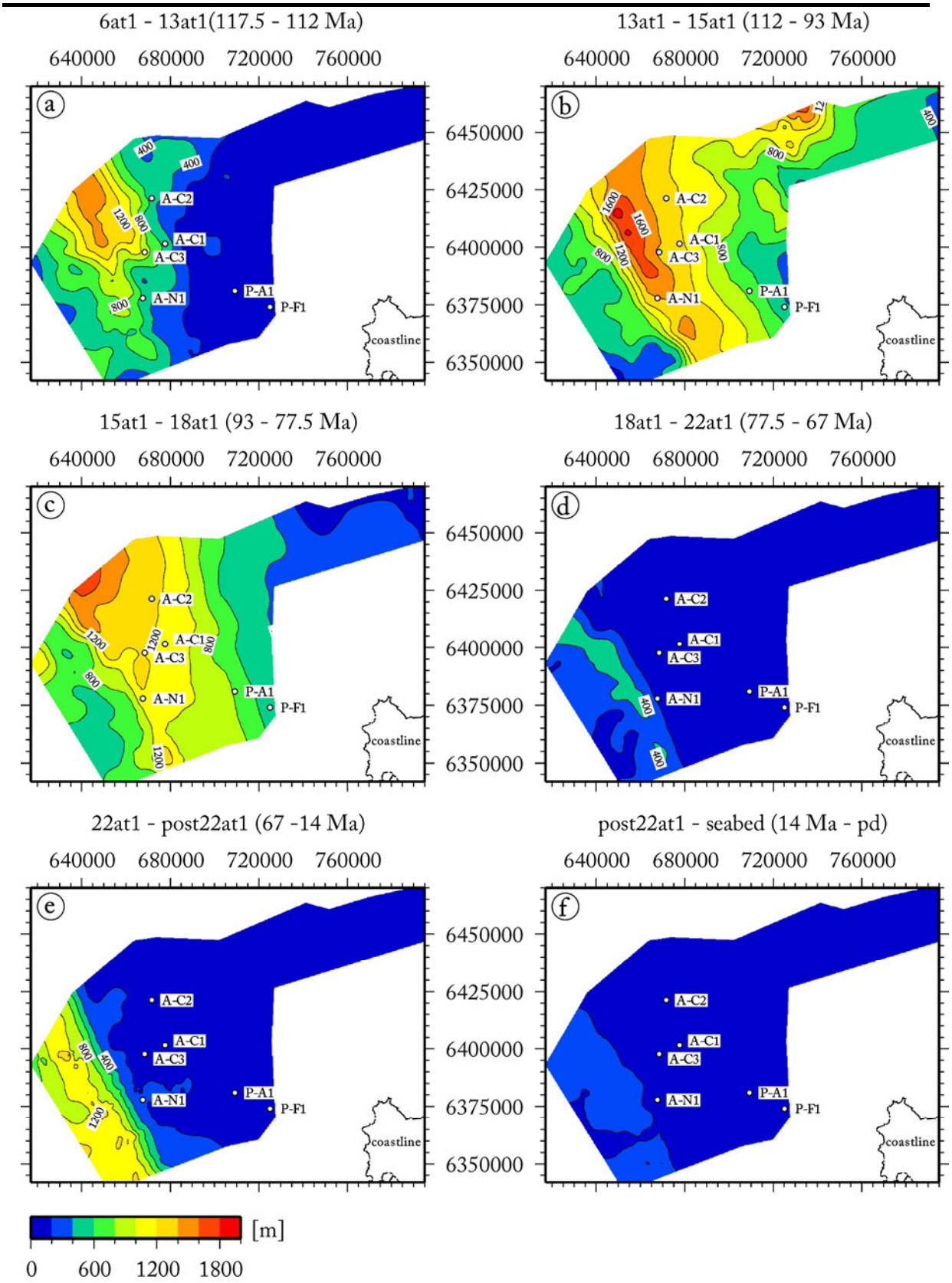

Figure 30: Thickness maps of the main sedimentary sequences for different time intervals derived from seismic interpretation.

Faulting affected restricted areas of the slope break.

While sedimentation was concentrated on the middle margin from the break-up of continents until the Campanian time period, the main depocentre shifted seawards onto the outer margin in more recent times.

A rather thin succession (> 500 m) of Late Maastrichtian age (18at1-22at1, 75-67 Ma) consists of deep-water chalks on the paleo upper slope encountered by well O-A1 (Figure 30d; McMillan, 2003). The outer margin was affected by post-depositional faulting (Paton et al., 2008). In the Latest Cretaceous, in Mid-Campanian, margin tilting and, linked to that, uplift brought sedimentation in the proximal parts of the Orange Basin to an end and let to erosion of the previously deposited successions (McMillan, 2003).

The timing of this erosional event is constrained by the youngest horizon found below the erosional unconformity, which is 77.5 Ma old, and by well data which document the deposition of sediments until Mid-Campanian times. The deposition of the horizon 22at1, which is 67 Ma in age, indicates the termination of erosion. Further evidence is provided by the absence of Maastrichtian sediments in the wells on the inner margin but deposition on the outer margin. Thus a minimum age of 74 Ma can be assigned for the initiation of erosion. Detailed mapping of the unconformity and the concordant nature of reflections was used to reconstruct the horizons geometry prior to erosion and to estimate the magnitude of erosion (Figure 31a; Kuhlmann et al., 2008). According to these estimates a maximum of 280 m of sediments has been eroded close to the coast whereas the amount of erosion is decreasing seawards. Wells A-C3 and A-N1 mark the outer limit of the area affected by erosion.

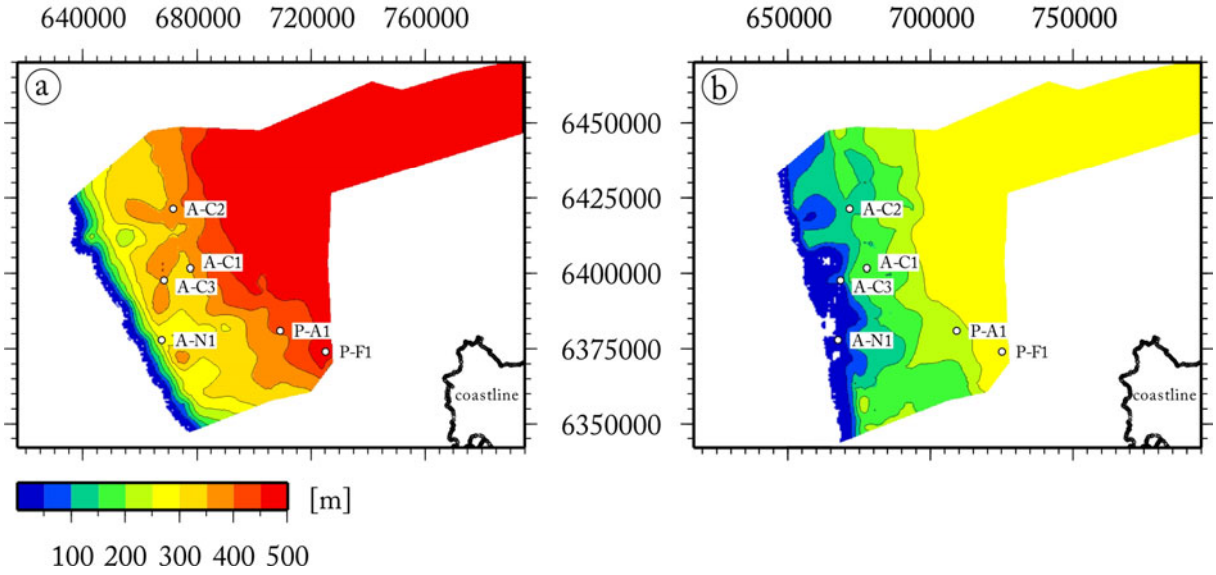

Figure 31: Maps indicating the amount of eroded material across the working area as derived from seismic interpretation **a)** amount of removed sediments between 74-67 Ma, **b)** sediments which were removed between 16 and 14 Ma.

The horizon 22at1 (67 Ma) defines the base of the Tertiary sedimentary wedge with thin Eocene or younger sediments resting on sediments of Coniacian to Albian age (Gerrard and Smith, 1982). The thickness of this wedge is increasing from a few hundred metres on the highly stable Cretaceous shelf to 1200 m on the outer shelf where the Eocene sediments rest on Maastrictian or Paleocene sediments (Figure 30e; Gerrard and Smith, 1982). The preserved thicknesses of these sediments indicate a seaward shift of the main depocentre. Since the

Tertiary these strata have been affected by margin instability and gravity faulting. Slumping is common throughout the Cenozoic succession (Faulkner, 2000) due to rejuvenation of older faults expressed in the development of growth faults and toe-thrust systems on the outer margin (Paton et al., 2008; Brown et al., 1995). Claystones and sandstones compose the bulk of the Lower Tertiary successions (Gerrard and Smith, 1982).

Tectonically driven renewed margin uplift led to the establishment of an erosional unconformity in response of which material is only preserved in the proximal deep water domains (McMillan, 2003). Like for the first erosional event, estimates on the amount of erosion have been derived from seismic interpretation and well information (Figure 31b). Seismic interpretation suggests that this 2nd phase of erosion ceased when the deposition of the 14 Ma old horizon started. Unfortunately, no further constraints are available to assess the onset of erosion. The Upper Tertiary succession is found to consist of sandy and shelly limestone and calcareous sandstones based on occasional bit samples (Gerrard and Smith, 1982). The water depths remained always relatively shallow; the deepening towards the present-day water depth occurred later than Maastrichtian times (McMillan, 2003). On top of the successions a thin veneer represents the sedimentation from 14 Ma until present-day (Figure 30f).

4.3 Method

A combined approach of subsidence analysis and forward modelling (Van Wees and Beekman, 2000; Van Wees et al., in press) was chosen to gain better insights into the interplay of tectonics and subsidence. Therefore, we initially carried out a 1D analysis of the well data using a two-step procedure: First, a geohistory analysis was carried out for the wells to determine the tectonic subsidence, which is to say, the process of deposition was reversed for each well using a backstripping technique. Second, 1D forward models for lithospheric stretching have been calculated and compared to the tectonic subsidence derived from backstripping. Changes have been successively applied to the forward models until a match between modelled and 'observed' tectonic subsidence was obtained. These changes relate to different mechanisms that may have influenced the subsidence history such as uniform or depth-dependent stretching and the effects of underplating.

Having obtained a reasonable tectonic history for the 1D case based on real wells we applied the respective forward scenario to the 3D model and evaluated the implications for the subsidence evolution and the thermal history in areas lacking well control.

4.3.1 Backstripping

The technique of backstripping is commonly applied to extensional basins to determine the magnitude of lithospheric stretching from the observed post-rift subsidence (Sclater and Christie, 1980). Stratigraphic units within a sediment column are removed progressively from top downwards and the remaining sediments are decompacted and isostatically restored using Airy isostasy. Thus, the restoration accounts for the new load conditions, the paleo water depth, and the isostatic response to the change in loads. The quality of any geohistory analysis is fundamentally dependent upon the quality of the paleo water depth information available (e.g. Roberts et al., 1998). Furthermore, the water body provides an additional load contribution to the isostatic response of the system and, in turn, to the observed subsidence. Besides erosional unconformities indicating zero water depth, information concerning paleo water depth usually comes from biostratigraphy. In a global

sense, the confidence level for foraminiferal biostratigraphy is unusually high in the basins of the South Atlantic (McMillan, 2003). Paleontological information was kindly provided by the Petroleum Agency of South Africa for the wells used in this study. Well reports document the general depositional environment through time and provide an estimate of paleo water depth. The interpreted chronostratigraphic plot of the Orange Basin provides good information on sea level fluctuations in Cretaceous times on a regional scale (McMillan, 2003). However, Cenozoic uplift of the margin and, linked to that, erosion partially removed the uppermost Cretaceous units. Thus, a reconstructed sea level curve must always remain incomplete (McMillan, 2003).

The output of backstripping comprises basically two subsidence curves. The first one, the basement subsidence, describes the subsidence the basement experienced as documented in the stratigraphy of the well. This curve is a composite of two components: (1) the effects of load induced subsidence driven by the presence of the overlying sediments and the water body and (2) the tectonically driven subsidence. The second curve, the tectonic subsidence, is obtained after subtracting the load-induced component from the total basement subsidence.

4.3.2 Forward models

A model was presented by Van Wees and Beekman (2000) for automatic forward modelling of subsidence data. This approach has been further developed and extended to account for important effects for heat flow and maturity modelling (Van Wees et al., in press).

Both, pure-shear uniform stretching (McKenzie, 1978) as well as depth-dependent differential stretching (e.g. Royden and Keen, 1980) can be simulated with the modelling approach. Furthermore, the effects of underplating can be determined. The thermal evolution is calculated for the syn-rift evolution and subsequent phases of cooling (Van Wees and Stevenson, 1995). Here, a minimisation technique is used to evaluate those stretching parameters that best reproduce the 'observed' tectonic subsidence. Predefined parameters are listed in Table 2 and comprise among others the initial thickness of the crust and lithosphere as well as the onset and duration of rifting (Van Wees and Beekman, 2000 and references therein). A detailed description of the modelling procedure and the physical background is given by Van Wees et al. (in press) and Van Wees and Beekmann (2000).

The uniform stretching model predicts the first-order lithospheric responses to continental extension, notably crustal thinning and geotherm perturbation (McKenzie, 1978; Kusznir et al., 1995). Two competing mechanisms proceed during rifting; lithospheric thinning is associated with an isostatic response of subsidence, whereas the disturbed lithospheric temperature field and the linked increase in the geothermal gradient causes uplift. The resulting net-effect generates syn-rift subsidence. The perturbed temperature field re-equilibrates in an exponential manner after rifting ceases. The subsidence curves are characterised by rapid subsidence first, followed by increasingly slowing subsidence in the post-rift phase. The respective decay time is about 60-70 Ma (Bott, 1992; Kusznir et al., 1995; Roberts et al., 1998).

Departures from the subsidence predicted by the uniform stretching model can be interpreted as additional thermal disturbances to the basin system that are not accounted for. These thermal disturbances may be a result of multi-phase, differential stretching or of magmatic underplating or a superposition of both (Kusznir et al., 2005; Van Wees et al., in press.). The magmatic character of the South African continental margin and the presence of

ⓐ

model parameter	units	value
inital lithospheric thickness	[km]	146
inital crustal thickness	[km]	36
surface crustal density	[kg/m³]	2900
surface mantle density	[kg/m³]	3300
surface density underplate	[kg/m³]	3000
crustal conductivity	[-]	2.6
mantle conductivity	[-]	3
heat production in the upper crust	[microW/m³]	depends
heat production in the lower crust	[microW/m³]	0.5
lithosphere thermal expansion	[-]	3.50E-05
base lithospere temperature	[°C]	1330

ⓑ

	ϕ_0	zscale	zscale change	zscale 2
sandstone	35	2300	1000	2000
shale	68	1500	500	1500
silt	50	1800	1000	2000
limestone	50	1400	500	2000

Upper part: $\varphi(z)\big|_{z<=zscalechange} = \varphi_0 e^{-\frac{z}{zscale}}$

Lower part: $\varphi(z)\big|_{z>zscalechange} = \left(\varphi_0 \frac{e^{-\frac{zscalechange}{zscale}}}{e^{-\frac{zscalechange}{zscale2}}} \right) e^{-\frac{z}{scale2}}$

Table 2: Predefined model parameters **a)** thermal parameters in the lithospheric stretching model **b)** double-porosity-depth curves used for the decompaction of the sediments throughout the backstripping approach.

a high density, high velocity body in the lower crust indicate that underplating has influenced the margin.

Furthermore, the observed phases of uplift and erosion in the late drift phase as well as the elevated vitrinite reflectance values point to thermal uplift related to phases of mantle attenuation long after continental break-up. We therefore evaluated the thermal consequences of these processes for the Orange Basin.

4.4 Results

First, we present and discuss different 1D models consistent with the constraints available for the wells. Beside the stratigraphy and lithology-dependent physical properties (porosity-depth relations, densities, thermal conductivity and radiogenic heat production; Table 2) these constraints include vitrinite reflectance data. Subsequently, the model that reproduces the observed tectonic subsidence and vitrinite reflectance best is applied to synthetic wells created for the gridpoints of the 3D model to derive predictions for un-drilled areas.

4.4.1 Tectonic subsidence

Figure 32a shows a compilation of the tectonic subsidence curves after backstripping of the wells. All curves are characterised by a moderate slope of initial subsidence as long as the rifting proceeds from 136 until 117.5 Ma. The transition to the drift stage is linked with an increase in subsidence rates from 117.5 to 112 Ma. For most of the wells the gradient is considerably steeper in the early post-rift phase than during initial (syn-rift) subsidence.

Subsequently, from Aptian (112 Ma) until the end of the Cenomanian (93 Ma) the steepness of the curves decreases again and they continue in a rather moderate pattern characteristic for 'normal' thermal subsidence.

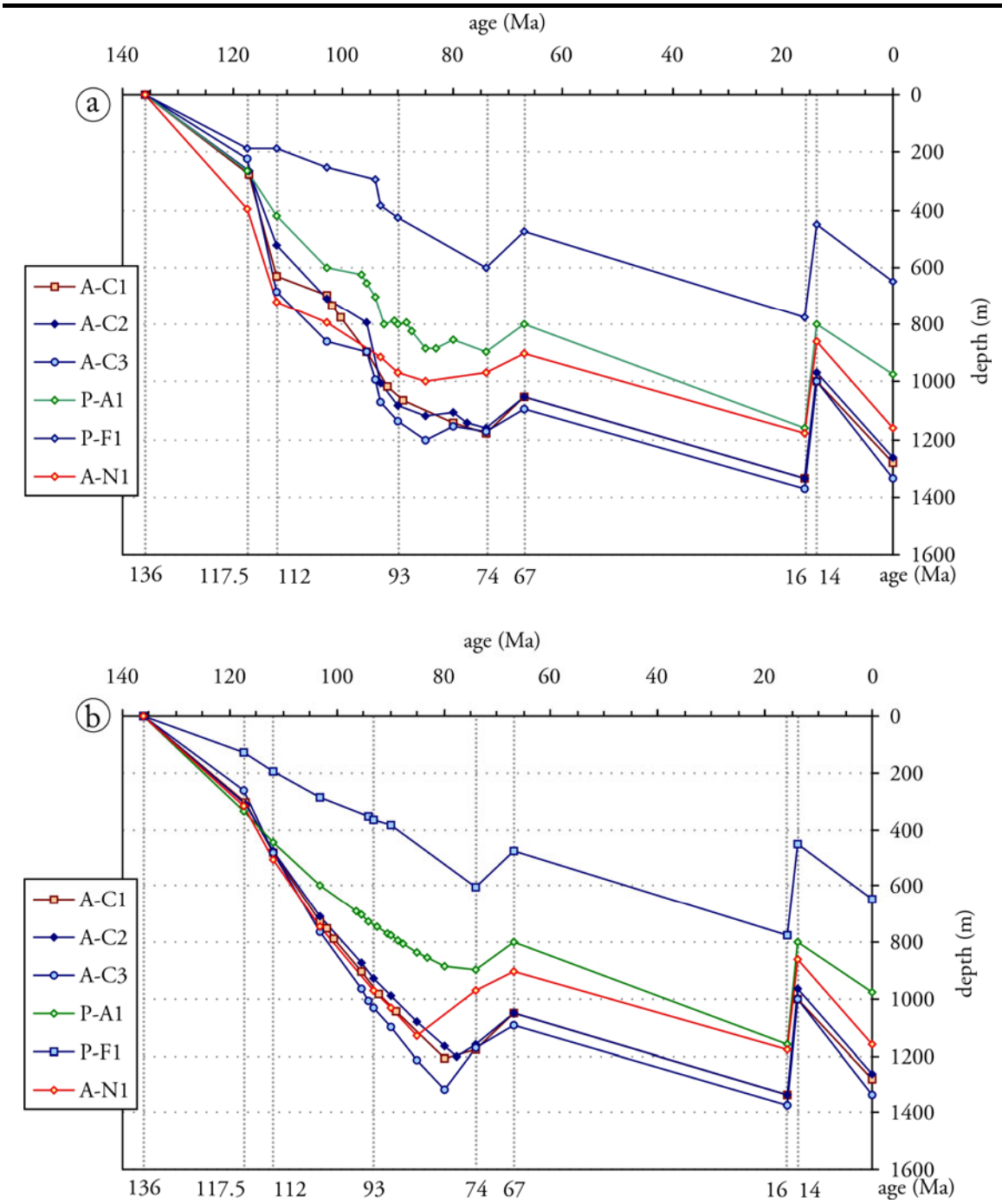

Figure 32: a) Compilation of the tectonic subsidence curves after backstripping of the wells. **b)** Plot of the according forward models that fit the observed tectonic subsidence best for the backstripped wells.

Here, it is notable that the end of this time interval is depicted by accelerated subsidence for wells in which this period is resolved with more than one data point.

Within the next 19 Ma (until 74 Ma) subsidence occurs with highly variable patterns. Depending on the temporal resolution of the single wells short periods of almost no subsidence, periods of intensive subsidence and also periods of slight uplifts can be observed.

Around 75 Ma, all the wells are affected by uplift which coincides with erosion. Erosion has been incorporated assuming zero water depth. The estimated amount of erosion is based on seismic interpretation and consistent with the erosion maps given in Figure 31.

Depending on the position of the individual wells and the amount of eroded material the pure tectonic uplift varies between 126 m for well P-F1 and 75 m for well A-C3.

The time interval from 67 Ma until the onset of the next erosional phase at 16 Ma is not well resolved within the wells. Seismic data in the distal domains west of the shelf break image Early Tertiary units cut by the erosional unconformity, but no wells are available to calibrate stratigraphy in detail. The maximum age of the erosional unconformity is constrained by the first overlying Miocene (14 Ma) unit. As no further constraints were available for the onset of erosion, this second, more intensive phase of erosion was assumed to start at 16 Ma for the modelling and to last until 14 Ma. The resulting amount of uplift ranges from 368 m (well A-C2) to 320 m (well A-N1).

From 14 Ma until today the margin is affected by moderate subsidence. No further data points are available within this interval from well logs which renders a better resolved, detailed subsidence reconstruction impossible. Again, the only source of information is seismic data that image a highly variable appearance of this youngest layer where particularly slumping renders correlation between individual wells difficult.

4.4.2 Forward models

After having obtained the tectonic subsidence history for all wells from backstripping, we tried to find forward models that reproduce this 'observed' subsidence pattern. The initial setting for all tested models consists in a lithosphere with an initial thickness of 146 km including a crust 36 km thick.

The results of the model that fits the observed tectonic subsidence best are plotted for all wells in Figure 32b.

The model results obtained for well A-C1 are shown to illustrate the differences between the tested forward models and discussed substitutional for all wells. As additional information, basement subsidence as well as tectonic subsidence and paleo water depth are shown for reference (Figure 33).

In the first instance, a uniform stretching model was tested in order to fit the 'observed' tectonic subsidence (Figure 33b, red curve). Due to uniform instantaneous stretching by a factor ß=1.41 for both, the crust and the mantle, the thickness observed for the crystalline crust today (> 25 km in well A-C1) is predicted. At the same time an initial basin of 602 m depth is created, which is far too deep when compared to the basin depth of 305 m in the backstripped curves. Thermal cooling commences subsequent to the rifting phase and uniform continuous subsidence creates a basin of steadily increasing depth consistent with present-day basement depth. Neither variations of ß nor of the initial lithosphere thickness reproduced the 'observed' tectonic subsidence as the initial subsidence always was too fast, and, of course, later phases of erosion remained unconsidered. Therefore, a number of effects have been included in the forward models which depart from the initial uniform stretching model.

underplating

We evaluated the effect of underplating which is considered to be emplaced in the syn-rift phase in our forward models. The density of molten rocks generated by decompressional melting is midway between the density of continental and oceanic crust and ranges between 2990 and 3070 kg/m³ for potential temperatures of 1280°C and 1480°C (Allen and Allen, 2006). Therefore, the density of the underplated material was defined to be 3000 kg/m³ and we assume an emplacement temperature of 1300°C. Lithospheric mantle (density of

3300 kg/m³) is replaced if these melts are trapped underneath the crust and the resulting net-effect when isostasy applies is uplift compared to a uniform stretching model without magmatic activity. Assuming that the lower crustal, high density body modelled for the same study area by Hirsch et al. (2007) represents the present-day relict of the syn-rift underplating we use the configuration of this body as constraint for the forward model. Accordingly, the respective thickness of the underplated material for well A-C1 is 12 km and it varies between 3 and 13 km across the rest of the working area.

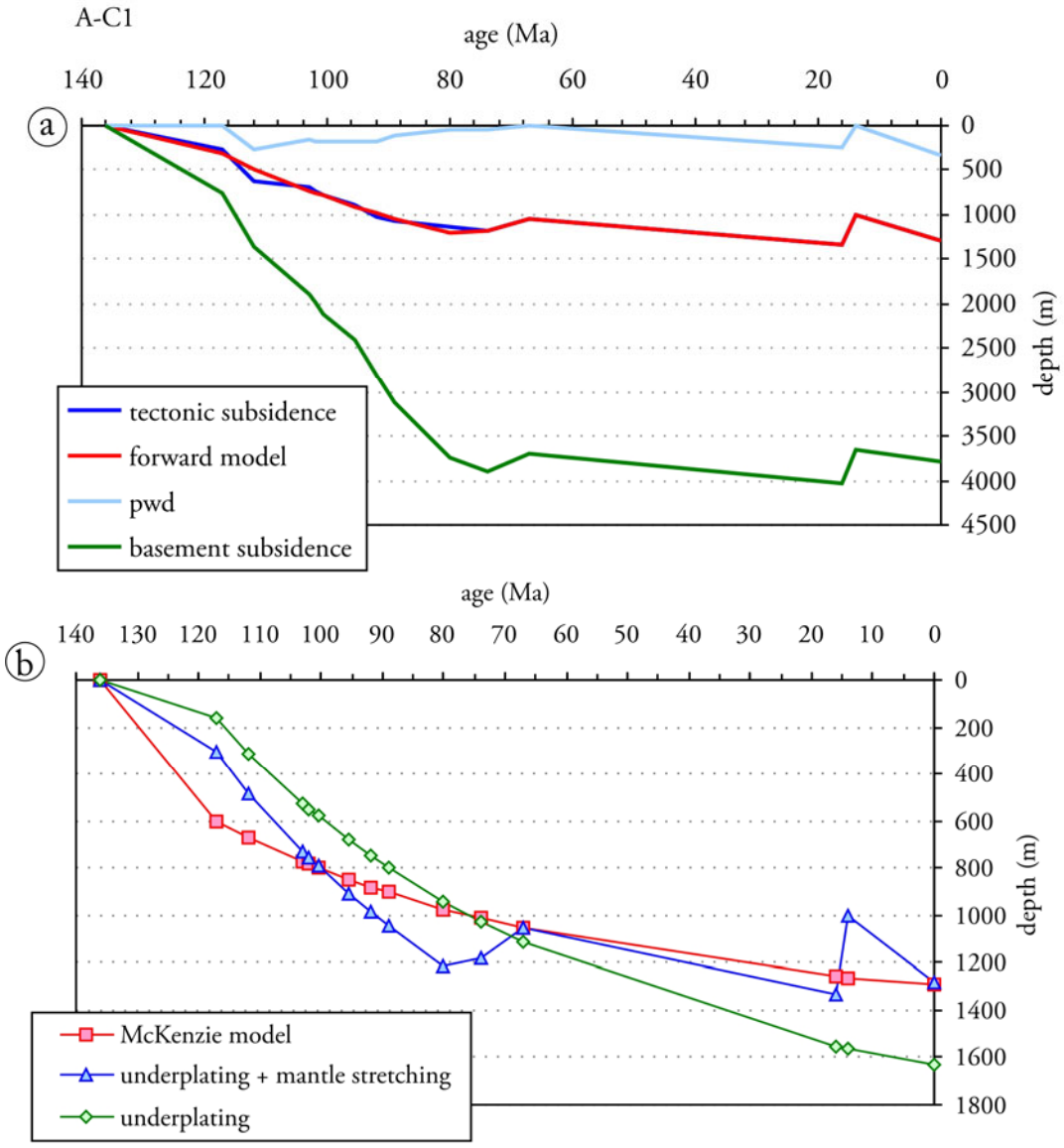

Figure 33: a) Subsidence curves for well A-C1: in green is shown the basement subsidence and in blue the tectonic subsidence curve. The latter is overlain by the tectonic subsidence curve predicted by the best-fit forward model. The light blue curve documents the paleo water depth distribution used throughout the modelling for well A-C1. **b)** Forward models for well A-C1. Whereas the red curve obeys the rules of a uniform stretching model (McKenzie, 1978) and considers only uniform stretching, the green curve incorporates the emplacement of underplating in the syn-rift stage. The blue curve represents a model which accounts for underplating and also mantle stretching from 74 Ma on.

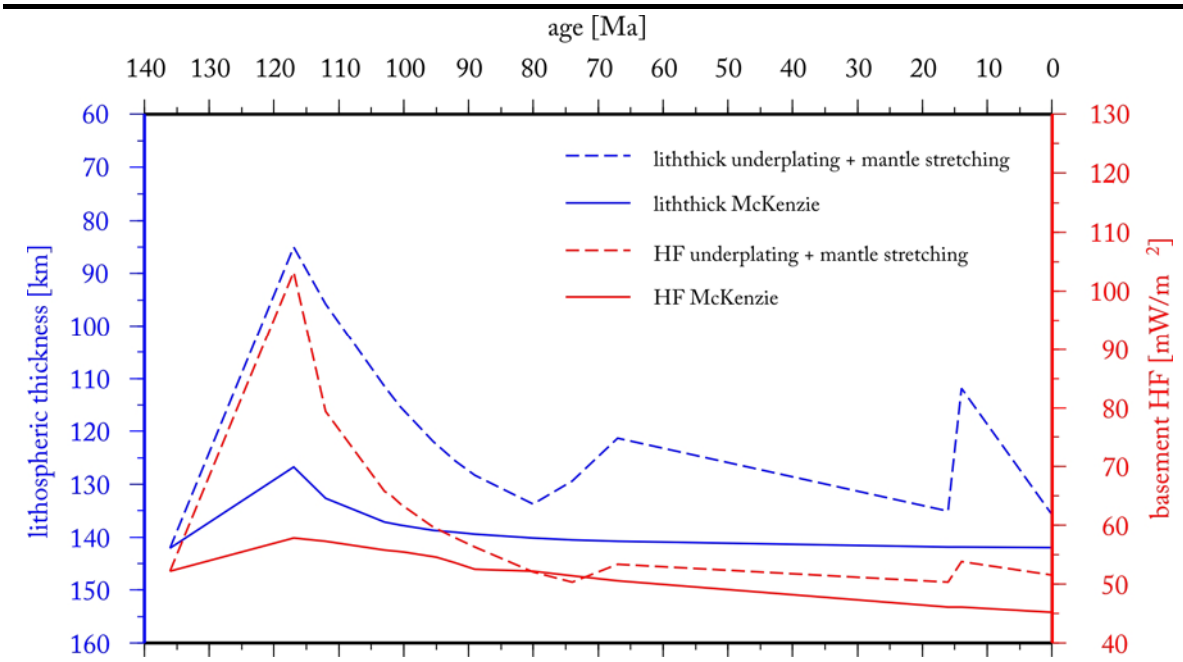

Figure 34: Heat flow evolution (in red) and development of the lithospheric thickness (in blue) compared for two models: Solid lines indicate the uniform stretching model (McKenzie, 1978) whereas dashed lines represent the best fit forward model including departures from the uniform stretching model such as underplating and post-rift stretching of the lithospheric mantle.

Considering the emplacement of the underplated body decreases the slope of the initial subsidence (Figure 33b, green curve). This reduces the initial subsidence of the basin to 165 m in the forward models and thus results in a better match with the backstripped, tectonic subsidence than achieved by the uniform stretching model.

The consideration of underplating also affects the thermal regime in the sedimentary basin (Fjeldskaar et al., 2003) in that it increases the heat flow in the basin due to the emplacement of hot material (Allen and Allen, 2006). The respective heat flow evolution is compared for both models in Figure 34. In the uniform-stretching-case, rifting is accompanied by an increase in basement heat flow of >10 mW/m². Incorporating underplating elevates the peak heat flow by ~50 mW/m² to ~100 mW/m² for the syn-rift phase.

The uniform stretching model predicted a lithospheric thinning of 30% for well A-C1. In contrast, the emplacement of a 12 km thick underplating enforced stronger stretching of the crust to ~10 km (β=3.27) which is consistent with the crustal structure presented in Figure 28. Since mantle material is replaced, the net effect is a reduced initial subsidence in the syn-rift phase compared with the uniform stretching model. The underplated body becomes part of the crystalline crust within the post-rift phase. Thus, the cumulative thickness of the crust becomes 22 km and the effective stretching factor becomes 1.54.

Summing up, the model changed due to the presence of the underplating into a depth-dependent stretching model.

Underplating not only significantly influences the initial stages of basin evolution, but also affects the post-rift subsidence pattern. Due to the addition of further, hot material the post-rift thermal cooling becomes more effective and the final basement depth is predicted to be much deeper than observed (Figure 33b, green curve). Though the fit with the observed tectonic subsidence is improved for the early stages of basin evolution if underplating is considered, the model furthermore does not account for the observed phases of uplift during

the late drift phase. These phases are, however, observed and require explanation. Phases of late tectonic uplift are observed at many passive margins and the related mechanisms are still a matter of debate (Watts and Fairhead, 1999; Fjeldskaar et al., 2003; Gernigon et al., 2004). Possible causes behind margin uplift include renewed phases of sub-crustal stretching, rift shoulder uplift in consequence of renewed extension, far-field compression due to ridge push forces or additional thinning of the sub-crustal mantle in response to either mantle plumes or small-scale convection (Boutillier and Keen, 1999). As neither indication for compressive deformation nor for extensional faulting are present in the seismic data of the Orange Basin, we explore how far the effects of sub-crustal stretching prior to the two major phases of uplift are consistent with the observed tectonic history and thermal maturation data.

sub-crustal stretching

Seismic and well data document two phases of erosion that have removed in places up to 500 m of sediments. Thus the 2nd tested departure from the uniform stretching model was the implementation of mantle stretching coeval to the observed erosional phases to account for thermal uplift. The thinning of the lithospheric mantle provokes upwelling of the asthenosphere. Thus denser lithospheric mantle is replaced by less dense asthenospheric material and results in isostatic uplift. If the net uplift surpasses the erosional level, material is removed from the system which in turn results in a mass deficit. This prevents complete re-equilibration of the system during post-rift cooling and therefore leads to net subsidence. The effects of mantle thinning are demonstrated for well A-C1 (Figure 33). The lithosphere is thinned to ~85 km in the syn-rift phase. Subsequently, thermal re-equilibration thickens the lithosphere again and at 74 Ma, more than 40 Ma later, the lithosphere almost regained its initial thickness. So far the model does not depart from the previously described model which incorporates initial uniform stretching and underplating. Differences occur in the post-rift phase.

The onset of the elder phase of erosion (74 Ma) is used herein as the beginning of the renewed mantle stretching. This thins the lithosphere again to 121 km which corresponds to a cumulative stretching factor of 1.1. Here, the lithosphere is ~20 km less thick than predicted by the uniform stretching model. Considering that the crust has not been affected by thinning the net stretching factor for the sub-crustal mantle amounts of 1.13. For the other wells the cumulative stretching factor for the 1st uplift phase ranges from 1.03 to 1.06 (Table 3).

event	A-C1			A-C2			A-C3			A-N1			P-A1			P-F1		
	$\beta_{eff.}$	δ	uplift	$\beta_{eff.}$	δ	uplift	$\beta_{eff.}$	δ	uplift	$\beta_{eff.}$	δ	uplift	$\beta_{eff.}$	δ	uplift	$\beta_{eff.}$	δ	uplift
rifting	1.54			1.51			1.66			1.51			1.41			1.14		
74-67 Ma		1.13	132		1.06	112		1.04	80		1.04	68		1.04	100		1.03	125
16-14 Ma		1.26	345		1.27	379		1.34	388		1.30	317		1.18	367		1.13	325

Table 3: Listing of the modelling results, which include the syn-rift crustal stretching values, post-rift stretching factors for the lithospheric mantle and the related amount of uplift which the margin experienced.

Figure 35 shows a compilation of the lithospheric thickness through time for each well. Subsequent relaxation of the mantle allows a re-coverage of the lithospheric thickness until the 2nd phase of uplift. The timing of the 2nd phase starts at 16 Ma, marking the onset of

erosion. Since this 2nd phase of erosion is marked by higher sediment denudation mantle stretching reaches considerably higher values than during the 1st phase. For well A-C1 the lithosphere is thinned from 135 km to 111 km; this corresponds to a cumulative beta factor of 1.21. The stretching values vary between 1.13 and 1.34 for the other wells (Table 3).

These phases of mantle thinning prevent thermal re-equilibration of the thermal system and result in higher heat flows compared to the uniform stretching model even though the stretching itself is only linked to minor heat peaks.

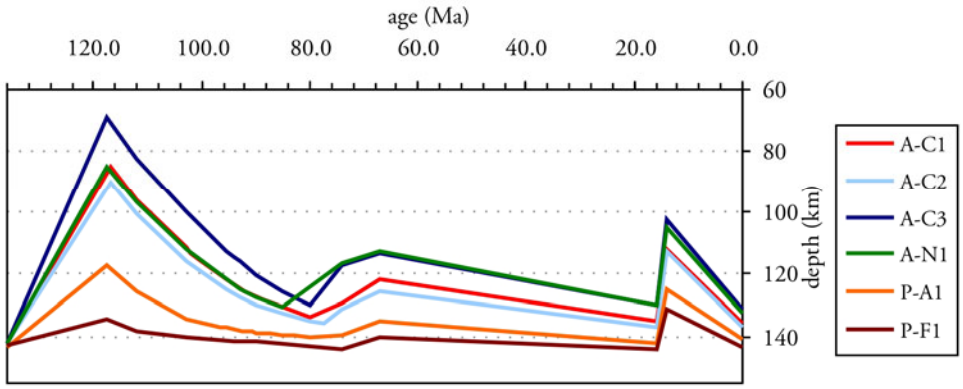

Figure 35: Evolution of the lithospheric thickness through time for all backstripped wells as predicted by the best-fit forward models.

heat flow

In implementing the explained and described departures from the uniform stretching model, we obtained a forward model which reproduces the observed subsidence pattern. However, the models should also be consistent with the observed vitrinite reflectance profiles. Accordingly, we evaluate the thermal history predicted by the forward model and investigate implications for the hydrocarbon generation. Especially, basement heat flow is one of the most influential parameters on the maturity of organic matter throughout basin evolution. The modelling approach enables the calculation of maturation based on probabilistic heat flow scenarios, taking uncertainties from lithospheric stretching into account. Furthermore, the effects of depth-dependent porosities and related changes in thermal conductivity are considered (cf. Van Wees et al., in press). We used the calculated basement heat flow for the best fit tectonic model for the maturation modelling adopting the kinetics of kerogen typ IV incorporating the activation energies of Burnham and Sweeney (1989).

Uncertainties related to parameters such as lithospheric and crustal thickness, estimates on erosion, paleo water depth and the porosity depth relations are evaluated in a sensitivity analysis and help to define critical parameters in the modelling approach. These uncertainties can be narrowed if information on temperatures and maturation in the wells is provided. Such data were available for the Orange Basin and have been used to cross-check the forward models thermally.

The predicted heat flow history for well A-C1 predicts a present-day heat flow of 51 mW/m² the according surface heat flow is about 56 mW/m². These numbers are slightly higher as predicted for old oceanic domains (~50 mW/m²; Stein and Stein, 1992). The well is underlain by underplating of 11 km. The heat contribution of this mafic feature is negligible.

Since the sediments contribute a maximum of 5 mW/m², the main component of heat flow must originate from the mantle.

As a general trend, the vitrinite reflectance measured in the wells of the Orange Basin show elevated values in comparison to the trend in a global compilation (Allen and Allen, 2006 and references therein) and are generally higher than expected from the present burial depth. This points to a thermal overprint either due to larger initial maximum burial and subsequent erosion or due to an additional heating event. Our tectonic forward model incorporating initial stretching with underplating and two late-stage phases of erosion predicts elevated values of vitrinite reflectance that are in good agreement with the measured values (**Figure 36**). Accordingly, the predicted heat flow history would explain the present-day maturity of the sediments.

For the A-wells, however, the modelled trend in the vitrinite values is still lower than in the measured samples. Especially in the uppermost 2.5 km, the modelled values are displaced parallel to the measured values. This indicates that sources of error are probably not related to the chosen rock specific parameters as the thermal conductivity or the porosity-depth-relations. Suspicious thermal parameters would rather be expressed in a differing gradient of the vitrinite increase with depth than in a parallel displacement and increased surface values. Therefore, other processes must be responsible for the general misfit. The character of the parallel displacement indicates that a rather young process was active since samples over the entire depth have been affected and overprinted. In a sensitivity analysis, we evaluated the influence of the amount of additional erosion. If thicknesses missing due to erosion are underestimated, also the maximum burial depth and the related maturation of the sediments are underestimated. The amount of eroded material was derived from seismic interpretation which is of course prone to uncertainties. Increasing the amount of erosion for the A-C wells to 1000 m and 900 m respectively results in a good fit between modelled and observed vitrinite reflectance (Figure 36b). This increased erosion, however, would require further mantle thinning. In detail, this would imply a thinning of the lithosphere to 100 km for well A-C1 whereas so far a thickness of 111 km was predicted for this event.

4.4.3 3D model

Assuming that the tectonic history derived for the single wells is also valid for the entire study area, the same approach has been applied to the previously described 3D model to derive predictions for areas where no well control is available.

Therefore, an equidistant grid of 234 synthetic wells with a spacing of ~10 km was generated for which backstripping and forward modelling has been carried out. The geohistory results derived from the real wells have been applied to these synthetic wells to investigate the subsidence history of the Orange Basin in a wider area constrained by seismic data only. Furthermore, spatial variations of parameters could be addressed and quantified throughout the basin.

As mentioned earlier, paleo water depth information is crucial in the geohistory analysis. To derive the required paleo water depth for areas without real well control we used a simple approximation. First, we carried out backstripping for all layers of the 3D model assuming an air loaded basin and local isostasy (Scheck and Bayer, 1999).

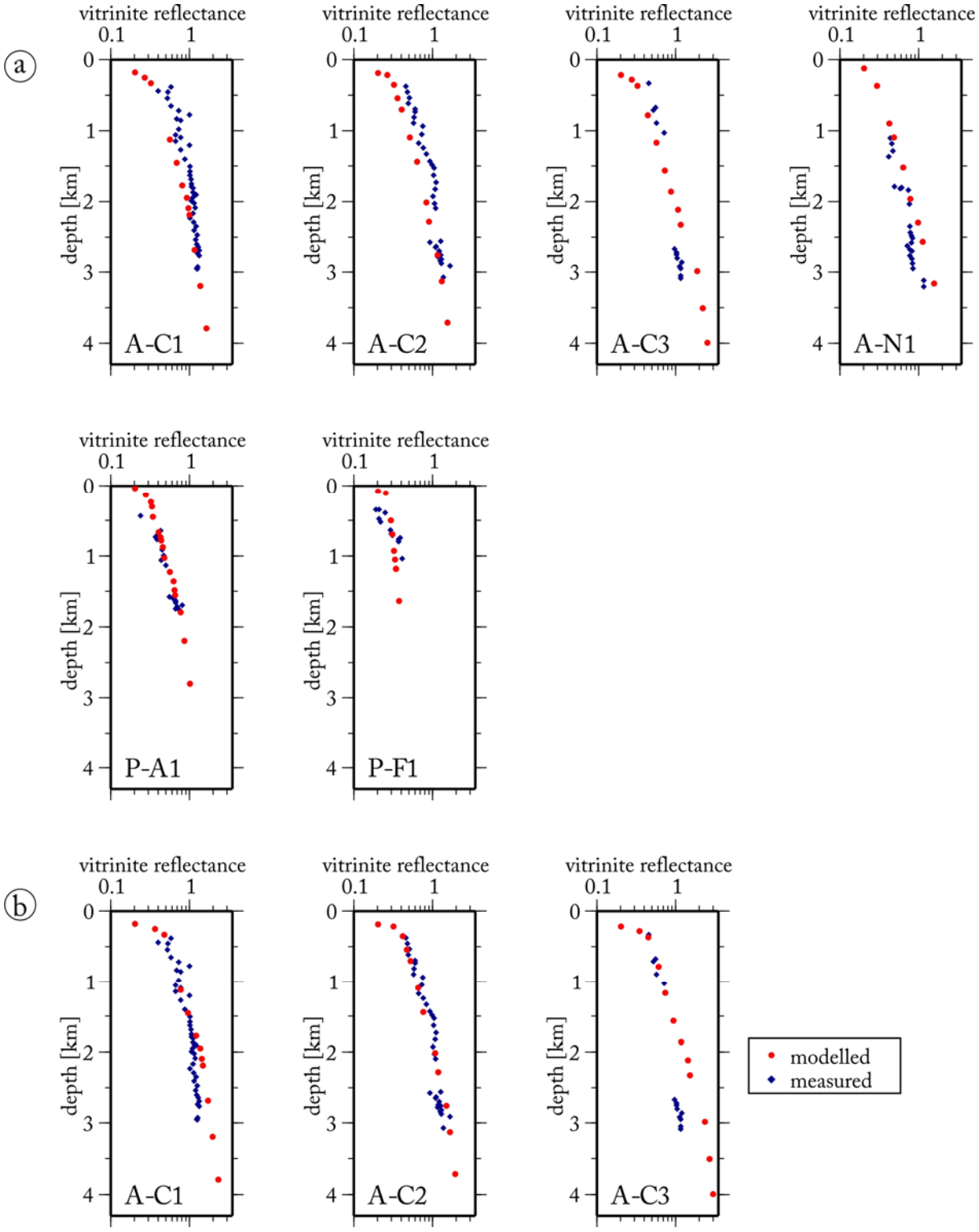

Figure 36: a) Comparison of the vitrinite reflectance profiles as predicted by the forward models to the measured maturity of each well. **b)** Comparison of the vitrinite reflectance as predicted by the forward models if more erosion is assumed as predicted by seismic interpretation to the measured maturity of each well.

The stepwise removal of stratigraphic units, decompaction of the remaining underlying layers, and the isostatic restoration reconstructs the topography of the respective horizon at the time of deposition. This topography is correct for air-loaded conditions and does not represent the correct bathymetry. Therefore, this topography was subsequently shifted vertically until the water column was consistent with the constrained paleo water depth reconstruction for the real wells. Thus, we obtained a good approximation for the lateral distribution of paleo water depth in agreement with the data from real wells but also considering isostatic principles and the effects of decompaction. Finally, backstripping taking these paleo water depth and erosional maps into account has been repeated for the virtual wells to derive the tectonic subsidence.

Figure 37 illustrates the lateral variations of this tectonic subsidence along two representative transects through the basin. Each diagram depicts the tectonic subsidence curve of a synthetic well and colours indicate the position of the well along the transect. The curves for synthetic wells along the north-south running profile on the shelf (Figure 37a) reveal that the post-rift subsidence displays a rather uniform, coeval subsidence pattern in north-south direction.

In contrast, the tectonic subsidence curves for the synthetic wells along a line which transects the basin in east-west direction (Figure 37b) differ from the proximal to the distal parts of the basin. According to increasing stretching factors from the proximal to the distal domain also the amount of tectonic subsidence increases seaward. Beside the absolute depth range all curves show a similar pattern as the same tectonic history is assumed for the entire area of the 3D model. Accordingly, the same sequence of events is observed in all synthetic wells.

After rifting had ceased at 117.5 Ma the basin underwent a short phase of relative rapid subsidence until 112 Ma. Within these first 5 Ma, the intensity of sagging is increasing with increasing distance to the coast. From 112 Ma onwards, smooth tectonic subsidence curves of moderate gradients indicate that a tranquil phase of subsidence prevailed in the basin. A minor event of short-lived uplift (91.5 Ma) occurred during this period affecting the entire margin before uniform and moderate subsidence continued until 77.5 Ma. At this point in basin evolution a steeper overall gradient of tectonic subsidence indicates renewed subsidence acceleration before a phase of uplift began at 74 Ma and lasted until 67 Ma.

Following this, the margin experienced renewed, continuous thermal subsidence until 16 Ma. Unfortunately, sparse data coverage prevents further analysis of this time interval.

Thereafter, a 2nd uplift event, larger in magnitude than the previous uplift, affected the basin from 16-14 Ma. Finally, the margin experienced another 14 Ma of subsidence until present-day.

Like in the 1D case for the real wells, the forward models for the synthetic wells predict the tectonic subsidence, the variation of stretching factors for the crust and lithospheric mantle and the thermal history, thus allowing an assessment of these parameters for the entire 3D model area.

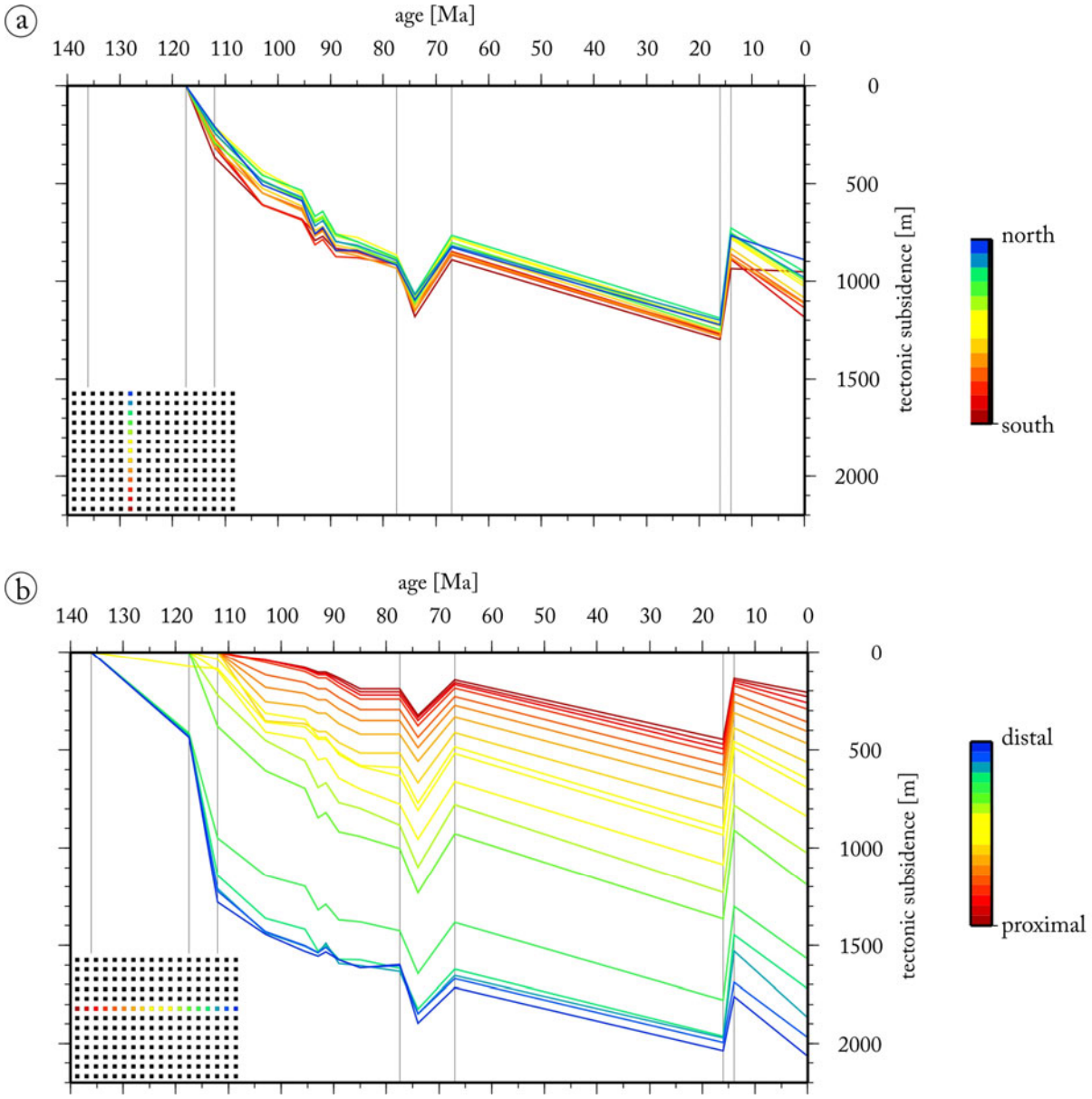

Figure 37: Illustration of the lateral variations of the tectonic subsidence along two representative transects through the basin. Each diagram depicts the tectonic subsidence curve of a synthetic well and colours indicate the position of the well along the transect **a)** synthetic wells along the north-south running profile on the shelf, **b)** tectonic subsidence curves for synthetic wells along a line which transects the basin in east-west direction.

rifting

The combined effect of uniform stretching and underplating for the initial rifting and the opening of the Orange Basin result in an increasing tectonic subsidence from the proximal to the distal domains of the basin. Accordingly, the tectonic subsidence for this time interval is consistent with the results of backstripping. Tectonic subsidence ranges between no vertical motion near the present coast and increases to 500 m of subsidence in the most distal parts. The effect of underplating prevents subsidence in domains where the effective stretching factor was smaller than 1.6 as the thermal uplift caused by the underplating counteracts the

rifting-induced subsidence. In these domains the margin appears to be unaffected by rifting in terms of initial subsidence.

The effective crustal stretching values vary between 1.0 close to the coast and 2.2 in the distal parts of the model (Figure 38).

At the same time, the lithosphere experiences a thinning to less than 60 km in the distal domains of the model, a thinning to 110 km in the vicinity of the A-wells and remained un-stretched in the most proximal domains. On the outer margin, where the beta values reach their maximum, the crust was thinned to less than 10 km post-rift thickness, which corresponds to the thickness of the crystalline crust observed today. This already indicates that the later tectonic phases did not lead to any further thinning of the crust, but where related to sub-crustal stretching.

Subsequent to rifting, thermal cooling starts and causes a re-equilibration of the system during which the thickness of the previously stretched lithospheric mantle is increasing again. This cooling appears to be the dominant driving mechanism for the subsidence of the basin. Accordingly, a deepening of the basin is predicted during the time interval (117.5-112 Ma) in which the tectonic induced component accounted for maximal 1000 m of subsidence (**Figure 39**a).

Again, the intensity of tectonic subsidence varies across the margin: On the inner shelf almost no subsidence was active but with increasing distance to the coast the intensity of tectonic subsidence increased and accounted for ~350 m depth near the A-C wells and 1000 m in the outer most domains.

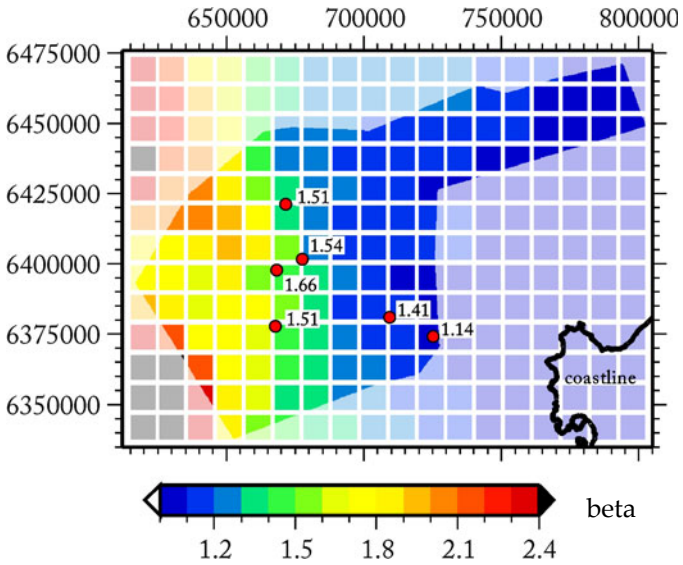

Figure 38: The distribution of effective crustal stretching values across the working area which varies between 1.0 close to the coast and 2.2 in the distal parts of the model. Red points indicate the position of the real wells and the calculated stretching factor for each well. Each rectangle represents one of the synthetic wells. The white mask outlines the area best constrained by seismic data.

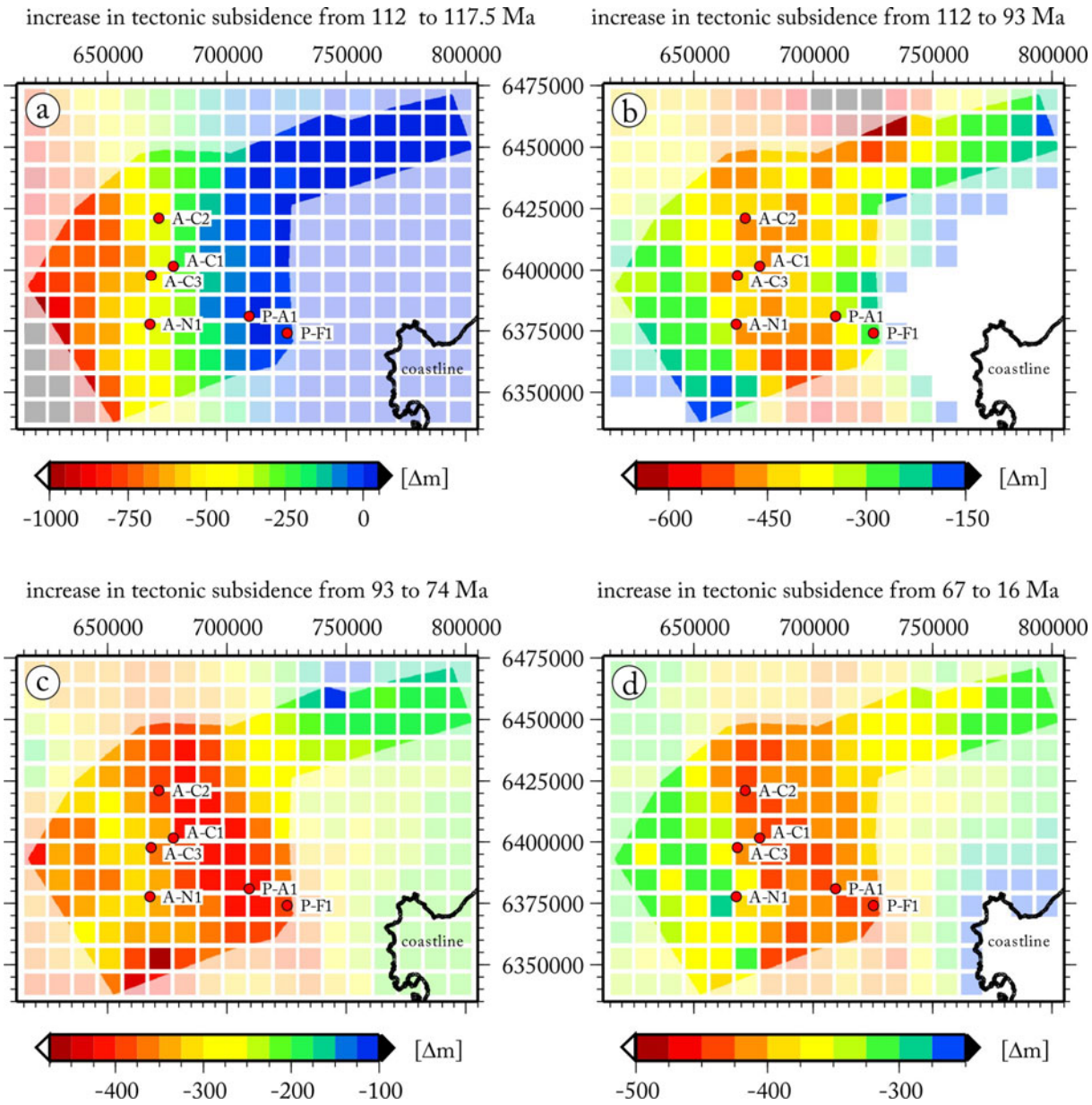

Figure 39: Map view of the increase in tectonic subsidence for several time steps. Details are given in the text.

112-93 Ma

From 112 until 93 Ma, the tectonic subsidence declines with respect to the proceeding time since rifting and varies from 200 m to 700 m across the basin. Maximum tectonic subsidence is focussed in a N-S striking corridor from 112-93 Ma (Figure 39b). The total accumulation space created by tectonics since the onset of rifting results from the superposition of the different phases of tectonic subsidence. Accordingly, the pattern of basement subsidence outlines a NW-SE striking depocentre on the inner margin where most of the sediments were deposited (cf. Figure 28b). Vast amounts of sediments were transported into this paleo depression and built up a delta of up to 1953 m in thickness, whereas the outer margin received only little sedimentation.

Contour lines of predicted temperatures in the Hauterivian potential source rock interval correlate spatially with contour lines of the maximum in sediment accumulation. Calculated

paleo temperatures within this source rock interval overstep 100°C in areas where more than 1000 m of sediments accumulated and exhibit a NW-SE striking maximum of up to 170°C where the overlying sediment package attains the largest thickness. In the overlying Aptian/Barremian source rock interval temperatures still exceed 70°C with a maximum of 140°C in the same area.

Thus, the process of sediment deposition dominates the thermal evolution in the sediments rather than the tectonically caused lateral variations in basement heat flow.

93-74 Ma

The increase in tectonic subsidence during the next-younger phase (93-74 Ma) reflects ongoing declining thermal subsidence that varies between ~200 m close to the coast and more than 400 m seawards (Figure 39c). At the end of this time interval at 74 Ma, a preliminary maximum in burial is reached, immediately before the margin experiences a phase of intermediate uplift.

At this stage, not only the basement depth reached a 1st maximum but also the temperatures within the source rock intervals. The Hauterivian source rock is subjected to 240°C in maximum in the north-western edge of the model. In the vicinity of the A-wells, where the thickest sediment portions were deposited, temperatures range between 140 and 180°C for this source rock. In the shallower Aptian/Barremian source rock interval modelled temperatures range between 120-160°C around the A-wells (Figure 40) and the uppermost source rock interval of Cenomanian/Turonian age is subjected to temperatures exceeding 100-140°C.

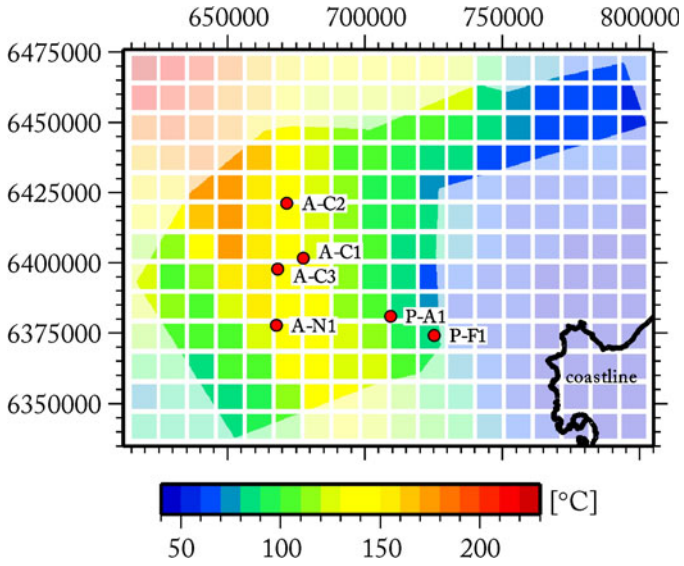

Figure 40: Spatial distribution of the temperature within the Aptian/Barremian source rock interval at 74 Ma.

Uplift from 74 - 67 Ma

The next time step in basin evolution from 70 Ma to 67 Ma is characterised by a phase of erosion of the inner shelf area. In order to remove the sediments the margin must not subside any further but needs to experience uplift to expose sediments to erosion. As detailed for 1D case, we assume mantle thinning as a possible mechanism behind this phenomenon, whereas the thickness of the crust does not experience further changes. So as to reproduce the

backstripped tectonic subsidence and the erosion estimates the required stretching of the lithospheric mantle varies between 1.1 and 1.2 (Figure 41a). The pre-uplift thickness of the re-equilibrated lithosphere in consequence of thermal cooling ranges between 120 km in the distal areas of the model and 146 km on the shelf as predicted by the forward model. In consequence of renewed mantle thinning this thickness is reduced to 107-140 km (Figure 41b).

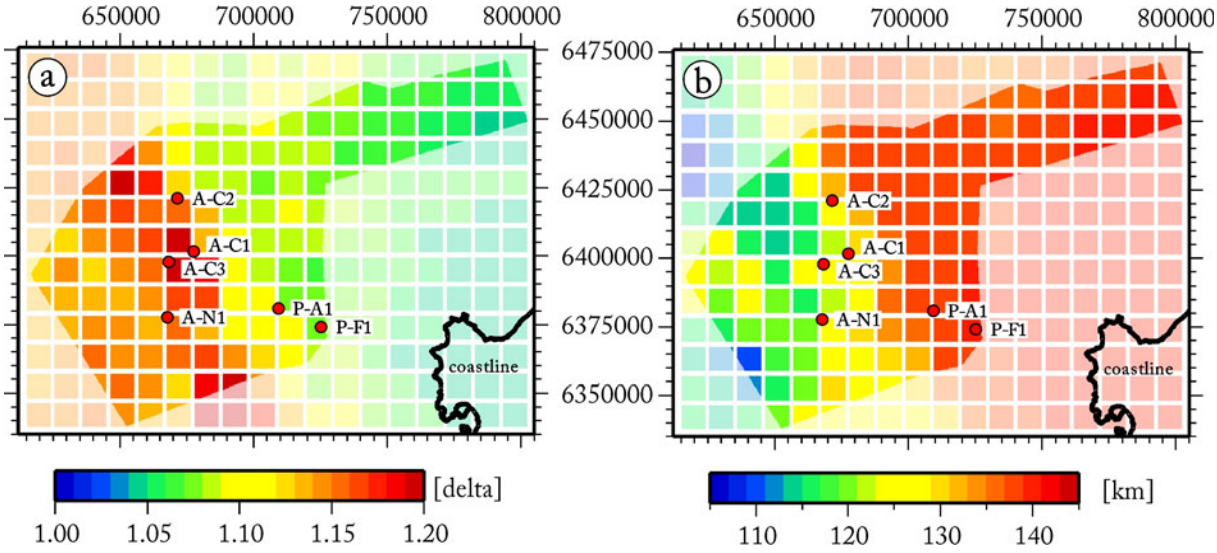

Figure 41: a) Spatial distribution of the required stretching factors of the lithospheric mantle between 74 and 67 Ma. **b)** Thickness map of the lithosphere in consequence of renewed stretching at 67 Ma.

The resulting net effect in terms of vertical, pure tectonically induced movement is a N-S striking corridor, encompassing the A-wells, that is exposed to maximum tectonic uplift of up to 340 m (Figure 42a). Adjacent to this corridor, the uplift exceeds 150 m all over the working area. Accordingly, the basement heat flow evolution from 74 to 67 Ma is characterised by an increase of up to 5 mW/m² on the inner margin (Figure 42b). Spatially, the distribution of the heat flow increase correlates with the area affected by erosion.

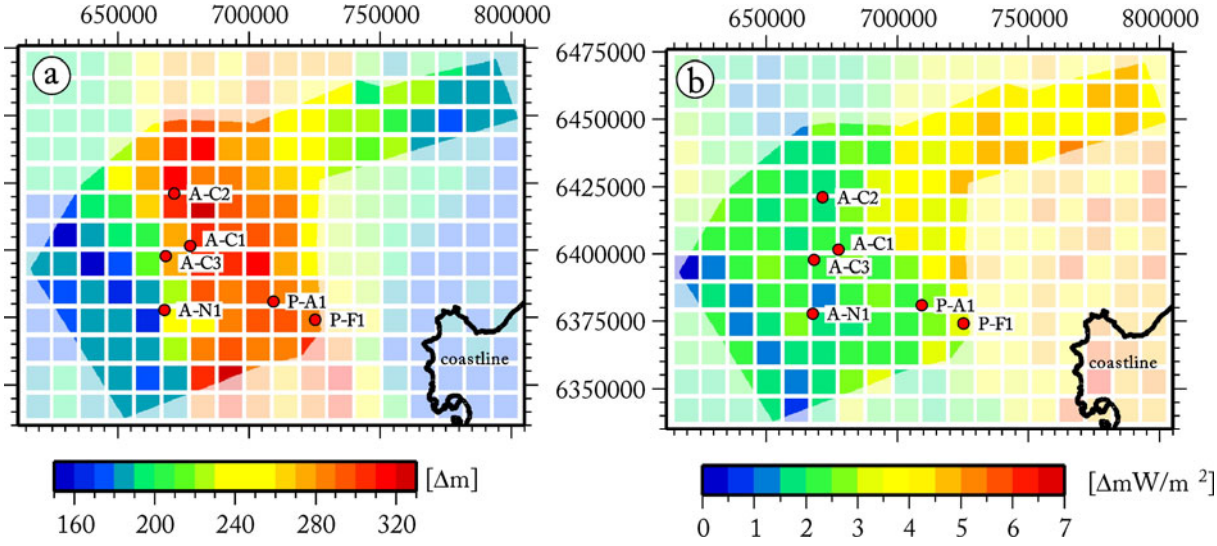

Figure 42: a) Map view of the calculated uplift across the margin documenting the pure tectonically induce vertical movement of the basin from 74 to 67 Ma. **b)** Map view of the increase in basement heat flow coeval to margin uplift between 74 and 67 Ma.

67-16 Ma

The deposition of a horizon dated to 67 Ma (22at1) documents the end of erosion and the onset of renewed margin subsidence. The following time interval until 16 Ma is limited upwards by a second major erosional unconformity, but is sparsely documented in the sediment columns since erosion and/or minor accumulation prevented the preservation of thick strata. Sediments are preserved predominantly seaward of the present-day shelf break on the outer margin. According to seismic data, up to 1500 m of sediments are preserved today on the outer margin documenting a rather moderate creation of accommodation space there (Figure 30e). On the inner and middle margin the reconstruction of the second phase of erosion documents the removal of about 500 m of sediments (Figure 31).

Prior to erosion, subsidence proceeded coeval to deposition and re-deepened the basin again until 16 Ma. Between 67 and 16 Ma tectonic subsidence contributed to this process ~300 m on the outer margin, ~450 m in a N-S corridor on the middle margin and less than 350 m farther landward (**Figure 39**d).

It was during this time interval that the source rocks experienced the deepest burial in the basin history which makes this interval the most interesting interval for hydrocarbon aspects.

Indeed, the model predicts that the temperatures within the source rock intervals exceed the temperatures experienced at 74 Ma as they are now overlain by a thicker sediment cover.

In the Hauterivian source rock interval the sediments of the outer margin are subjected to ~200°C, the middle margin experiences ~150°C and on the inner margin of ~70°C occur. At a shallower level, the temperatures of the Aptian/Barremian source rocks still reach ~180°C seaward of the A-wells where the largest sediment thicknesses accumulated. Temperatures decrease to ~120°C farther landward and vary between 70 – 90°C close to the coast (Figure 43). In the Cenomanian source rock interval temperatures of 150°C are reached in maximum in the distal domains of the model. Temperatures are continuously decreasing to ~90°C farther landward and on the inner margin this interval still has a temperature of ~60°C.

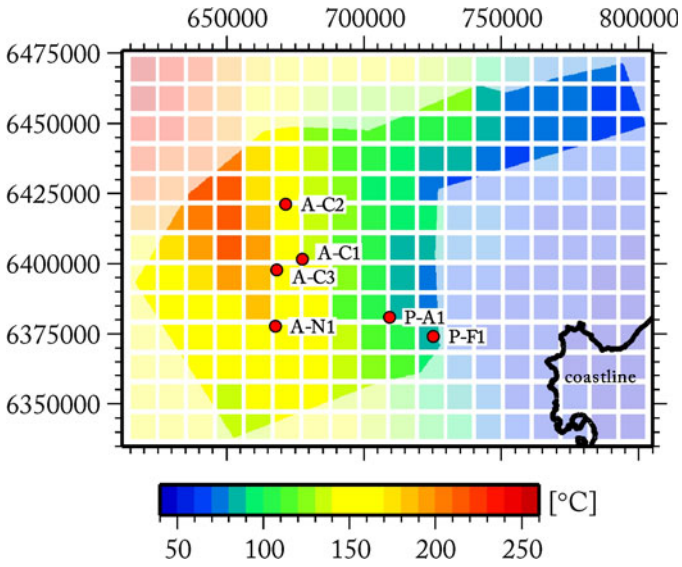

Figure 43: Map of the predicted temperature distribution within the Aptian/Barremian source rock at 16 Ma.

Uplift from 16-14Ma

As mentioned above, seismic data document erosion in the late Early Tertiary prior to 14 Ma which was estimated to amount 500 m at maximum (Figure 31b). Again, sub-crustal stretching was modelled to account for uplift and like in the 1D case, a duration of 2 Ma was assumed for the erosion event. The intensity of erosion during this phase of uplift is larger than the intensity of the 1st erosional phase and accordingly the amount of mantle thinning also exceeds that of the previous stretching event.

For the time interval from 16 to 14 Ma stretching factors for the lithospheric mantle were found to be smaller than 1.2 for the proximal half of the model. In the distal half of the models the factors are round about 1.25 and the stretching factor even overstepped 1.5 in the domain where most of the sediments accumulated (Figure 44).

The lithospheric mantle is thinned according to the distribution of the stretching factors and the stretched thickness varies between 100 km and 130 km.

Tectonic uplift ranged from 150 m to more than 300 m for the 1st tectonic uplift event (74-67 Ma). The 2nd more effective erosional event is, in turn, linked to more intensive tectonic uplift. The uplift varied between moderate values of 240 m on the outer margin and maximum values of 540 m concentrated on the middle margin whereas the inner margin experiences even 350-400 m of tectonic uplift (Figure 45a).

The increase in basement heat flow from 14 to 16 Ma is less than 8 mW/m² throughout the working area (Figure 45b) and outlines the realm which has been affected by erosion (Figure 31b).

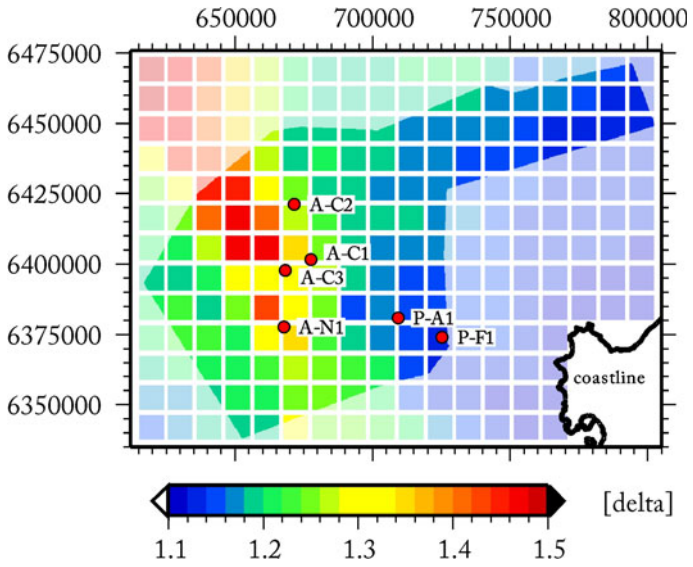

Figure 44: Map illustrating the spatial distribution of stretching factors for the lithospheric mantle for the time interval from 16 to 14 Ma.

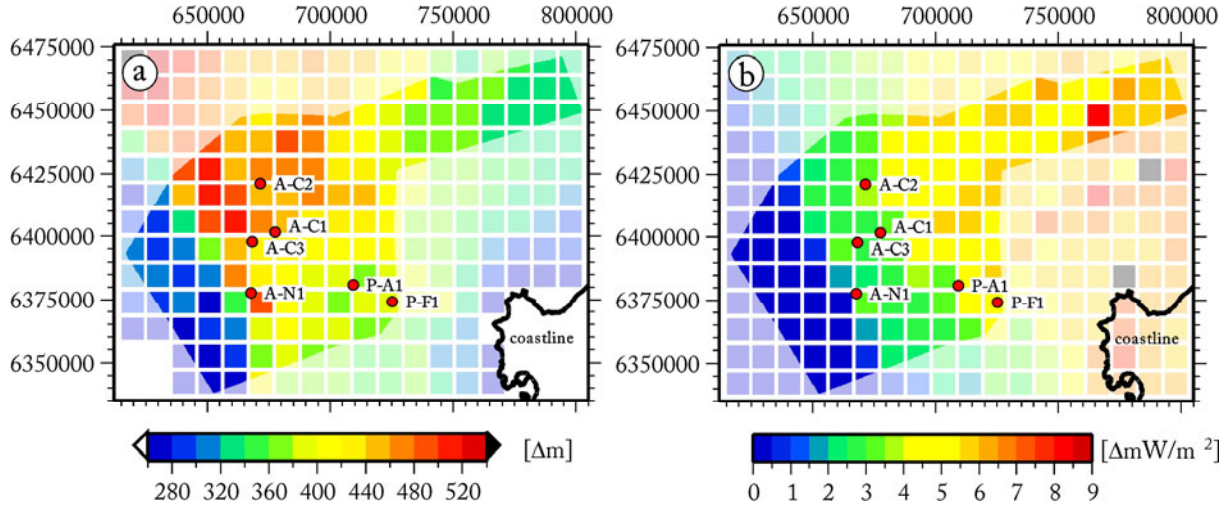

Figure 45: a) Map view of the calculated tectonically induced uplift for the time interval from 16 to 14 Ma indicating that maximum uplift occurred in the NW of the model. **b**) Map view of the increase in basement heat flow from 14 to 16 Ma.

Implications for hydrocarbon generation

The most interesting stages of basin development for hydrocarbon generation are those when the potential source rock intervals experienced maximum temperatures. The maximum temperatures can have been reached in response to maximum burial, due to a thermal overprint, or due to a superposition of both processes. The reconstructed subsidence of the basin documents a phase when the burial depth of the horizons exceeded the depth in which the horizons are found today (c.f. Figure 33a). This maximum burial depth was achieved before the 2nd uplift event 16 Ma ago. Accordingly, this time step is linked to peak temperatures to which the sediments have been subjected to.

The temperatures of the source rock intervals have been reported according to each time step before (cf. Figure 40, Figure 43). The entire temperature evolution is shown for one representative synthetic well in the vicinity of well A-C1 (Figure 46).

Phases of steep gradients in subsidence are also characterised by a steep increase in temperature, such as for the time interval between 117.5 and 103 Ma.

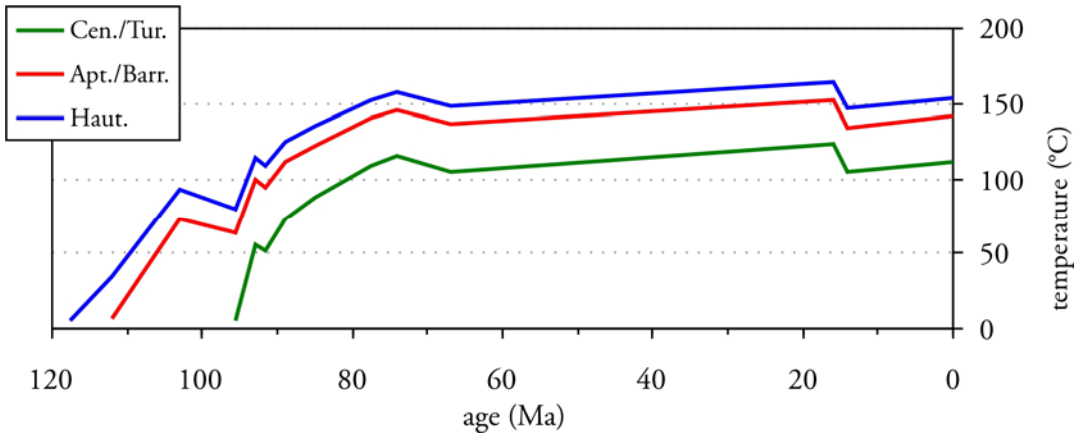

Figure 46: Temperature evolution through time for 3 depth intervals comprising potential source rock intervals documented for one synthetic well nearby well A-C1.

An erosional hiatus between 93 and 93.5 Ma is expressed as a minor temperature decrease. Subsequently, steadily proceeding subsidence acts in concert with increasing temperatures which reach a preliminary maximum at 74 Ma, before a temperature decrease documents the uplift the margin is subjected to. The maximum temperatures of 165°C are reached when the sediments experienced maximum burial at 14 Ma. The Hauterivian and the Aptian/Barremian source rock interval enter the maturity window of oil and gas generation when overstepping 0.5 in vitrinite reflectance at 95.5 and 93 Ma, respectively (Figure 47).

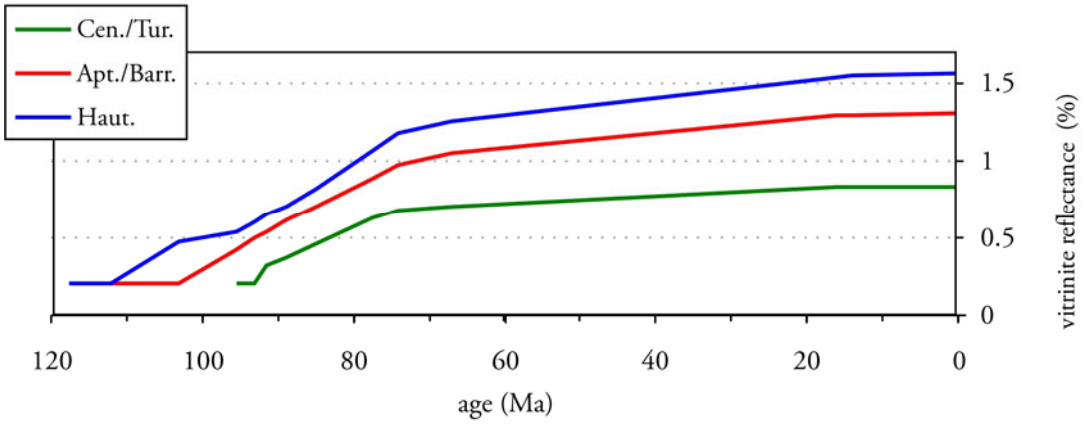

Figure 47: Maturity evolution through time for 3 depth intervals comprising potential source rock intervals documented for one synthetic well nearby well A-C1.

The cracking of oil to gas commences at a vitrinite reflectance value of 0.8 which starts for the deepest source rock at 85 Ma and for the Aptian/Barremian one aroung 77.5 Ma. Both exceed 1.0 in vitrinite reflectance at 77.5 and 67 Ma. The latter boundary is not exceeded by the youngest and most speculative source rock interval of Cenomanian/Turonian age, which remained in the oil and gas generation window from 85 Ma until 16 Ma. In contrast to the temperature evolution, short phases of tectonic activity are not expressed in the maturity evolution.

In response to the repeated shifts of depocentres the appraisal of present-day prospectivity should consider the spatial variation of the maturity related to the different source rocks at the time of deepest burial (16 Ma). At this time the Hauterivian source rock is predicted to have a maturity of more than 1.2 all across the outer margin and even more than 2.2 in the domains of largest sediment accumulation (Figure 48a). The same area is also more mature than 1.5 in the overlying Aptian/Barremian source rock interval, which reaches values of about ~1.0 on the outer margin (Figure 48b). The Cenomanian/Turonian source rock reaches ~0.6 on the middle margin which increases farther seaward to ~0.7 and to more than 1.0 in the domain of largest sediment thicknesses (Figure 48c).

4.5 Discussion and Conclusions

Our attempt to reconstruct the subsidence history in the Orange Basin revealed that a simple uniform stretching model is insufficient to explain the observed subsidence history in that it does neither predict the observed slope of initial tectonic subsidence nor Cenozoic phases of uplift. Only depth-dependent lithospheric thinning with larger thinning factors for the sub-crustal mantle can account for the subsidence history and the thermal evolution consistent with seismic data and measured vitrinite reflectance.

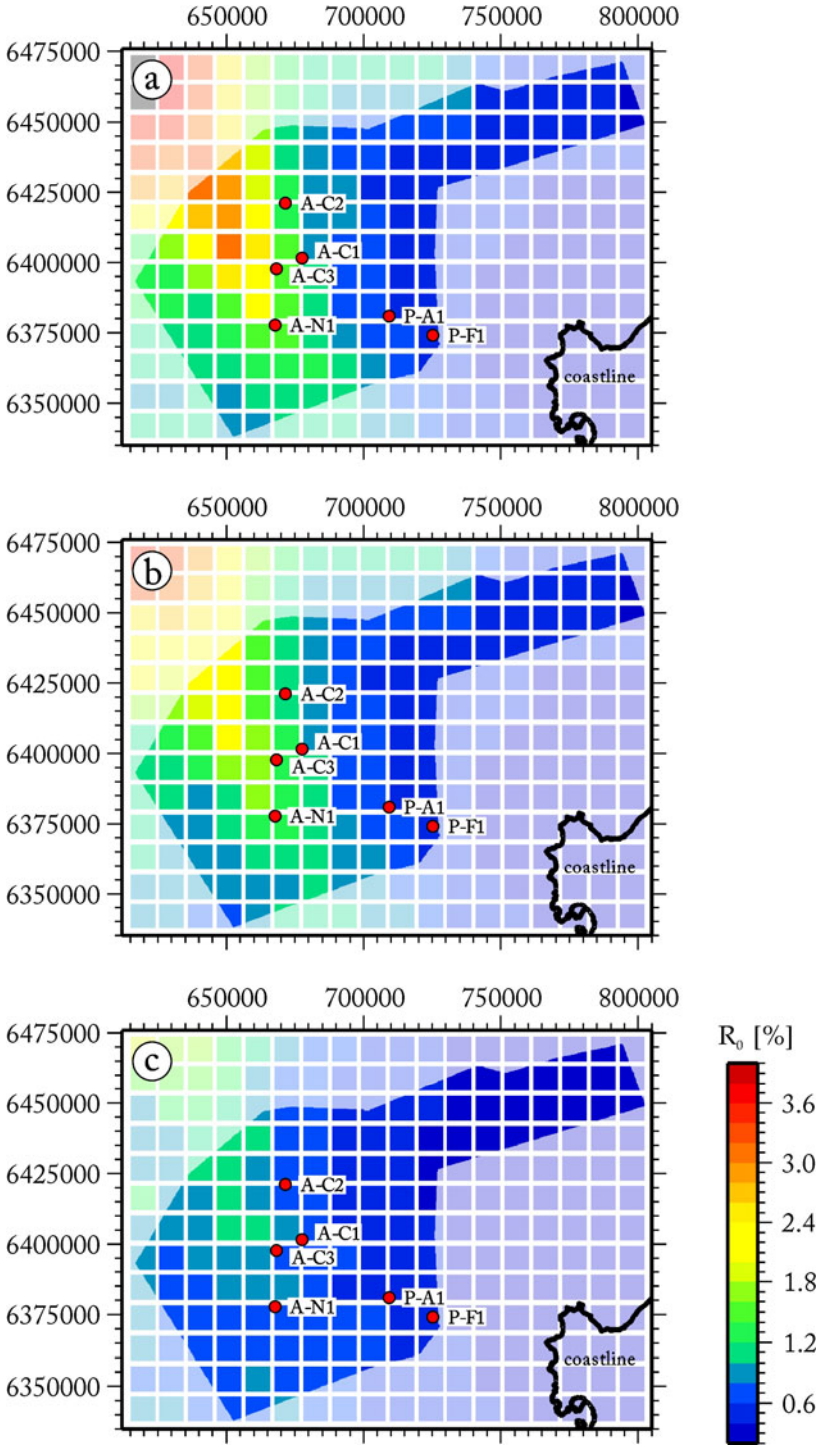

Figure 48: Map view of the spatial distribution of the modelled sediment maturity at 16 Ma when the sediments were subjected to maximum burial and maximum temperatures. **a)** Map view of the maturity of the Hauterivian source rock interval at 16 Ma. **b)** Map view of the maturity of the Aptian/Barremian source rock interval at 16 Ma. **c)** Map view of the maturity of the Cenomanian/Turonian source rock interval at 16 Ma.

The forward models which reproduce the observed subsidence history best include two departures from the uniform stretching model: First, underplating has been implemented considering the geometry of a high velocity, high density lower crustal body according to the study of Hirsch et al. (2007). The presence of these lower crustal bodies is a common feature along many volcanic passive continental margins (Watts and Fairhead, 1999) and for the study area, not only suggested by gravity modelling (Hirsch et al., 2007), but also proven by seismic refraction data (Hirsch et al., in press). In spite of a still ongoing discussion, these lower crustal bodies are interpreted as a result of magmatic underplating. Accordingly, this underplated material represents both ponded magmatic material trapped beneath the Moho and magmatic sills injected into the lower crust (White and McKenzie, 1989; Cox, 1992; Rutter et al., 1993; Thybo et al., 2000).

Observations supporting underplating occurring coevally with initial rifting include surface uplift, massive sand influx and the low subsidence rate during and after the break-up (Maclennan and Lovell, 2002). The production of the required melts is still a matter of debate and may be a result of elevated potential temperature of the mantle, of high extension rates, of small scale convection, or of fertile patches in the upper mantle (McKenzie and Bickle, 1988; Wilson, 1993; Boutillier and Keen, 1999; Korenaga, 2004; Buck, 1991; Pedersen and van der Beek, 1994; Van Wijk et al., 2001; Nielsen and Hopper, 2002; Foulger and Anderson, 2005). It is beyond the scope of this study to discriminate between causative mechanisms. Instead we aimed to assess the consequences of underplating for the subsidence and heat flow history. Our results confirm earlier studies (Fjeldskaar et al., 2003; Gernigon et al., 2004) in that the main effects of underplating in comparison to the uniform stretching model are the reduction of the initial subsidence, the significant but short termed increase in heat flow, and the enhanced post-rift subsidence due to the addition of further, hot material.

A second departure from the uniform stretching model is needed, since from initial rifting with coeval underplating alone, a much deeper basin is predicted than observed today and phases of intervening uplift in the Cenozoic would remain unexplained. This second departure consists of renewed sub-crustal thinning at times for which erosion is observed. A reactivated rifting of the sub-crustal domain interrupts the thermal subsidence in consequence of the initial rifting and induces uplift which is consistent with erosional unconformities documented in the seismic data and in the wells. In addition, sub-crustal stretching creates elevated heat flow scenarios. These scenarios seem to be appropriate since the thermal maturity of sediments within the Orange Basin is not only higher than would correspond to their present burial depth but also higher than a uniform stretching model would predict. In parts (A-C wells), even more erosion than suggested by seismic interpretation and, linked to that, mantle thinning is required to reproduce the observed maturity of the sediments.

These Cenozoic phases of uplift are more difficult to explain dynamically. Again, the phenomenon of post-break-up phases of uplift is observed at many passive margins but proposed mechanisms are the topic of controversy (Jackson et al., 2005). Post-break-up margin uplift may be a consequence of a rising mantle superswell (Burke, 1996; Nyblade and Robinson, 1994; Gurnis et al., 2000), of residual effects of long-lived Mesozoic plume heads and tails (Nyblade and Sleep, 2003), of lithospheric folding and thermal softening in response to ridge-push forces (Ayele, 2002), of small-scale convection (Huismans and Beaumont, 2008), or even of a renewed pulse of lithospheric extension in response to a change in plate rotation poles (Nürnberg and Müller, 1991; Guiraud and Bosworth, 1997). For passive margins west and south of South Africa a temporal correlation is reported

between phases of margin uplift, phases of increased denudation of the continent onshore (Kounov et al., 2007) and phases of Kimberlite emplacement (de Wit, 2007, Tinker et al., 2008), that points to processes affecting the lithospheric and sub-lithospheric mantle.

Rift shoulder uplift might provide a mechanism to explain the observed onshore topography including the Great Escarpment even though its origin and age is subjected to a controversy. Linked to that, flexural uplift due to isostatic rebound in response to erosion of the rift shoulders, can extend far into the basin and can cause uplift of the shelf (Burov and Cloetingh, 1997; Van Balen et al., 1995) but would not explain the phases of renewed subsidence subsequent to uplift.

The presence of the Great Escarpment might argue for a hybrid rifting model of simple shear in the upper crust on listrict or planar faults whereas the pure shear occurs in the ductile lower crust and mantle lithosphere (Kusznir, 1991). Seismic data do not indicate the presence of listric or planar faults cutting through the crust or upper mantle which discards this theory for explanation.

Another outcome of this study is the present-day heat flow in the basin. The values, as shown for well A-C1, are slightly higher than predicted for an old oceanic domain but in good agreement with heat flow values predicted by Goutorbe et al. (2008). Consistent with their results we found the contribution of the sediments to the surface heat flow to be less than ~5 mW/m². Since the contribution of the underplated body to the heat flow is negligible, the main component of the 50-60 mW/m² must be contributed by the mantle. Following their argumentation, there is a stark contrast between the estimated heat flow values of 17-30 mW/m² for the onshore Archean craton and the Proterozoic belts. The modelling results show an increase in surface heat flow across the margin with the highest values distal to the coast. Thus, the radiogenic heat production of the crust is inapplicable to explain the increase since the crust thins towards the ocean (Goutorbe et al., 2008). Global heat flow maps inferred from global seismic models show that continental margins are characterised by higher heat flow values as the adjacent oceanic and continental domains (Shapiro and Ritzwoller, 2004). This modelling is consistent with findings presented by Lucazeau et al. (2004) who found a similar heat flow distribution across the margin offshore Angola with the highest values on the continental shelf. They argue for an edge effect caused by an abrupt change in lithospheric thickness inducing convective patterns at the base of the lithosphere. Such an increase in heat flow over a relatively short distance could be reproduced in laboratory experiments (Guillou and Jaupart, 1995).

The lack of extensive volcanism within South Africa (Burke, 1996) today seems to rule out a thermal anomaly directly within or beneath the lithosphere. Several studies suggested that discontinuities in lithospheric thickness may result in small scale convective instabilities which might cause surface topography anomalies and/or tectonic features. Small scale convection models have been proposed with a downwelling that remains fixed at the margin of the craton whilst the upwelling moves off the spreading axes of the ocean basin (King and Ritsema, 2000). The downwelling would cause a cold thermal anomaly and could therefore account for lithospheric thinning in the absence of a positive anomaly.

The absence of volcanism in combination with the observed seismic structure of the lithosphere does not support models which suggest the emplacement of a Cenozoic mantle plume even if such a plume could account for the present-day elevation of south Africa. Even two starting mantle plume heads, one at the time of Karoo volcanism (ca. 183 Ma) and the other at the time of kimberlite eruption (ca. 80–90 Ma) cannot produce much (< 200 m) of

the present-day anomalous elevation (Nyblade and Sleep, 2003). Only if the plume tails linger beneath the lithosphere for ~25–30 Ma, ~500 m of present-day elevation could be reproduced but this theory also fails to explain the phases of uplift and subsidence by turns.

It has been found that the velocity of the deep mantle underneath South Africa is lower than average which is typical for hot regions (Gurnis et al., 2000). The interpretation of this anomaly is that it represents a long lived hot mantle upwelling which correlates spatially with long-wavelength geoid highs (Gurnis et al., 2000). Africa has the highest elevation of a continent probably indicative of uplift supported by very deep seated flow in the lower mantle.

A state of horizontal compression is proposed for the Lower Congo Basin from the analysis of fault mechanisms for 5 earthquakes controlled by distant plate-boundary forces (Ayele, 2002). Compression would thus support the existence of lithospheric folding (e.g. Cloetingh and Burov, 1996; Cloetingh et al., 1999) as a candidate to explain the observed uplift. This compression could be induced by ridge push of the Mid-Atlantic Ridge on the western plate boundary acting in concert with extension in the East African Rift System at the eastern plate boundary. On the other hand, the spreading rates between South America and Africa have been continuously decreasing since the onset of drifting (Müller et al., 1997). Therefore, it is questionable whether distant plate-boundary forces are causative mechanisms for the uplift observed in the South Atlantic. Furthermore, no compressional features are observed in our study area which is used as an argument to reject lithospheric buckling as causative mechanism.

Our results confirm the necessity to involve sub-crustal thinning in order to explain the observed post-break-up subsidence and the maturation of organic matter. If this mantle stretching is a consequence of any of the mantle processes presently discussed can not be deduced from our analysis but would require additional deep seismic and seismologic investigations.

In summary, our model predicts a syn-break-up setting characterised by shallow water depth and high heat flow due to differential stretching and associated underplating, subjected to subsequent thermal cooling and affected by two additional phases of sub-crustal stretching about 70 Ma after break-up. This concept is not only supported by the preserved sediment record and the evolution of tectonic subsidence but also by the crustal configuration observed today (Bauer et al., 2000; Hirsch et al. 2007, in press). Finally, the modelled thermal history suggests that the potential source rocks may have generated petroleum in the past and, provided adequate reservoir rocks and an intact seal exist, prospective petroleum systems may be present in the area.

Acknowledgements

This work has been done in the framework of INKABA yeAFRICA at the Helmholtz – Zentrum Potsdam Deutsches GeoForschungsZentrum-GFZ.

Isostatic modelling was performed with the Geological Modelling System (GMS) developed at GeoForschungsZentrum Potsdam, Department Organic Geochemistry under the leadership of Prof. Dr. U. Bayer.

Many thanks go to Bruno Goutorbe for providing temperature data. Heinz-Gerd Holl is thanked for discussing the porosity logs and Ian McMillan for help with the paleo water depths.

Maps were plotted using GMT 4.0 (http://gmt.soest.hawaii.edu/).

5 Conclusions

The overall objective of this thesis was to assess the structure of the crust underlying the Orange Basin and to evaluate the main controlling factors for its evolution.

The main focus of the first part of this work was to investigate the crustal structure with the help of a combined approach of isostatic calculations and gravity modelling.

Here, we obtained a model of the deeper crustal structure from shallow seismic information used in combination with the available free-air-gravity anomaly. Seismic data which resolve the sedimentary successions are used to set up a 3D structural model of the uppermost part of the lithosphere. Obeying the principles of Airy, several models were developed for the mid and lower crustal domains assuming an isostatic balanced system to evaluate the depth position of the Moho. Sensitivity tests were applied to these models and their 3D gravity response was validated against different crustal structures of the basin. A major result of this exercise was that it is only possible to reproduce the observed edge-effect anomaly when the mid to lower crust, departing from Airy´s approach, is heterogeneous, comprising a body in the lower crust of high density (3.2 g/cm³) and significant thickness (up to 14 km). This feature is interpreted as a relict of magmatic underplating representing the intrusive counterpart of the seaward dipping reflectors extruded coevally to rifting. The presence of underplated material and of seaward dipping reflectors confirms the magmatic character of the margin.

The second part of the thesis comprised investigations along a seismic refraction line crossing the Orange Basin farther north of the main working area, close to the border to Namibia. Here the picture is different; since seismic refraction data are available it is possible to image the structure of the entire crust. The processing of this refraction line confirmed the presence of a high velocity body in the lower crust close to the continent-ocean boundary in the northward projected continuation of the high density body found in the 3D gravity model. Furthermore, the refraction profile offered information on the seismic velocity structure in particular of this lower crustal body and the entire margin. The velocity model showed that the lower crustal body is not only characterised by high densities but also by high velocities (>7 km/s). The investigation has been extended in thus that gravity modelling and isostatic calculations helped to further reduce the ambiguousness in seismic velocity modelling. Seismic velocities have been converted into densities for gravity modelling to evaluate the density structure of the margin. Here, we found the high-density body in the lower crust to have a thickness of ~10 km and a density of 3.1 g/cm³. Thus, along the Springbok profile, the body is slightly less dense and less in volume than farther south. Finally, an isostatic crustal model integrating the changes applied to the gravity model indicates the isostatic equilibrium of the margin at least along the profile.

The 3D gravity model presented in the 1st part of this thesis suggests an underplated body of considerably greater thickness than found along the Springbok profile.

In contrast, additional seismic lines, the MAMBA lines, further north of Springbok document a decrease in thickness from north to south (Bauer et al., 2000).

These counterintuitive results pose the question which processes dictate the emplacement of underplating.

It has been argued in the second part of this thesis that an involved mantle plume might be responsible for the vast amounts of underplating but also decompressional melting processes alone might cause voluminous amount of melts to produce the observed underplated body.

Numerical simulations show that mantle temperatures, extension velocity, and pre-rift Moho configuration might determine to a large extent the amount of melt produced even without the presence of a warm mantle plume (Van Wijk et al., 2001). On the contrary, the decreasing magnesium content of the crust argues for a plume influence as far south as offshore Namibia but diminishing farther south (Trumbull et al., 2000, 2007). This image is supported by the seismic refraction lines.

The presence of seaward dipping reflectors along the entire South Atlantic margin otherwise seems to give evidence for decompressional melting processes. Furthermore, the found structure of the underplated body in the 3D model, thicker than found along the Springbok profile, argues due to its distal position to the plume trail for decompressional melting processes. Variable thicknesses might therefore be related to varying rifting parameters along the margin. On the other hand, one must keep in mind that modelling of potential field data is always prone to ambiguities. Therefore, only another seismic transect which crosses the working area can elucidate the deeper crustal structure and might help to confine the origin of the underplated body in the Orange Basin.

So far, models have been developed which characterise the present-day structure of the margin. But, as initially stated, a further point of interest was to reveal the past of the basin, which might also provide insights into the development of the hydrocarbon system of the region.

The previously developed models represent static models and dealt, amongst others, with the geometry of the underplated body and the present distribution of physical properties across the margin. The found geometry of the sediments, the crust and the high density body is used as an input for the last part of this thesis which attempts to derive a rifting model for the Orange Basin. This rifting model does not only reproduce the observed subsidence history but also considers the effects of magmatic underplating on the subsidence and on the thermal history of the basin. Even though it is not considered how the melt is generated and how it migrates, the model provides insights into the processes related to lithospheric extension and into the heat flow evolution through time. In turn, it is possible to deduce the temperature history for individual successions and make predictions for the maturity of the successions which comprise potential source rocks.

The results show that magmatic underplating indicated by the presence of the high density body in the lower crust is a pre-requisite to reproduce the observed subsidence patterns. The impact of the related elevated heat flow coeval to continental break-up is evaluated as well as the effect on the post-rift subsidence which becomes more effective due to the additional hot material. Considering the underplating represents a departure from the uniform stretching model. Further departures are renewed phases of sub-crustal stretching taking place in the Cenozoic. Sub-crustal stretching was found to be necessary since it represents a mechanism to explain the observed phases of erosion and uplift and, at the same time, the measured vitrinite reflectance data in the Orange Basin which are higher than expected from their present-day burial depth.

An important outcome of this study is that both the tectonic subsidence and the thermal history of the Orange Basin call for multiphase, depth-dependent differential stretching of the lithosphere. In detail, three main tectonic phases are found to describe the evolution of the Orange Basin in accordance with the present configuration of the margin and thermal history indicators. Initial rifting between 136 and 117.5 Ma, superimposed by magmatic underplating, results in a moderate intensity of initial tectonic subsidence followed by thermal cooling. This is interrupted by a 2nd tectonic phase involving sub-crustal stretching

around 74 – 67 Ma. The resulting uplift is expressed as an erosional unconformity over most of the margin. This 2nd phase of tectonic activity was again followed by thermal cooling and subsidence which in turn was interrupted by a 3rd event of sub-crustal stretching between 16 and 14 Ma.

The subsidence model that fits best with present-day structures and maturity data predicts an emplacement of the underplate coeval to initial rifting and continental break-up. The model further predicts that post-break-up phases of extension did not affect the crystalline crust but only the lithospheric mantle. This indicates that the crust was either mechanically too strong after the initial phase of rifting and 43 Ma of thermal equilibration to be stretched or that another process than extension was responsible for the thinning of the lithospheric mantle. Convective processes taking place in the asthenospheric upper mantle could have been responsible for this thinning of the lithospheric mantle and may have caused thermal erosion at the base of the lithosphere. The last conclusion, however, remains speculative. Likewise, we cannot discriminate between decrompressional melting and the influence of a mantle plume as causative mechanisms.

The situation in South Africa is unique in thus, the continent experienced repeated regional phases of uplift (de Wit, 2007). There is little consensus and an ongoing debate on the precise timing, duration and the amount of exhumation (e.g. Tinker et al., 2008; Paton et al., 2007; McMillan, 2003; Gallagher and Brown, 1999).

Repeated tilting of the margin during the Late Cenomanian until the Late Maastrichtian is inferred from the interpretation of foraminifera data in the basins on the South African continental margin (McMillan, 2003). A comprehensive analysis and comparison of sedimentary successions within 7 basins around South Africa provided evidence that these successions accumulated as a response to the local tectonic regime (McMillan, 2003). The global sea level change record remains completely concealed behind tectonically driven movements which excludes global sea level changes as a cause for major erosional events. Evidence for additional phases of uplift in the Neogene is provided by Partridge and Maud (1987) who related dated offshore marine sequences to terrestrial landsurfaces.

In contrast to the results presented in this thesis, modelling of apatite fission track data suggests that two thermal cooling events and by inference uplift and vast denudation onshore occurred prior to the Cenozoic (Tinker et al. 2008; Kounov et al., 2007). It has been questioned that the proposed upwelling of anomalously hot lower mantle material as a mechanism for these uplift events might have sustained the elevated topography of southern Africa or would have a rather transient uplift effect (de Wit, 2007; Nyblade and Sleep, 2003).

It is beyond the scope of this thesis to contribute to this ongoing controversy, as a lack of information on the amount and timing of Lower Cretaceous erosional events prevents to resolve possible phases of marginal uplift in the Cretaceous. However, in order to reproduce the present-day structures of the margin and to explain the observed tectonic subsidence history with its thermal implications a renewed sub-crustal stretching is required not earlier as the Cenozoic.

Summarising, we investigated the South African continental margin using diverse data sets and combined our findings to comprehensive models which give insights in the crustal structure based on seismic and gravity modelling. This gives a picture of the margin as we observe it today. Insights into the past are provided by inverse and forward modelling of real and synthetic wells which illustrate the evolution of the margin and comprise explanations on possible mechanisms for the present-day elevated position of the margin and the thermal overprint it must have experienced.

6 References

Airy, G.B., 1855. On the Computation of the Effect of the Attraction of Mountain-Masses, as Disturbing the Apparent Astronomical Latitude of Stations in Geodetic Surveys. Philosophical Transactions of the Royal Society of London, 145: 101-104.

Allen, P.A. and Allen, J.R., 2006. Basin Analysis: principles and applications. Blackwell Science Ltd., 549 pp.

Austin, J.A., Jr. and Uchupi, E., 1982. Continental-oceanic crustal transition off Southwest Africa. American Association of Petroleum Geologists Bulletin, 66(9): 1328-1347.

Ayele, A., 2002. Active compressional tectonics in central Africa and implications for plate tectonic models; evidence from fault mechanism studies of the 1998 earthquakes in the Congo Basin. Journal of African Earth Sciences, 35(1): 45-50.

Bauer, K. et al., 2000. Deep structure of the Namibia continental margin as derived from integrated geophysical studies. Journal of Geophysical Research, 105(B11): 25,829-25,853.

Bott, M.H.P., 1992. Passive margins and their subsidence. Journal of the Geological Society, 149(5): 805-812.

Boutilier, R.R. and Keen, C.E., 1999. Small-scale convection and divergent plate boundaries. Journal of Geophysical Research, 104(B4): 7389-7403.

Brown, L.F., Jr., Benson, J.M., Brink, G.J., Doherty, S., Jollands, A., Jungslager, E.H.A., Keenan, J.H.G., Muntingh, A., and van Wyk, N.J.S., 1995. Sequence stratigraphy in offshore South African divergent basins: an atlas on exploration for Cretaceous lowstand traps by SOEKOR (Pty) Ltd. American Association of Petroleum Geologists, Studies in Geology, 41, 184 pp.

Buck, R. and Anonymous, 1986. Possible relations between small-scale convection, linear gravity anomalies and ridge crest topographic variations. Eos, Transactions, American Geophysical Union, 67(16): 357.

Buck, W.R., 1991. Modes of continental lithospheric extension. Journal of Geophysical Research, 96(B12): 20,161-20,178.

Burke, K., 1996. The African Plate. South African Journal of Geology, 99(4): 339-409.

Burnham, A.K. and Sweeney, J.J., 1989. A chemical kinetic model of vitrinite maturation and reflectance. Geochimica et Cosmochimica Acta, 53(10): 2649-2657.

Burov, E. and Cloetingh, S., 1997. Erosion and rift dynamics; new thermomechanical aspects of post-rift evolution of extensional basins. Earth and Planetary Science Letters, 150(1-2): 7-26.

Christensen, N.I. and Mooney, W.D., 1995. Seismic velocity structure and composition of the continental crust: a global view. Journal of Geophysical Research, 100(B6): 9761-9788.

Cloetingh, S., Burov, E. and Poliakov, A., 1999. Lithosphere folding; primary response to compression? (from Central Asia to Paris Basin). Tectonics, 18(6): 1064-1083.

Cloetingh, S. and Burov, E.B., 1996. Thermomechanical structure of European continental lithosphere; constraints from rheological profiles and EET estimates. Geophysical Journal International, 124(3): 695-723.

Corcoran, D.V. and Clayton, G., 2001. Interpretation of vitrinite reflectance profiles in sedimentary basins, onshore and offshore Ireland. In: P.M. Shannon, P.D.W. Haughton and D.V. Corcoran (Editors), The petroleum exploration of Ireland's offshore basins. Geological Society Special Publications, pp. 61-90.

Cox, K.G., 1992. Karoo igneous activity, and the early stages of the break-up of Gondwanaland. Geological Society Special Publications, 68: 137-148.

de Wit, M.J., 2007. The Kalahari Epeirogeny and climate change; differentiating cause and effect from core to space. South African Journal of Geology, 110(2-3): 367-392.

Dingle, R.V., Siesser, W.G. and Newton, A.R., 1983. Mesozoic and Tertiary geology of Southern Africa. Rotterdam : A.A. Balkema ; Salem, N.H., U.S.A. : Distributed in the U.S.A. & Canada by M.B.S., 1983., 375 pp.

Doucouré, C.M. and de Wit, M.J., 2003. Old inherited origin for the present near-bimodal topography of Africa. Journal of African Earth Sciences, 36(4): 371-388.

Dow, W.G., 1977. Kerogen studies and geological interpretations. Journal of Geochemical Exploration, 7: 79-99.

Eagles, G., 2007. New angles on South Atlantic opening. Geophysical Journal International, 168(1): 353-361.

Eglington, B.M. and Armstrong, R.A., 2003. Geochronological and isotopic constraints on the Mesoproterozoic Namaqua-Natal Belt; evidence from deep borehole intersections in South Africa. Precambrian Research, 125(3-4): 179-189.

Eldholm, O., Gladczenko, T.P., Skogseid, J. and Planke, S., 2000. Atlantic volcanic margins: a comparative study, Dynamics of the Norwegian margin. Geological Society of London, Special Publications, London, United Kingdom, pp. 411-428.

Eldholm, O., Skogseid, J., Planke, S. and Gladczenko, T.P., 1995. Volcanic margin concepts. In: E. Banda, Talwani, M. & Torné, M. (Editor), Rifted Ocean–Continent Boundaries. Kluwer Academic Publishers, pp. 1-16.

Faulkner, P.A., 2000. Tectonic and thermal evolution of South Atlantic marginal basins, University of Cambridge.

Fjeldskaar, W., Johansen, H., Dodd, T.A. and Thompson, M., 2003. Temperature and maturity effects of magmatic underplating in the Gjallar Ridge, Norwegian Sea, Multidimensional basin modeling. American Association of Petroleum Geologists, Tulsa, OK, United States, pp. 71-85.

Foucher, J.-P., Le Pichon, X. , Sibuet, J.-C., Roberts, D. G., Chenet, P.-Y., Bally, A. W., Oxburgh, E. R., Kent, P., Dewey, J. F.,Bott, M. H. P., Jackson, J. A., Osmaston, M. F. and Turcotte, D.L., 1982. The ocean-continent transition in the uniform lithospheric stretching model: Role of partial melting in the mantle. Philosophical Transactions of the Royal Society of London. Series A, Mathematical and Physical Sciences, The Evolution of Sedimentary Basins, 305(1489): 27-43.

Foulger, G.R. and Anderson, D.L., 2005. A cool model for the Iceland hotspot. Journal of Volcanology and Geothermal Research, 141(1-2): 1-22.

Fowler, C.M.R., 1996. The Solid Earth: an introduction to global geophysics. Cambridge University Press, Cambridge, 704 pp.

Frimmel, H.E. and Frank, W., 1998. Neoproterozoic tectono-thermal evolution of the Gariep Belt and its basement, Namibia and South Africa. Precambrian Research, 90(1-2): 1-28.

Gernigon, L. et al., 2006. A moderate melting model for the Voring margin (Norway) based on structural observations and a thermo-kinematical modelling: Implication for the meaning of the lower crustal bodies. Tectonophysics, 412(3-4): 255-278.

Gernigon, L., Ringenbach, J.-C., Planke, S. and Le Gall, B., 2004. Deep structures and breakup along volcanic rifted margins: insights from integrated studies along the outer Voring Basin (Norway). Marine and Petroleum Geology, 21(3): 363-372.

Gernigon, L., Ringenbach, J.C., Planke, S., Le, G.B. and Jonquet, K.H., 2003. Extension, crustal structure and magmatism at the outer Voring Basin, Norwegian margin. Journal of the Geological Society of London, 160(2): 197-208.

Gerrard, I. and Smith, G.C., 1982. Post-Paleozoic succession and structure of the southwestern African continental margin. In: J.S. Watkins, Drake, C.L. (Editors), Studies in Continental Margin Geology. American Association of Petroleum Geologists Memoir, Tulsa, pp. 49-74.

Gladczenko, T.P. et al., 1997. South Atlantic volcanic margins. Journal of the Geological Society, 154(3): 465-470.

Gladczenko, T.P., Skogseid, J. and Eldholm, O., 1998. Namibia volcanic margin. Marine Geophysical Researches, 20(4): 313-341.

Goetze, H.-J. and Lahmeyer, B., 1988. Application of three-dimensional interactive modeling in gravity and magnetics. Geophysics, 53(8): 1096-1108.

Goutorbe, B., Lucazeau, F. and Bonneville, A., 2008. The thermal regime of South African continental margins. Earth and Planetary Science Letters, 267(1-2): 256-265.

Green, R.W.E. and Durrheim, R.J., 1990. A seismic refraction investigation of the Namaqualand Metamorphic Complex, South Africa. Journal of Geophysical Research, 95(B12): 19,927-19,932.

Grunow, A., Hanson, R., and Wilson, T., 1996. Were aspects of Pan-African deformation linked to Iapetus opening? Geology, 24(12): 1063-1066.

Guillou, L. and Jaupart, C., 1995. On the effect of continents on mantle convection. Journal of Geophysical Research, 100(B12): 24,217-24,238.

Guiraud, R. and Bosworth, W., 1997. Senonian basin inversion and rejuvenation of rifting in Africa and Arabia; synthesis and implications to plate-scale tectonics. Tectonophysics, 282(1-4): 39-82.

Gurnis, M., Mitrovica, J.X., Ritsema, J. and van Heijst, H.-J., 2000. Constraining mantle density structure using geological evidence of surface uplift rates: The case of the African Superplume. Geochemistry, Geophysics, Geosystems - G (super 3), 1(7): Paper Number 1999GC000035.

Herbin, J.P. et al., 1987. Cretaceous anoxic events in the South Atlantic. Revista Brasileira de Geociencias, 17(2): 92-99.

Héroux, Y.A., Chagnon, A. and Bertrand, R., 1979. Compilation and correlation of major thermal maturation indicators. American Association of Petroleum Geologists Bulletin, 63: 2128-2144.

Hinz, K., 1981. Hypothesis on terrestrial catastrophes: wedges of very thick oceanward dipping layers beneath passive continental margins - their origins and paleoenvironmental significance. Geologisches Jahrbuch, Series E, 22: 1-28.

Hirsch, K.K., Bauer, K. and Scheck-Wenderoth, M., 2008. Deep structure of the western South African passive margin - Results from a combined approach of seismic, gravity and isostatic investigations. Tectonophysics.

Hirsch, K.K., Scheck-Wenderoth, M., Paton, D.A. and Bauer, K., 2007. Crustal structure beneath the Orange Basin, South Africa. South African Journal of Geology, 110(2/3): 249-260.

Holbrook, W.S. and Kelemen, P.B., 1993. Large igneous province on the US Atlantic margin and implications for magmatism during continental breakup. Nature (London), 364(6436): 433-436.

Holbrook, W.S. et al., 1994. Deep structure of the U.S. Atlantic continental margin, offshore South Carolina, from coincident ocean bottom and multichannel seismic data. Journal of Geophysical Research, B, Solid Earth and Planets, 99(5): 9155-9178.

Huismans, R.S. and Beaumont, C., 2008. Complex rifted continental margins explained by dynamical models of depth-dependent lithospheric extension. Geology (Boulder), 36(2): 163-166.

Jackson, M.P.A., Hudec, M.R. and Hegarty, K.A., 2005. The great West African Tertiary coastal uplift; fact or fiction? A perspective from the Angolan divergent margin. Tectonics, 24(6): 23.

King, S.D. and Ritsema, J., 2000. African hot spot volcanism; small-scale convection in the upper mantle beneath cratons. Science, 290(5494): 1137-1140.

Korenaga, J., 2004. Mantle mixing and continental breakup magmatism. Earth and Planetary Science Letters, 218(3-4): 463-473.

Kounov, A. et al., 2007. Present denudation rates at selected sections of the South African escarpment and the elevated continental interior based on cosmogenic (super 3) He and (super 21) Ne. South African Journal of Geology, 110(2-3): 235-248.

Kuhlmann, G., R. di Primio, D. van der Spuy and Horsfield, B., 2008. Implications of Slope Failures for the Hydrocarbon System in the Orange Basin, Offshore South Africa, American Association of Petroleum Geologists, Annual Convention and Exhibition, San Antonio, Texas.

Kusznir, N.J., Hunsdale, R., Roberts, A.M. and iSIMMTeam, 2005. Timing and magnitude of depth-dependent lithosphere stretching on the southern Lofoten and northern Vøring continental margins offshore mid-Norway: implications for subsidence and hydrocarbon maturation at volcanic rifted margins. In: A.G.V. Doré, B. A. (Editor), Petroleum Geology: North-West Europe and Global Perspectives—Proceedings of the 6th Petroleum Geology Conference. Petroleum Geology Conferences Ltd. Published by the Geological Society, London, pp. 767-783.

Kusznir, N.J., Marsden, G. and Egan, S.S., 1991. A flexural-cantilever simple-shear/pure-shear model of continental lithosphere extension; applications to the Jeanne d'Arc Basin, Grand Banks and Viking Graben, North Sea. Geological Society Special Publications, 56: 41-60.

Kusznir, N.J., Roberts, A.M. and Morley, C.K., 1995. Forward and reverse modelling of rift basin formation. In: J.J. Lambiase (Editor), Hydrocarbon Habitat in Rift Basins. Geological Society, London, pp. 33-56.

Light, M.P.R., Maslanyj, M.P. and Banks, N.L., 1992. New geophysical evidence for extensional tectonics on the divergent margin offshore Namibia. In: B.C. Storey, T. Alabaster and R.J. Pankhurst (Editors), Magmatism and the causes of continental break-up. Special Publications. Geological Society, London, United Kingdom, pp. 257-270.

Lucazeau, F., Brigaud, F. and Bouroullec, J.L., 2004. High-resolution heat flow density in the Lower Congo Basin. Geochemistry, Geophysics, Geosystems - G (super 3), 5: doi:10.1029/2003GC000644.

Ludwig, W.J., Nafe, J.E. and Drake, C.L., 1970. Seismic refraction. In: A.E. Maxwell (Editor), The Sea. Wiley-Interscience, New York, pp. 53-84.

Macdonald, D., Gomez-Perez, I., Franzese, J., Spalletti, L., Lawver, L., Gahagan, L., Dalziel, I., Thomas, C., Trewin, N., Hole, M., and Paton, D., 2003. Mesozoic break-up of SW

Gondwana; implications for regional hydrocarbon potential of the southern South Atlantic. Marine and Petroleum Geology, 20(3-4): 287-308.
Maclennan, J. and Lovell, B., 2002. Control of regional sea level by surface uplift and subsidence caused by magmatic underplating of Earth's crust. Geology (Boulder), 30(8): 675-678.
Mahanyele, P.J. et al., 2004. How far to the south does the volcanic margin of Southwest Africa extend? An initial velocity model for the ocean-continent transition in the southern Cape Basin, 64. Jahrestagung der Deutschen Geophysikalischen Gesellschaft. Abstract volume, Berlin, pp. 443-444.
Marsh, J.S., Ewart, A., Milner, S.C., Duncan, A.R. and Miller, R.M., 2001. The Etendeka igneous province; magma types and their stratigraphic distribution with implications for the evolution of the Parana-Etendeka flood basalt province. Bulletin of Volcanology, 62(6-7): 464-486.
McKenzie, D., 1978. Some remarks on the development of sedimentary basins. Earth and Planetary Science Letters, 40(1): 25-32.
McKenzie, D. and Bickle, M.J., 1988. The volume and composition of melt generated by extension of the lithosphere. Journal of Petrology, 29(3): 625-679.
McMillan, I.K., 2003. Foraminiferally defined biostratigraphic episodes and sedimentation pattern of the Cretaceous drift succession (Early Barremian to Late Maastrichtian) in seven basins on the South African and southern Namibian continental margin. South African Journal of Science, 99(11-12): 537-576.
Milner, S.C., LeReox, A.P. and O'Connor, M., 1995. Age of Mesozoic igneous rocks in northwestern Namibia, and their relationship to continental breakup. Journal of the Geological Society London, 152(1): 97-104.
Mjelde, R. et al., 2002. Lower crustal seismic velocity-anomalies; magmatic underplating or serpentinized peridotite? Evidence from the Vøring Margin, NE Atlantic. Marine Geophysical Researches, 23(2): 169-183.
Müller, R.D., Roest, W.R., Royer, J.-Y., Gahagan, L.M. and Sclater, J.G., 1997. Digital isochrons of the world's ocean floor. Journal of Geophysical Research, 102(B2): 3211-3214.
Muntingh, A., 1993. Geology, prospects in Orange Basin offshore western South Africa. Oil and Gas Journal, 91(4): 106-109.
Muntingh, A. and Brown, L.F.J., 1993. Sequence stratigraphy of the petroleum plays, postrift Cretaceous rocks (lower Aptian to upper Maastrichtian), Orange Basin, western offshore, South Africa. In: P. Weimer, Posamentier, H.W. (Editors), Siliclastic Sequence Stratigraphy - recent developments and applications. American Association of Petroleum Geologists Memoir, Tulsa, pp. 71-97.
Nielsen, T.K. and Hopper, J.R., 2002. Formation of volcanic rifted margins; are temperature anomalies required? Geophysical Research Letters, 29(21): 4.
Nürnberg, D. and Müller, R.D., 1991. The tectonic evolution of the South Atlantic from Late Jurassic to present. Tectonophysics, 191(1-2): 27-53.
Nyblade, A.A. and Robinson, S.W., 1994. The African superswell. Geophysical Research Letters, 21(9): 765-768.
Nyblade, A.A. and Sleep, N.H., 2003. Long lasting epeirogenic uplift from mantle plumes and the origin of the southern African Plateau. Geochemistry, Geophysics, Geosystems, 4(12): 1105.

Partridge, T.C. and Maud, R.R., 1987. Geomorphic evolution of Southern Africa since the Mesozoic. South African Journal of Geology, 90(2): 179-208.

Paton, D.A., van der Spuy, D., di Primio, R. and Horsfield, B., 2008. Tectonically induced adjustment of passive-margin accommodation space; influence on the hydrocarbon potential of the Orange Basin, South Africa. American Association of Petroleum Geologists Bulletin, 92(5): 589-609.

Pedersen, T. and van der Beek, P., 1994. Extension and magmatism in the Oslo Rift, Southeast Norway; no sign of a mantle plume. Earth and Planetary Science Letters, 123(1-4): 317-329.

Pluijm, B.A.v.d. and Marshak, S., 2004. Earth Structure. W. W. Norton Company, New York, London, 656 pp.

Porada, H., 1979. The Damara-Ribeira orogen of the Pan-African-Brasiliano cycle in Namibia (Southwest Africa) and Brazil as interpreted in terms of continental collision. Tectonophysics, 57: 237-265.

Pratt, J.H., 1855. On the Attraction of the Himalaya Mountains, and of the Elevated Regions beyond Them, upon the Plumb-Line in India. Philosophical Transactions of the Royal Society of London, 145: 53-100.

Raum, T. et al., 2006. Crustal structure and evolution of the southern Vøring Basin and Vøring Transform Margin, NE Atlantic. Tectonophysics, 415(1-4): 167-202.

Reeves, C. and de Wit, M., 2000. Making ends meet in Gondwana: retracing the transforms of the Indian Ocean and reconnecting continental shear zones. Terra Nova, 12(6): 272-280.

Reid, D.L., Erlank, A.J. and Rex, D.C., 1991. Age and correlation of the False Bay dolerite dyke swarm, south-western Cape, Cape Province. South African Journal of Geology, 94(2-3): 155-158.

Reid, D.L. and Rex, D.C., 1994. Cretaceous dykes associated with the opening of the South Atlantic; the Mehlberg Dyke, northern Richtersveld. South African Journal of Geology, 97(2): 135-145.

Roberts, A.M., Kusznir, N.J., Yielding, G. and Styles, P., 1998. 2D flexural backstripping of extensional basins; the need for a sideways glance. Petroleum Geoscience, 4(4): 327-338.

Royden, L. and Keen, C.E., 1980. Rifting process and thermal evolution of the continental margin of eastern Canada determined from subsidence curves. Earth and Planetary Science Letters, 51(2): 343-361.

Rutter, E.H., Brodie, K.H. and Evans, P.J., 1993. Structural geometry, lower crustal magmatic underplating and lithospheric stretching in the Ivrea-Verbano zone, northern Italy. Journal of Structural Geology, 15(3-5): 647-662.

Sandwell, D.T. and Smith, W.H.F., 1997. Marine gravity anomaly from Geosat and ERS 1 satellite altimetry. Journal of Geophysical Research, B, Solid Earth and Planets, 102(5): 10,039-10,054.

Scheck, M. and Bayer, U., 1997. Configuration of the crust below the intracratonic Northeast German Basin. Terra Nostra, 97/11: 121-125.

Scheck, M. and Bayer, U., 1999. Evolution of the Northeast German Basin -- inferences from a 3D structural model and subsidence analysis. Tectonophysics, 313(1-2): 145-169.

Schinkel, J., December 2006. Tiefenstruktur der Kontinent-Ozean-Grenze vor dem Orange Fluss, Namibia. Diploma Thesis, Institut für Geowissenschaften der Friedrich-Schiller-Universität, Jena.

Schnabel, M. et al., 2006. Deep Structure of the Argentine and Conjugated South African Continental Margins, American Association of Petroleum Geologists, International Conference and Exhibition, Perth, Australia.

Sclater, J.G. and Christie, P.A.F., 1980. Continental stretching: An explanation of the Post-Mid-Cretaceous subsidence of the central North Sea Basin. Journal of Geophysical Research, 85(B7): 3711-3739.

Seider, G. and Mitchell, J.G., 1976. Episodic mesozoic volcanism in Namibia and Brazil:A Kr-Ar isochron study bearing on the opening of the South Atlantic. Earth and Planetary Science Letters, 30: 292-303.

Shapiro, N.M. and Ritzwoller, M.H., 2004. Inferring surface heat flux distributions guided by a global seismic model: particular application to Antarctica. Earth and Planetary Science Letters, 223(1-2): 213-224.

Sleep, N.H. and Fuyita, K., 1997. Principles of Geophysics. Blackwell Science, Malden, 586 pp.

Spudich, P. and Orcutt, J., 1980. A New Look at the Seismic Velocity Structure of the Oceanic Crust. Reviews of Geophysics and Space Physics, 18(3): 627-645.

Stein, C.A. and Stein, S., 1992. A model for the global variation in oceanic depth and heat flow with lithospheric age. Nature (London), 359(6391): 123-129.

Stewart, J., Watts, A.B. and Bagguley, J.G., 2000. Three-dimensional subsidence analysis and gravity modelling of the continental margin offshore Namibia. Geophysical Journal International, 141(3): 724-746.

Talwani, M. and Abreu, V., 2000. Inferences regarding initiation of oceanic crust formation from the U.S. East Coast Margin and conjugate South Atlantic margins. In: W. Mohriac, Talwani, M. (Editor), Atlantic rifts and continental margins. American Geophysical Union, Washington, DC, United States, pp. 211-233.

Thybo, H., Maguire, P.K.H., Birt, C. and Perchuc, E., 2000. Seismic reflectivity and magmatic underplating beneath the Kenya Rift. Geophysical Research Letters, 27(17): 2745-2748.

Tinker, J., de Wit, M. and Brown, R., 2008. Mesozoic exhumation of the southern Cape, South Africa, quantified using apatite fission track thermochronology. Tectonophysics, 455(1-4): 77-93.

Trumbull, R.B. et al., 2000. Insights on the genesis of the Cretaceous Damaraland igneous complexes in Namibia from a Nd- and Sr-isotopic perspective. Communications of the Geological Survey of Namibia, 12: 313-324.

Trumbull, R.B., Reid, D.L., de Beer, C., vanAcken, D. and Romer, R.L., 2007. Magmatism and Continental Breakup at the West Margin of Southern Africa: A Geochemical Comparison of Dolerite Dikes from NW Namibia and the Western Cape. South African Journal of Geology, 110(2/3): 477-502.

Trumbull, R.B., Sobolev, S.V. and Bauer, K., 2002. Petrophysical modeling of high seismic velocity crust at the Namibian volcanic margin. Special Paper - Geological Society of America, 362: 221-230.

Turcotte, D.L. and Schubert, G., 2002. Geodynamics. New York, NY (US) ;John Wiley and Sons, Inc., United States, 472 pp.

van Balen, R.T., van der Beek, P.A. and Cloetingh, S.A.P.L., 1995. The effect of rift shoulder erosion on stratal patterns at passive margins; implications for sequence stratigraphy. Earth and Planetary Science Letters, 134(3-4): 527-544.

van der Spuy, D., Jikelo, N.A., Ziegler, T. and Bowyer, M., 2003. Deepwater 2D data reveal Orange basin objectives off western South Africa. Oil & Gas Journal, 101: 44-49.

van Wees, J.D. and Beekman, F., 2000. Lithosphere rheology during intraplate basin extension and inversion; inferences from automated modeling of four basins in Western Europe. Tectonophysics, 320(3-4): 219-242.

van Wees, J.D. and Stephenson, R.A., 1995. Quantitative modelling of basin and rheological evolution of the Iberian Basin (Central Spain): implications for lithospheric dynamics of intraplate extension and inversion. Tectonophysics, 252(1-4): 163-178.

Van Wees, J.D. et al., in press. Probabilistic tectonic heat flow modelling for basin maturation: assessment method and applications. Marine and Petroleum Geology.

Van Wijk, J.W., Huismans, R.S., ter Voorde, M. and Cloetingh, S.A.P.L., 2001. Melt generation at volcanic continental margins; no need for a mantle plume? Geophysical Research Letters, 28(20): 3995-3998.

Walcott, R.I., 1972. Gravity, Flexure, and the Growth of Sedimentary basins at a Continental Edge. Geological Society of America Bulletin, 83(6): 1845-1848.

Watts, A.B., 1988. Gravity anomalies, crustal structure and flexure of the lithosphere at the Baltimore Canyon Trough (Atlantic). Earth and Planetary Science Letters, 89(2): 221-238.

Watts, A.B. and Fairhead, J.D., 1999. A process-oriented approach to modeling the gravity signature of continental margins. The Leading Edge, 18: 258-263.

Wernicke, B., 1981. Low-angle normal faults in the Basin and Range Province; nappe tectonics in an extending orogen. Nature (London), 291(5817): 645-648.

White, R. and McKenzie, D., 1989. Magmatism at rift zones - The generation of volcanic continental margins and flood basalts. Journal of Geophysical Research, 94(6): 7685-7729.

White, R.S., Spence, G.D., Fowler, S.R., McKenzie, D.P., Westbrook, G.K., Bowen, A.N., 1987. Magmatism at rifted continental margins. nature, 330: 439-444.

Wilson, M., 1993. Magmatism and the geodynamics of basin formation. Sedimentary Geology, 86(1-2): 5-29.

Zelt, C.A. and Smith, R.B., 1992. Seismic traveltime inversion for 2-D crustal velocity structure. Geophysical Journal International, 108: 16-34.

7 Acknowledgements

I would like to express gratitude to my supervisors Onno Oncken and Sierd Cloetingh to furnish the reviews for this thesis.

I´m very grateful for the support I experienced from Leni. She helped steady the ship on several occasions not only with scientific advice but helped as a friend. I´d like to thank for many insightful discussions and new provided directions. She was sustaining my work even when I got bogged down with details.

Thanks go to Brian Horsfield who supported my work as the head of Section 4.3 and as the head of the project INKABA yeAFRICA in which this work was imbedded. Maarten de Wit provided support as a reviewer and insistent disputer who tried to get to the bottom of everything and see beyond the obvious.

This work benefited from the fundament provided by Douglas A. Paton who furthermore participated as a short term supervisor and finally found his role as the perfect proofreader. Gesa Kuhlmann was my co-worker in the Orange Basin and I want to thank for fruitful discussions.

Klaus Bauer is thanked for the extensive collaboration and perfect teamwork on the Springbok refraction line and on many additional occasions.

I want to thank Bob Trumbull for the permission to pop up in his office at any time and find him ready for enthusiastic discussions. He always encouraged me to alternative views and taught me to be "cool like a cucumber".

Special thanks go to Jan-Diederick van Wees, who guided me through the minefield called "Petroprob", and the Amsterdam group, especially Fred and Maarten, who helped in various ways.

H.-J. Goetze is thanked for courtesy of IGMAS and especially Zuzana Alasonati Tašárová who very patiently introduced me to the world of IGMAS.

My fellow roommates went with me through all the ups and downs of doing a PhD and we had a really good time together. Even when Mauro was "too busy" he was always ready to help and Judith represents my favourite and best source of geological information and grammar answers.

Thanks go to my colleagues of Section 4.4. and the entire floor C4, thank you for the good working atmosphere. Lew helped greatly with solving several computer problems.

All colleagues from GFZ Section 4.3 are thanked for helpful discussions on geochemical "stuff" I had no clue about and helped in dealing with Petrel or Petromod. Thank you Robert, Volkmar, Raingard, Zahie, Rolando (hereby you finally receive the beta factors you yearned for so long). I also benefited from the advice given by Yurij, thanks for that.

Without the loving support from my family and my friends I would never have lasted the distance: Thanks for everything.

And finally, I´d love to thank my greatest fan and critic Uli for everything, every day.

8 Appendix

Model setup and development

The models described in detail in chapter 4.4.2 represent only a small fraction of the total number of models studied. They represent the basic outcome of this work and the final models are based on a suite of sensitivity studies. In order to provide the input parameters for a geohistory analysis and to put a model together for the individual wells, many input parameters need to be examined and predefined.
A geohistory analysis results in diagrams of time versus depth, depicting the subsidence history of a well by plotting the numeric ages of the unit boundaries (from biostratigraphy) against their depths. Therefore, the composition of the sediments and their thermal characteristics needs to be examined for each well. Furthermore, the response of the porosity of the sediments to loading and unloading and linked to that the density variations with depth of the sediments have to be specified beforehand.
For each well the lithological composition was used as input for the backstripping procedure. It was achieved from studying well reports to determine the individual fractions of clay, silt, sandstone, and other components. Accordingly, for each fraction the depth-dependent porosity decrease was established in a double-porosity-depth curve (Table 2). This curve describes the porosity decrease with increasing burial. Available well logs documenting the density and the porosity were corrected and used to constrain the porosity-depth curve in thus that the found sediment composition and the according porosity-depth curves reproduce the measured porosity and density values. This procedure was applied to each well. Both parameters directly affect the modelling results; the porosity predominantly influences the thermal calculations (e.g. the predicted maturity of the sediments), whereas the density affects the calculated isostatic response of the system.
Furthermore, the thermal parameters of sediments such as thermal conductivities and heat production and their influence on the modelling results of the predicted vitrinite reflectance data were in addition investigated. Starting with literature values, which provide for most rocks a range of appropriate values, adequate values were found which fitted to geothermal constraints provided in form of vitrinite reflectance data. This alignment was done for each sediment fraction and for each individual well.
The predefined depth-porosity-curves and the thermal parameters of the sediments have a significant influence on the modelled vitrinite reflectance values. As described in chapter 4.4.2 (heat flow) the values in the uppermost part of the wells are always underestimated by the models predictions. Changing the predefined depth-porosity-curves and the thermal parameters of the sediments alone does not improve the modelling results in the intended way. It is possible to increase or decrease the gradient of vitrinite reflectance increase with depth but it does not elevate the values in the uppermost part of the wells. Thus, the observed vertical shift can not be explained with changing thermal parameters alone.
After having obtained the input parameters for the sediments, it is crucial to have a good constraint on both the pre-rift crustal thickness and the lithospheric thickness in order to achieve forward models to explain the observations.

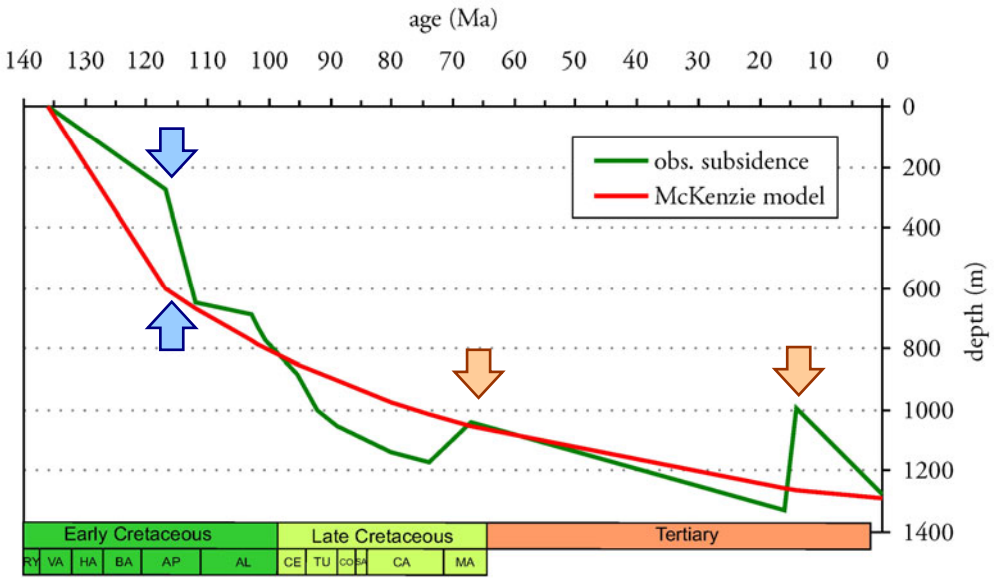

Figure A1: Subsidence history predicted by a McKenzie model (red curve) overlain by the observed subsidence (green curve). Striking mis-matches occur in the syn-rift phase (blue arrows) where the initial subsidence is overestimated and in the post-rift phase (brownish arrows) since the McKenzie fails to reproduce phases of margin uplift.

The crustal thickness found along the Springbok profile indicates a crust of 38 km onshore. In a first instance, varying crustal thicknesses have been tested based on an instantaneous stretching model after McKenzie. The crustal thickness and the lithospheric thickness have a decisive influence on the general shape and the final depth of the developing basin predicted by these models. The thicker the crust, the less pronounced subsidence occurs. A range of ± 20 km was used for a series of tested models. Finally, 36 km give the best fit and appear to be reasonable compared to the crustal thickness found along the Springbok profile onshore in the domain not affected by stretching.

A sensitivity analysis was also carried out to find a reasonable initial lithospheric thickness. Here, literature values provided the starting point (http://www.lithosphere.info/TC1-2006.html). The global thermal model TC1 for the continental lithosphere predicts a value between 100 and 125 km.

Basin history inversion models revealed that the required initial lithospheric thickness consistent with the subsidence history is 146 km. This value results from a series of calculated models with tested thicknesses varying between 100 km and 160 km pre-rift thickness for the lithospheric.

A McKenzie model is characterised by steep initial subsidence in the syn-rift phase followed by continuous, moderate subsidence in the post-rift phase driven by thermal cooling of the basin (Figure A1). In contrast, the observations indicate a less pronounced subsidence for the syn-rift phase of the Orange Basin as predicted in the McKenzie forward model (Figure A1) and, furthermore, we find phases of uplift in the post-rift phase of the Orange Basin which are not explained by thermal cooling alone.

But it was not only aimed to obtain a rough fit with McKenzie models, which lack to explain phases of margin evolution when overprinting mechanisms have been active. Therefore, several model configurations have been examined as described in the following. It was aimed to reproduce the observed geometry of the sediments in the course of the modelling and also the vitrinite reflectance data which represent geothermal constraints.

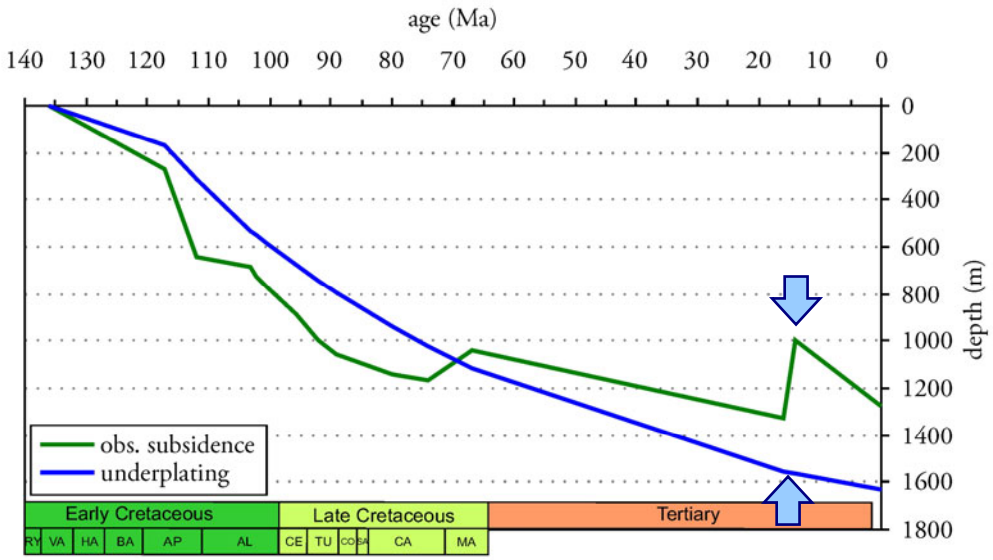

Figure A2: Subsidence history predicted by a model which incorporates underplating in the syn-rift phase (blue curve) overlain by the observed subsidence (green curve). The initial subsidence is reduced compared to a McKenzie model and is in good agreement with the observations. Mis-matches occur in the post-rift phase, since the model still fails to reproduce phases of margin uplift (blue arrows).

It is known from previous studies (e.g. Bauer et al., 2000; Hirsch et al., 2007) that rifting was accompanied by underplating. Therefore, underplating has been implemented in a further set of forward models as a first departure from the classical McKenzie model since the latter does not incorporate the generations of melts. The geotherm does not intersect the solidus of crustal and mantle material in a McKenzie model and the generation of melts is inhibited.
The presence of underplated material reduces the initial subsidence in comparison to the McKenzie model since this material replaces lithospheric material so that the net effect is uplift relative to the depth expected from McKenzie models. The thickness of the underplated material was taken from the results of the 3D gravity modelling (Chapter 2, this thesis). Here again, the post-rift subsidence is solely driven by thermal cooling which in this case is more pronounced due to the addition of further hot material to the system and the predicted final basin depth is much deeper than observed (Figure A2).
The according basement heat flow evolution for both forward models is shown in Figure A3. For the underplating model, the predicted heat flow peak reaches 95 mW/m² and is continuously decreasing in the post-rift phase. In contrast, the McKenzie model predicts a heat pulse during the process of rifting which slightly oversteps 55 mW/m². Here, the post-rift thermal cooling is less pronounced as if further hot material is emplaced.
Since this first departure from the McKenzie model is insufficient to explain the geometries of the sediments in the observed way, a further modification is needed. In the reconstructed subsidence history two phases of uplift were found. As a possible causative mechanism explaining these observations mantle thinning was evaluated.
Thus, in the course of modelling the next generation of models was evaluated which takes the emplacement of underplating in the rifting stage into consideration and which allows for mantle thinning since Campanian times. Figure A4 illustrates that a good fit is achieved for the predicted subsidence history and the observations, not only for the initial subsidence but also for the post-rift phases of uplift. Herein, the amount of uplift is depending on the amount of erosion reconstructed from seismic interpretation. This model fulfils the first modelling goal in thus it reconstructs the present day geometries of the sediments.

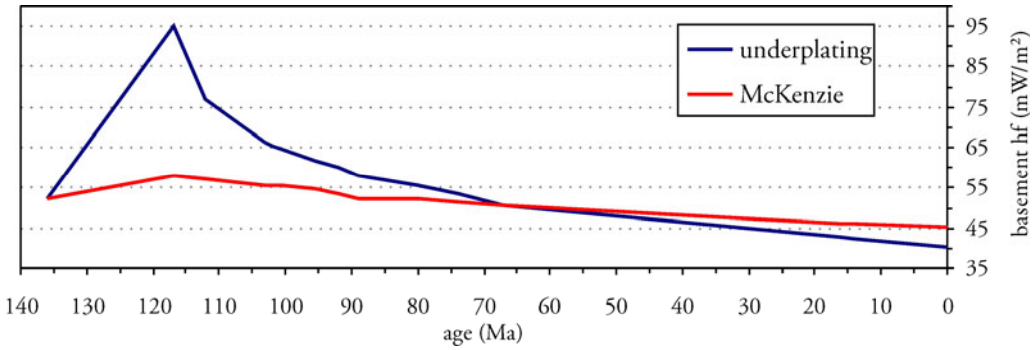

Figure A3: A diagram illustrating the basement heat flows for the McKenzie model (red curve) and the model which incorporates underplating in the syn-rift stage (blue curve).

The proposed final model, which includes both underplating and post-rift mantle thinning, indicates that the margin experienced more subsidence and burial than indicated by the present-day sediments geometry. The vitrinite reflectance data found in the Orange Basin show elevated values compared to a global compilation (Allen and Allen, 2006 and references therein). In other words, the values are higher than indicated by their present-day burial depth.

Therefore, we propose more burial and subsequent uplift of the margin to explain the elevated values. But also alternative processes have been tested. These alternatives include elevated heat flow values for different time intervals but no further burial. Three examples for the tested alternative models are shown in Figure A5. Even if the heat pulse is almost as high as during the process of rifting the impact on the calculated maturity values is small. However, heat peaks of various intensity and duration are insufficient to explain the elevated values of vitrinite reflectance data and support the proposed combination of more burial and subsequent margin uplift which is here explained by mantle thinning.

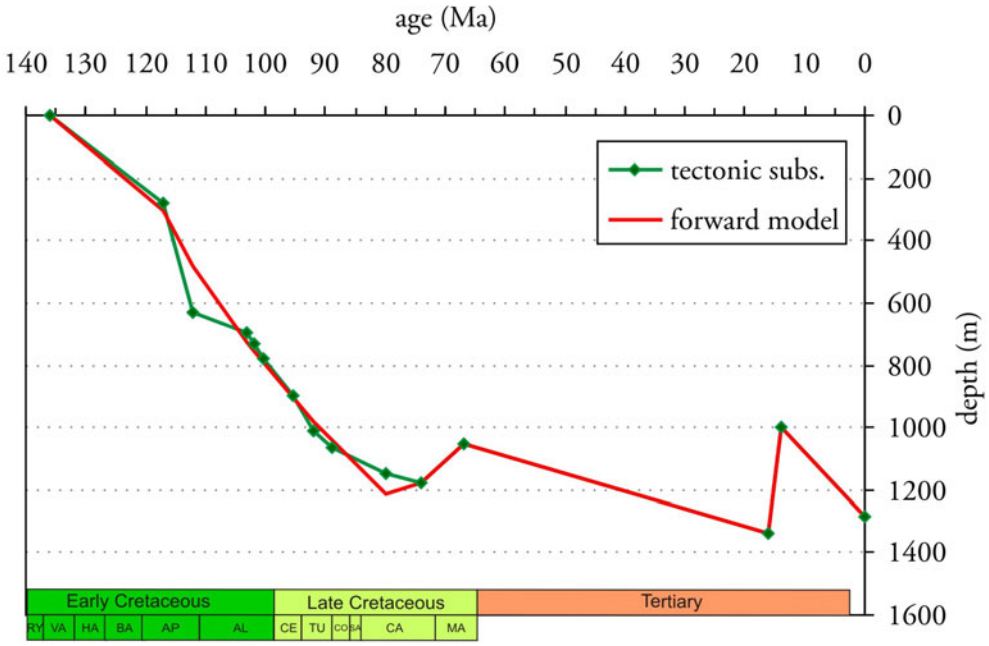

Figure A4: Subsidence history predicted by a model which incorporates underplating in the syn-rift phase (red curve) and mantle thinning in the post-rift phase overlain by the observed subsidence (green curve).

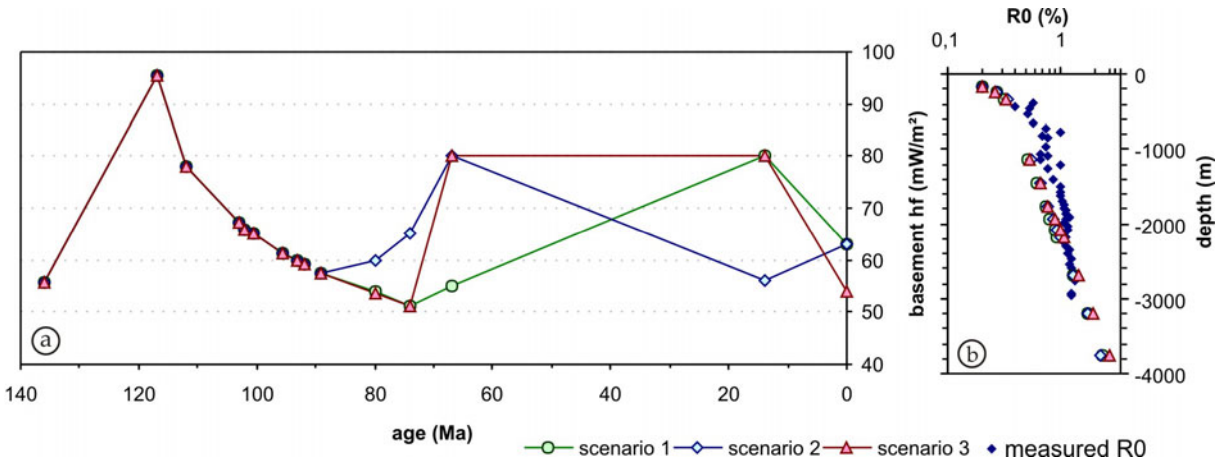

Figure A5: Alternative models developed to evaluate the influence of basement heat flow peaks in the absence of margin uplift. **a)** Basement heat flow scenarios used as input and **b)** the according predicted vitrinite reflectance values.

ISSN 1610-0956